



Attribution–NonCommercial–NoDerivs 2.0 KOREA

You are free to :

- **Share** — copy and redistribute the material in any medium or format

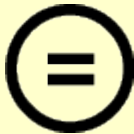
Under the following terms :



Attribution — You must give [appropriate credit](#), provide a link to the license, and [indicate if changes were made](#). You may do so in any reasonable manner, but not in any way that suggests the licensor endorses you or your use.




NonCommercial — You may not use the material for [commercial purposes](#).



NoDerivatives — If you [remix, transform, or build upon](#) the material, you may not distribute the modified material.

You do not have to comply with the license for elements of the material in the public domain or where your use is permitted by an applicable exception or limitation.

This is a human-readable summary of (and not a substitute for) the [license](#).

[Disclaimer](#) 

Doctoral Thesis

Gate-Tunable Magnetotransport in Ferromagnetic  
ZnO Nanowire FET Devices

Vijayakumar Modepalli

Department of Materials Science and Engineering

Graduate School of UNIST

2016

# Gate-Tunable Magnetotransport in Ferromagnetic ZnO Nanowire FET Devices

Vijayakumar Modepalli

Department of Materials Science and Engineering

Graduate School of UNIST

# Gate-Tunable Magnetotransport in Ferromagnetic ZnO Nanowire FET Devices

A thesis/dissertation  
submitted to the Graduate School of UNIST  
in partial fulfillment of the  
requirements for the degree of  
Doctor of Philosophy

Vijayakumar Modepalli

06. 14. 2016 of submission

Approved by

---

Advisor

Jung-Woo Yoo

# Gate-Tunable Magnetotransport in Ferromagnetic ZnO Nanowire FET Devices

Vijayakumar Modepalli

This certifies that the thesis/dissertation of Vijayakumar Modepalli is  
approved.

06. 14. 2016 Month/Day/Year of submission

signature

---

Advisor: Jung-Woo Yoo

signature

---

Kibog Park

signature

---

Jeong Min Baik

signature

---

Ki-Suk Lee

signature

---

Jeongyong Kim

## **ABSTRACT**

Electrical manipulation of magnetization has grown as an essential ingredient in rapidly evolving spintronic research. Switching of nano-scale magnetization can be induced by a spin-polarized current *via* spin-transfer torque, domain wall motion, and/or spin-orbit torque, which are being increasingly utilized for magnetic memory devices under development. Apart from current dissipation, the electric field itself can also be used to control the magnetism in various materials, especially in dilute magnetic semiconductors (DMSs). A gate-voltage-induced accumulation of charge could alter magnetic exchange interactions and eventually lead to changes in magnetic moment, coercivity, anisotropy, and transition temperature. Semiconductor spintronics has garnered increasing attention due to the concept behind the spin field-effect transistor (spin-FET), where the spin precession is governed by the gate-controllable Rashba field. Tuning the magnetization of the source and drain in the spin-FET architecture offers additional state variables in future state-of-the-art electronic applications.

This dissertation addresses the study of dramatic gate-induced change of ferromagnetism in ZnO nanowire (NW) field-effect transistors (FETs). The ZnO NWs used in this study were grown by using chemical vapor deposition (CVD) technique. The crystal structure and composition of ZnO NWs were studied by X-ray diffraction (XRD), high-resolution transmission electron microscopy (HRTEM), and X-ray photoelectron spectroscopy (XPS). Ferromagnetism in our ZnO NWs arose from oxygen vacancies, which constitute deep levels hosting unpaired electron spins. The magnetic transition temperature of the studied ZnO NWs was estimated to be well above room temperature. The *in situ* UV confocal photoluminescence (PL) study confirmed oxygen vacancy mediated ferromagnetism in the studied ZnO NW FET devices. Both the estimated carrier concentration and temperature dependent conductivity reveal the studied ZnO NWs are at the crossover of the metal-insulator transition. In particular, gate-induced modulation of the carrier concentration in the ZnO NW FET significantly alters carrier-mediated exchange interactions, which causes even inversion of magnetoresistance (MR) from negative to positive values. Upon sweeping the gate bias from  $-40$  V to  $+50$  V, the MRs estimated at 2 T and 2 K were changed from  $-11.3\%$  to  $+4.1\%$ . Detailed analysis on the gate dependent MR behavior clearly showed enhanced spin splitting energy with increasing carrier concentration. Gate voltage dependent PL spectra of an individual NW device confirmed the localization of oxygen vacancy-induced spins, indicating that gate-tunable indirect exchange coupling between localized magnetic moments played an important role in the remarkable change of the MR.



## Table of Contents

Abstract.....	i
List of figures.....	v
List of tables.....	xi
<b>1. Introduction.....</b>	<b>1</b>
1.1. Spintronics.....	1
1.2. Diluted magnetic semiconductors .....	2
1.3. Scope of thesis.....	5
<b>2. Spintronics: Magnetoresistance overview .....</b>	<b>7</b>
2.1. Introduction .....	7
2.2. Ordinary magnetoresistance .....	8
2.3. Anisotropic magnetoresistance .....	9
2.4. Giant magnetoresistance .....	10
2.5. Tunneling magnetoresistance .....	11
2.6. Magnetoresistance in a non-local spin valve .....	13
2.7. Magnetoresistance due to weak localization .....	16
2.8. Spin orbit interaction and Hall effects.....	18
2.8.1. Spin orbit interaction .....	18
2.8.2. Anomalous Hall effect .....	19
2.8.3. Spin Hall effect .....	20
2.9. Control of magnetism by electric fields .....	22
<b>3. Experimental Techniques.....</b>	<b>23</b>
3.1. Device fabrication procedure .....	23
3.2. Atomic layer deposition .....	26
3.3. Physical vapor deposition.....	31
3.4. Electrical measurement setup.....	35
3.5. Physical property measurement system.....	37
3.6. Magnetic property measurement system .....	39
<b>4. ZnO nanowires: Growth and characterization .....</b>	<b>41</b>
4.1. Introduction .....	41
4.2. Experiment: Synthesis of ZnO nanowires using CVD method.....	44



4.3. Characterization of ZnO nanowires.....	46
4.3.1. Results and Discussion: XRD and HR-TEM analysis .....	46
4.3.2. Results and Discussion: XPS analysis.....	48
4.4. Ferromagnetism in ZnO nanowires .....	50
4.4.1. Introduction .....	50
4.4.2. Results and Discussion.....	51
4.5. Conclusions .....	53
<b>5. ZnO nanowire field effect transistor .....</b>	<b>54</b>
5.1. Introduction .....	54
5.2. Experiment: Device fabrication.....	55
5.3. Results and Discussion.....	57
5.4. Conclusions .....	61
<b>6. Gate-tunable magnetotransport in single ferromagnetic ZnO nanowire(NW) FET devices 62</b>	<b>62</b>
6.1. Gate-tunable spin exchange interactions and magnetoresistance .....	62
6.1.1. Introduction .....	62
6.2. Results and analysis.....	63
Gate-tunable inversion of magnetoresistance in ferromagnetic ZnO NW .....	63
Temperature dependent magnetotransport of ferromagnetic ZnO NW .....	66
Discussion .....	70
Reproducibility of the results .....	81
6.3. Threshold voltage dependence of giant magnetoresistance in ferromagnetic ZnO NW FET devices.....	82
6.4. Conclusions .....	85
<b>7. Gate-tunable photoluminescence study of single ferromagnetic ZnO nanowire FET devices .....</b>	<b>86</b>
7.1. Experiment: UV- confocal microscopy.....	86
7.2. Results and Discussion.....	88
7.2.1. PL imaging of a single ZnO NW FET device .....	88
7.2.2. Gate voltage induced PL imaging of a single ZnO NW FET device .....	90
7.3. Conclusions .....	93
<b>References .....</b>	<b>94</b>
<b>Acknowledgements.....</b>	<b>105</b>

## LIST OF FIGURES

**Figure 2.1.** Schematic illustration of electron spin with the net magnetic moment  $\mu$  and charge  $e$ .

**Figure 2.2.** The typical anisotropic magnetoresistance in a ferromagnetic metals and alloys and its corresponding schematics to show the orientation of magnetization and current density.

**Figure 2.3.** Magnetoresistance (MR) of three Fe/Cr superlattices at 4.2 K. Here the current flow direction and the applied magnetic field are along the [110] axis in the plane of the layers [2].

**Figure 2.4.** Schematic illustration of a tunneling magnetoresistance (TMR) effect by means of spin dependent tunneling. In a magnetic tunnel junction, the density of states of both ferromagnetic layers determines whether a large current (a) or small current (b) tunnel through.

**Figure 2.5.** (a-b) Schematic layout of four terminal NSLV device with (a) parallel and (b) antiparallel magnetization of the spin injector and detector. (c-d) The spin splitting of the electrochemical potential  $\Delta\mu$  corresponding spin accumulation produced by spin injection from contact 2. Depending on the direction of magnetization, the  $V_{NL}$  measured at contact 3, either spin up (c) or spin down branch (d) of the chemical potential.

**Figure 2.6.** (a) Schematic layout of the four terminal NLSV. (b) Nonlocal magnetoresistance characteristic of the GaN nanowire at room temperature under in plane magnetic field. The arrows indicate the relative orientation of the injector (contact 2) and detector (contact 3) [27].

**Figure 2.7.** Transport in a diffusive regime: (a) Weak localization due to constructive interference. (b) Weak-anti localization due to incoherent scattering of electron waves.

**Figure 2.8.** Schematic illustration of the spin hall effect.

**Figure 2.9.** Schematic illustration of experimental setup to measure inverse SHE.

**Figure 2.10.** An electrically controlled magnetic switch designed by Ohno et al,[81] where the field effect control of the hole induced ferromagnetism in magnetic semiconductor (In,Mn)As field effect transistor. The cross section of the metal insulator semiconductor field effect transistor is shown in the above figure. The applied gate voltage ( $V_G$ ) controls the hole (filled circles) concentration in the semiconductor channel. Negative  $V_G$  increase the hole concentration, resulting in enhancement of ferromagnetic interaction among Mn ions, whereas the positive  $V_G$  has an opposite effect. The schematic

arrow in the above figure shows the magnitude of the Mn magnetization. The buffer layer corresponds to the InAs/(Al,Ga)Sb/AlSb structure.

**Figure 3.1.** Experimental procedure for ZnO NW device fabrication

**Figure 3.2.** The image of Reference number patterns, transformed onto SiO<sub>2</sub> substrate to identify the location of nanowire while performing e-beam lithography.

**Figure 3.3.** (a) Optical microscope image taken after the e-beam lithography processing and development. (b) Optical microscope image taken after the process of liftoff step. Figure (a and b) also shows that, during the spin coating process, sometimes the unwanted nanowire debris will migrate into the NW location and causes the electrode damage.

**Figure 3.4. The visualization of ALD process by depositing Al<sub>2</sub>O<sub>3</sub> using TMA and H<sub>2</sub>O precursors.**

(a) The surface of the substrate initially covered with hydroxyl groups. (b) Formation of new intermediate layer after reacting TMA molecules with hydroxyl groups. (c) The substrate covered with new intermediate layer. (d) Reaction between H<sub>2</sub>O molecules and intermediate layer, leading to the target Al<sub>2</sub>O<sub>3</sub> and new hydroxyl groups. (e) The substrate again covered by hydroxyl groups. [Reproduced from Meng, X.B. et al., 2012. [92]]

**Figure 3.5.** Experimental setup for ALD: Various components of SVTA ALD system. [Extracted From SVTA ALD Manual]

**Figure 3.6.** The picture of the RoboALD software main page. The RoboALD software is written in LabView language and ranges from complete manual operation of each component to full recipe automation.

**Figure 3.7.** Experimental setup for thermal evaporation technique. Thermal evaporation technique was used to deposit the gold (Au) electrode to the ZnO NW during device processing.

**Figure 3.8.** Schematic illustration of the electron beam evaporation technique

**Figure 3.9.** Experimental setup for electron beam evaporation technique. This technique was used to deposit various types of materials such as titanium (Ti), aluminum oxide (Al<sub>2</sub>O<sub>3</sub>), iron (Fe), and cobalt (Co) during device fabrication process.

**Figure 3.10. Electrical measurement setup.** (a) Physical property measurement system and electric measurement setup, where the measurement was taken by using Keithley electric instrument. (b) Standard

sample puck and (c) rotator puck (for angle dependent measurements) for various magnetic field ( $-9$  T to  $+9$  T) and temperature dependent measurements.

**Figure 3.11.** Installed LabVIEW software in a PPMS computer to control all electric measurements and PPMS options together with the help of Multivu software.

**Figure 3.12.** Major components of the PPMS probe [Extracted from Quantum design PPMS manual].

**Figure 3.13.** Scheme of the MPMS SQUID magnetometer (left), geometry of the detection coil and sample response curve (right) [From QD MPMS manual].

**Figure 4.1.** Schematic view of the hexagonal wurzite ZnO crystal structure [93]. The light grey spheres corresponds to oxygen, whereas dark spheres corresponds to zinc. The base plane primitive translation vectors  $a$  and  $b$  include an angle of  $120^\circ$  and  $c$  is orthogonal to them.

**Figure 4.2.** Schematic chart representing various methods employed in the growth of ZnO nanostructures

**Figure 4.3.** Schematic illustration of growth mechanism of ZnO nanowires using CVD method

**Figure 4.4.** Scanning electron microscopy (SEM) image of an assembly of ZnO NWs grown by CVD method.

**Figure 4.5. Structural characteristics of ZnO NWs grown by the CVD method.** (a) XRD pattern of as-grown ZnO NWs grown on a sapphire substrate by CVD method.

**Figure 4.6.** HR-TEM image of ZnO NW shows growth in the  $c$ -axis direction of the hexagonal wurtzite phase. Inset shows the corresponding SAED pattern.

**Figure 4.7. Elemental characteristics of ZnO NWs grown on the sapphire substrate.** (a) Survey XPS spectrum of ZnO NWs on the sapphire substrate. (b-c) Magnified views on the XPS spectrum corresponding to the Zn- $2p$  (b) and O- $1s$  (c) core level regions.

**Figure 4.8.** Dietl et al. predicted of critical temperatures for various Mn-doped  $p$ -type semiconductors (diluted magnetic semiconductors). [104]

**Figure 4.9.** Magnetization as a function of magnetic field measured at  $T = 300, 200, 100$  and  $10$  K for an assembly of ZnO NWs.

**Figure 4.10.** Normalized saturation magnetization as a function of  $(M_s/M_0)$  as a function of temperature. The estimated Curie temperature to be well above room temperature (approximately  $416$  K).

**Figure 5.1.** (a) Schematic illustration of a typical Al<sub>2</sub>O<sub>3</sub>-capped ZnO NW FET device and (b) its corresponding SEM image with multiple electrodes. Here, the effective channel length was  $L = 1.5 \mu\text{m}$ .

**Figure 5.2.**  $I$ - $V$  characteristics of the studied ZnO NW at  $T = 300 \text{ K}$ . The extracted resistivity was determined to be  $\rho \sim 0.023 \Omega \cdot \text{cm}$  at  $V_g = 0 \text{ V}$ .

**Figure 5.3.** The corresponding  $V_g$ - $I_d$  characteristics at  $V_{ds} = 100 \text{ mV}$ . The obtained field-effect mobility was  $\mu = 32.5 \text{ cm}^2/(\text{V} \cdot \text{s})$ , and the carrier density was  $n = 8.04 \times 10^{18} \text{ cm}^{-3}$ .

**Figure 5.4.** Temperature dependent transport of ZnO NW device at  $V_g = 0 \text{ V}$ .

**Figure 5.5. FET behavior and transport parameters at  $T = 2\text{K}$ .** (a)  $V_g$ - $I_d$  curve of ZnO NW FET device at  $V_{ds} = 100 \text{ mV}$ . At  $V_g = 0 \text{ V}$ , the carrier density was estimated to be  $n = 7.54 \times 10^{18} \text{ cm}^{-3}$  and the mobility to be  $= 21.49 \text{ cm}^2/\text{V} \cdot \text{s}$ . (b) The carrier density  $n$  (left axis) and the corresponding  $k_F l$  value (right axis) as a function of  $V_g$ .

**Figure 6.1.** Schematic view of the magnetotransport in ZnO NW FET device, where the magnetic field is applied perpendicular to the axial direction of the NW.

**Figure 6.2. Gate-dependent magnetotransport of a single ferromagnetic ZnO NW FET device.** Gate voltage induced inversion of magnetoresistance from negative to positive was observed under various gate voltages  $V_g$  between  $-40 \text{ V}$  and  $+50 \text{ V}$  at  $2\text{K}$ .

**Figure 6.3.** Gate-dependent MR value of a single ferromagnetic ZnO NW FET device at  $H = 0$  and  $1.5 \text{ T}$ ,  $T = 2\text{K}$ . Left axis shows the magnitude of MR as a function of gate voltage, where the MR value is dramatically tuned upon sweeping the gate voltage from  $-40 \text{ V}$  to  $+50 \text{ V}$  at  $2\text{K}$ . Right axis shows the field effect resistance as a function of gate voltage at  $H = 0$  value.

**Figure 6.4. Temperature dependent magnetotransport of a single ferromagnetic ZnO NW.** The observed negative MR for (a)  $V_g = -40 \text{ V}$  and (b)  $V_g = -30 \text{ V}$  under various temperatures. The temperature dependent behavior shows that, the magnitude of MR was dramatically decreased as the temperature was increased.

**Figure 6.5. Temperature dependent magnetotransport of a single ferromagnetic ZnO NW.** The observed negative MR for (a)  $V_g = +50 \text{ V}$  and (b)  $V_g = +40 \text{ V}$  under various temperatures. The temperature dependent behavior shows that, the magnitude of MR was dramatically decreased as the temperature was increased and at  $T = 30 \text{ K}$  the sign of MR was inverted from positive to negative before it reaches to the negligible value at  $50 \text{ K}$ .

**Figure 6.6.** Summary of temperature-dependent magneto-transport of a single ferromagnetic ZnO NW under various gate voltages at  $H = 1.5$  T. When the temperature was lowered to below 30 K, the MR bifurcated into positive and negative values according to the applied gate voltage, and its magnitude increased as the temperature was decreased further.

**Figure 6.7. Description of the fit of a semiempirical model to the measured MR values.** Eqn 6.1 curves fit to the measured MR values at  $T = 2$  K for various gate voltages in ZnO NW. All curves fit well to the collected data over all gate voltages.

**Figure 6.8.** The obtained fitting parameter  $b$  as a function of gate voltage  $V_g$  at  $T = 2$  K.

**Figure 6.9.** The obtained fitting parameters  $c$  and  $d$  of Eqn 6.1 obtained at  $V_g = +50$  V.

**Figure 6.10. Description of MR in ferromagnetic ZnO NW by fitting the measured values with a semi-empirical model of Eqn 6.1.** (a-b) Fitting the measured values with semi-empirical model, at a gate voltage of  $V_g = +50$  V and  $+40$  V under varied temperatures. The MR values were observed to decrease with increasing temperature, and became negative at around 30 K. The MR was negligible at 50 K. (c-d) Fitting measured MR values with a semi-empirical model, at a gate voltage of  $V_g = -30$  V and  $-40$  V under varied temperatures. In all above cases, the experimental values are in good agreement with the semi empirical model.

**Figure 6.11.** The obtained fitting parameter  $b$  as a function a function of temperature for gate voltages  $V_g = -40$  V and  $-30$  V.

**Figure 6.12.** The temperature dependent parameters  $c$  and  $d$  of Eqn 6.1 obtained at  $V_g = +50$  V.

**Figure 6.13: Reproducibility of the gate dependence of MR in our ferromagnetic ZnO NW FET (device B).** (a) Gate-tunable inversion of MR at  $T = 2$  K. (b) Gate-dependent MR value of at  $H = 0$  and 1 T,  $T = 2$  K. Left axis shows the magnitude of MR as a function of gate voltage, where the MR value is dramatically tuned upon sweeping the gate voltage from  $-40$  V to  $+50$  V at 2K. Right axis shows the field effect resistance as a function of gate voltage at  $H = 0$  value. (c-d) Temperature dependence of MR collected at  $V_g = +50$  V and  $+40$  V.

**Figure 6.14. Gate-dependent magnetotransport of a ferromagnetic ZnO NW.** (a) Gate voltage induced tuning of giant magnetoresistance for  $V_g = +40$  V and  $+35$  V at  $T = 2$  K. (b) The left axis shows the extracted value of maximum MR, and right axis shows the zero field resistance as a function of gate voltage.

**Figure 6.15.** (a)  $V_g$ - $I_d$  characteristics of a ZnO NW FET devices at  $T = 300$  K. The FET characteristics of the Devices # 1,2,3 was governed by the native doping concentration in ZnO NWs, where Device #1 lies at the insulator regime, devices # 2,3 lies at the crossover of metal-insulator transition regime. (b) The corresponding MR curves for Devices # 1 and 3 at  $V_g = +40$  V. The inset shows the extracted MR value as a function of device number (#) at  $V_g = +40$  V and  $H = 1$  T.

**Figure 7.1.** Schematic view of the UV confocal PL spectral imaging of a single ZnO NW device with the application of gate voltage. The laser power applied to the sample was typically  $50 \mu\text{W}$  and an acquisition time of 150 ms per pixel was used for PL spectral imaging.

**Figure 7.2. Optical properties of the studied ZnO NW.** (a) The RT-PL intensity mapping of single ZnO NW device with zero gate bias. Contrast scale of the PL image represents the photon counts, i.e., PL intensity. (b) RT-PL spectra of a single ZnO NW device

**Figure 7.3.** Schematic illustration of the energy band diagram of the ZnO NW including various defect-related energy levels.

**Figure 7.4. Gate-tuned RT PL emission intensity mapping of a single ZnO NW device.** (a-d) The emission intensity mapping of the UV band edge emission peak (main peak) and defect-related peaks at gate voltages  $V_g = 0$  and  $+30$  V. A wavelength range of 370-450 nm was chosen to display the main band edge emission (a and c), while 480-640 nm was the selected range to display oxygen vacancy-induced emission (b and d). Dotted line in PL images represent the location of the NW and the electrodes.

**Figure 7.5. Gate-tuned RT PL spectra of a single ZnO NW device.** The PL spectra of the single ZnO NW FET measured at  $V_g = 0$  V and  $+30$  V. The PL spectra showed the intensity of the "main peak" at  $V_g = 0$  V was decreased considerably upon application of a gate voltage  $V_g = +30$  V. The inset shows that the intensity of "defect peak" at  $V_g = 0$  V changed slightly upon application of a gate voltage  $V_g = +30$  V.

## LIST OF TABLES

**Table 6.1.** Parameters describing the fit of the semi-empirical model to the observed  $MR$  values for various gate voltages at  $T = 2$  K.

**Table 6.2.** Parameters describing the fit of the semi-empirical model to the observed  $MR$  values for various temperatures at  $V_g = -40$  V and  $-30$  V.

**Table 6.3.** Parameters describing the fit of the semi-empirical model to the observed  $MR$  values for various temperatures at  $V_g = +40$  V and  $+50$  V.



# Chapter 1

## Introduction

---

### 1.1 Spintronics

With the scaling of CMOS technology reaching to its fundamental limits, there are several new technologies are being actively explored as potential replacements. Among them, Spintronics or spin electronics is an area of research which exploits the spin (angular momentum) properties of electron instead or in addition to charge degree of freedom, considered to be a promising direction for the post CMOS era.<sup>1</sup> In spintronics, the major challenges are the measuring electron spin lifetimes, transport of spins across relevant length scales and detection of spin coherence in nanoscale systems and interfaces. The utilization of spin property as spin up (one state) and spin down (zero state), make the way to perform the Boolean logic operations to realize the computer chips based on spintronic devices. However, to be able to realize spintronics based computer chips it is necessary to build fundamental spintronic devices in which spin state can be manipulated.

Spintronic devices are well suited for realizing memories that are highly dense and non-volatile. Compared to the CMOS counterparts such as SRAM and DRAM, the spintronic memories have low leakage current and therefore have greater potential to revolutionize the storage and computing capabilities of future systems. In 2007 Nobel Prize in physics has been awarded to Albert Fert and Peter Grunberg for their independently discovered giant magnetoresistance (GMR) effect in 1988.<sup>2,3</sup> This discovery is considered to be the beginning of the new generation of the spin based electronics. After the discovery of GMR effect, read heads of hard disk drives were commercialized, where the GMR sensor reads the data written on the disc. For an extension of GMR effect, the TMR effect was discovered in which an insulating barrier is separated by the two ferromagnetic layers. This invention gives the way to extend the research by incorporating various nonmagnetic materials as a channel between the two ferromagnetic layers for spin transport mechanism. In 1985, Johnson and Silsbee was first performed experiments and realized spin valve device in which aluminum (Al) is used as a spin transporting channel.<sup>4,6</sup> In this type of so called spin valves, the resulting spin signal may include spurious signals such as Hall and AMR effects<sup>7,8</sup> which are quite similar to the spin valve signals. Later Jedema et al used the nonlocal spin detection technique to eliminate the spurious signal contribution from the spin signal. In his study, he used Al and Cu to investigate the spin

transportation.<sup>9-11</sup> Followed by this research, the same non-local technique has been used to perform spin transport studies in various nanostructures, for example in a graphene layer,<sup>12</sup> carbon nanotube,<sup>13</sup> and several semiconducting nanowires, such as germanium<sup>14</sup>, silicon<sup>15, 16</sup> and other III-V NWs.<sup>17, 18</sup>

After the preliminary realization of spin property and its potential benefits in spintronics, Datta and Das proposed the most prominent device proposal called spin field effect transistor (spin-FET)<sup>19</sup> in the late 1989 and opens a new gateway to spin information processing<sup>20, 21</sup>. According to Datta and Das spin FET proposal, the Rashba spin-orbit<sup>22</sup> coupling serves as the ingredient to perform controlled rotations of spins of electrons passing through the channel layer in a FET-type device. Although the ability of manipulation of electron spins in semiconductors is now possible<sup>23-27</sup>, the realization of a fully functional spin-FET for information processing is yet to be realized, owing to several fundamental challenges such as the low spin injection efficiency due to resistance mismatch, spin relaxation and the spread of spin precession angles. In order to avoid conductivity mismatch problem one possibility is that incorporation of tunnel barrier between ferromagnetic electrode and semiconductor channel, for efficient spin injection by spin dependent tunneling process. Other possibility is the development of ferromagnetic semiconductors or diluted magnetic semiconductors (DMS) for source and drain materials in order to rule out conductivity mismatch problem.

## 1.2 Diluted Magnetic semiconductors (DMSs)

As we discussed in the previous section, the first generation of spintronics devices were based on passive magnetoresistive sensors and memory elements using electrodes made from alloys of ferromagnetic 3d metals. Their development was later boosted by the discovery of giant magnetoresistance and tunneling magnetoresistance.<sup>28</sup> Next generation is expected to consist on active spintronic devices that will necessarily comprise the creation and manipulation of spin-polarized electrons in a host semiconductor<sup>21</sup>. In order to achieve an operational device, the electrons must be spin-polarized and their polarization largely preserved as they travel through the semiconductor material. For achieving this, there are a few complications and challenges which need to be seriously addressed,

- The most obvious way for spin injection would be injecting from a FM metal in a metal/SC junction. This type of heterostructures have been extensively studied; however, it has been shown that it is difficult to preserve the electron spin across the interface, mainly due to the large mismatch in electrical conductivity between the two materials.

- It is difficult to realize such a device because semiconductors currently used in integrated circuits, transistors and lasers, such as silicon and gallium arsenide are nonmagnetic. Moreover, the magnetic fields that would be required to have a useful difference in the energy between the two possible electron spin orientations (up and down) are too high for everyday use.
- Therefore, the design of materials combining both SC and FM properties turns to be crucial in the development of such devices and presents a serious materials physics challenge.

In this prospective the magnetic semiconductors are important ingredient to realize future spintronic devices. Moreover, magnetic semiconductors should allow easier integrability with the existing semiconductor technology, and would be vital for signal amplification with highly spin-polarized carriers. However, for realization of semiconductor spintronics, significant challenges related to the lifetime, control and detection of spin polarized carriers is seriously addressed. Also, one more important criteria is that realization of diluted magnetic spintronic device above room temperature is also one of the biggest challenges to meet.

Magnetic semiconductors are much needed materials in spintronic applications, due to its ability of coexistence of both ferromagnetism and important semiconducting properties. In 1980s, the first DMSs to be identified were II-VI semiconductor alloys<sup>29</sup> with very low Curie temperatures of about a few K.<sup>30</sup> Later, during the investigations of ferromagnetism in Mn-doped III-V semiconductors.<sup>31-35</sup> a relatively high  $T_c$  of 173 K was achieved in Mn-doped GaAs.<sup>36, 37</sup> It is observed that, in all these materials carrier mediated ferromagnetism was proven to be the source of ferromagnetism and which even enables the modifications of magnetism through charge manipulation. This has motivated a continuous search for materials with even higher  $T_c$  and carrier mediated ferromagnetism. It is point out that, the oxide based DMS have the capability of high electron doping and would be the key material for future spintronic devices with high  $T_c$  value (above room temperature).<sup>38</sup> In this direction, Matsumoto et al.<sup>39, 40</sup> have achieved the groundbreaking discovery of RT ferromagnetism in Co doped  $\text{TiO}_2$ . Later many research groups started investigations in other oxide based DMS such as TM-doped  $\text{ZnO}$ <sup>41</sup>,  $\text{SnO}_2$ <sup>42</sup>,  $\text{Cu}_2\text{O}$ <sup>43</sup> and  $\text{In}_{1.8}\text{Sn}_{0.2}\text{O}_3$ <sup>44</sup>. The detailed summary of high  $T_c$  oxide-based DMS can be found elsewhere<sup>45</sup>.

Among the various DMSs, ZnO is a promising spin source since it epitomizes DMS with  $T_c$  well above room temperature (RT). In particular, magnetization of ZnO can be induced by either transition ion doping and/or by intrinsic defects, such as oxygen vacancy ( $V_O$ ) and zinc vacancy ( $V_{Zn}$ ). In particular,  $V_O$ -induced RT ferromagnetism in as-grown ZnO nanowires (NWs) has been well established<sup>46-50</sup>. The  $V_O$ -induced emissions in the photoluminescence (PL) spectra in as-grown ZnO NW are always concomitant with the presence of ferromagnetism<sup>46-50</sup>. The presence of  $V_O$  defects as well as ferromagnetism in ZnO can be eliminated by annealing the ZnO in an oxygen environment, and these features can be even resurrected by vacuum annealing<sup>48, 51</sup>. It has been shown that formation of  $V_O$  energetically attracts interstitial Zn ( $I_{Zn}$ )<sup>52</sup>. While the former presents as a deep level trap, the latter forms a shallow donor level. Thus, the pair creation of defects causes ZnO to be a primarily  $n$ -type semiconductor<sup>52</sup>. An electron spin resonance (ESR) study showed that singly charged deep levels from  $V_O$  can host unpaired electron spins<sup>53</sup>. Recent study revealed native  $V_{Zn}$  and/or defect complexes involved with  $V_{Zn}$  can also derive the appearance of ferromagnetism in ZnO<sup>54, 55</sup>. Whether the main source of spin moments is  $V_O$  or  $V_{Zn}$  should depend on the sample growth method in this material. The origin and mechanism of this  $d^0$  ferromagnetism need to be further studied. In general, charge transport in ZnO NWs strongly relies on the native doping level and varies from hopping to the weakly localized limit<sup>56, 57</sup>. Thus, the magnetic exchange interaction between randomly distributed defect-induced spins is also subject to the doping concentration. Recent studies have suggested two different mechanisms<sup>58</sup> for ferromagnetic ordering in transition metal-doped ZnO: one is the formation of bound magnetic polarons in the localized limit<sup>45, 59, 60</sup> and the other involves carrier-mediated exchange interactions in the metallic regime<sup>61</sup>. It would be intriguing to probe how the gate-controlled carrier concentration affects the spin exchange in this unique magnetic semiconductor system.

### 1.3 Scope of thesis

In this thesis, I present experimental work on gate-tunable magnetotransport studies in ferromagnetic ZnO nanowire field effect transistor (FET) devices. Particularly I display the dramatic gate voltage tuning of magnetoresistance in ferromagnetic ZnO NW due to carrier mediated spin exchange interactions. Here, ZnO nanowires (NWs) used in this thesis were grown by chemical vapor deposition (CVD) technique and further characterized by various characterization techniques. I also present gate dependent photoluminescence (PL) study on single ferromagnetic ZnO NW devices. The chapters in this thesis are:

#### Chapter 2:

Some basic theoretical concepts of spintronics are introduced. Particularly I discuss the concepts of various magnetoresistance effects occurs in normal metals, ferromagnetic metals, non-magnetic semiconductors and magnetic semiconductors. I also discuss briefly about the spin orbit interaction induced magnetoresistance effects such as anomalous Hall effect (AHE) and spin Hall Effect (SHE). I also briefly discuss about the electric field controlled magnetism in DMS.

#### Chapter 3:

Here I describe the fabrication techniques used for the production of single ferromagnetic ZnO nanowire field effect transistor (FET) devices. Also a large part of the chapter is used to discuss a number of experimental and characterization techniques used to develop this thesis.

#### Chapter 4:

Here I discuss the growth and characterization of ZnO NWs. ZnO NWs used in this thesis were grown by chemical vapor deposition (CVD) technique. The crystal structure and composition of ZnO NWs were studied by X-ray diffraction (XRD), high-resolution transmission electron microscopy (HRTEM), and X-ray photoelectron spectroscopy (XPS).

Furthermore, I also present the magnetic properties of as grown ZnO NWs grown by CVD method. The magnetic property was observed from 300K to 10K by using super conducting quantum interface device (SQUID). The ferromagnetism in our ZnO NWs was observed well above the room temperature.

#### Chapter 5:

In this chapter I present the fabrication and characterization of ZnO nanowire FET devices. The measurements at room temperature show that good ohmic contact between Ti/Au and ZnO NW which leads

to the estimated mobility of  $\sim 32.5 \text{ cm}^2/\text{V}\cdot\text{s}$ . The temperature dependent conductivity and estimated carrier concentration at  $V_g = 0 \text{ V}$  reveal that, the studied ZnO NWs in this thesis were natively doped and lies at the crossover of the metal-insulator transition.

#### Chapter 6:

In this chapter I present the gate-tunable magnetotransport studies on single ferromagnetic ZnO nanowire FET devices. Upon sweeping the gate bias from  $-40$  to  $+50 \text{ V}$ , the MRs estimated at  $2 \text{ K}$  and  $2 \text{ T}$  were changed from  $-11.3\%$  to  $+4.1 \%$ . Detailed analysis on the gate dependent MR behavior clearly showed enhanced spin splitting energy with increasing carrier concentration. I also present the results of threshold voltage dependent behavior of magnetoresistance values, which were collected from the various device performances.

Chapter 7: Here I discuss the results of gate-tunable photoluminescence (PL) study on single ferromagnetic ZnO NW FET devices. Gate voltage dependent PL spectra of an individual NW device confirmed the localization of oxygen vacancy-induced spins, indicating that gate-tunable indirect exchange coupling between localized magnetic moments played an important role in the remarkable change of the MR, discussed in chapter 6.

## Chapter 2

# Spintronics: Magnetoresistance overview

---

### 2.1. Introduction

Spin-based electronics, or spintronics, refers to the study of the role played by the intrinsic spin of the electron in solid state physics, and possible devices which are specifically exploit spin properties instead of or in addition to charge degree of freedom. Currently spin transport electronics including spin injection, transport with its precession control and detection is currently a hot topic, which offers opportunities for a new generation of multifunctional devices.

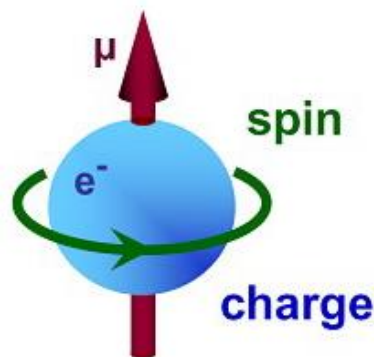


**Figure 2.1.** Schematic illustration of electron spin with net magnetic moment  $\mu$  and charge  $e$ .

In spintronics, magnetoresistance (MR), the change of material's resistance with the application of a magnetic field, is a well-known phenomenon. There are several different ways in which a magnetic field can affect hopping conductivity. The most obvious difference is between affecting it via spins and affecting it via the orbital motion. However, the magnetoresistance effect can be well observed in various materials including normal metals, ferromagnetic metal, normal semiconductor, ferromagnetic semiconductors, topological insulators and also in the organic materials. The observation of magnetoresistance effect can be enabled by various device geometries and approaches. This chapter dedicated to briefly outline the various types of magnetoresistance effects in spintronics.

## 2.2. Ordinary Magnetoresistance (OMR)

In a non-ferromagnetic metals, the presence of an externally applied field perpendicular to the current induces a Hall voltage in a direction orthogonal to both the current and magnetic field. An applied field causes a change in the longitudinal resistance of a material because the Hall effect causes charge carriers to deflect from the current direction. Due to the Lorentz force, the conduction electrons are forced into cyclotron orbits about the applied field. Once a charge carrier begins to orbit around the magnetic field, it no longer contributes to the current density until it is scattered. Once the conduction electron is scattered, it then begins its next cyclotron orbit, with an initial velocity biased towards the applied field.

The effect of an applied field on the electrical resistivity thus depends upon the original resistivity; the longer the relaxation time  $\tau$ , the larger the effect of an applied magnetic field. This is the ‘ordinary’ magnetoresistance effect which is analytically described by Kohler’s rule:

$$\frac{\Delta\rho}{\rho} \propto a \left( \frac{H}{\rho} \right)^2$$

Where  $\Delta\rho$  is the change in resistivity,  $\rho$  is the resistivity of the material in the absence of an applied field and  $H$  is the applied field and  $a$  is a constant of proportionality. Experimentally, it is observed that the change in resistivity  $\Delta\rho$  is maximum when the applied field and the electric current are perpendicular and a minimum (weaker effect) when they are parallel.<sup>62</sup>

In a ferromagnetic metals, this effect is often masked by the presence of a much larger phenomenon, known as the ‘extraordinary’ magnetoresistance effect. Due to the existence of strong spontaneous magnetization,  $M$ , in ferromagnetic metals, the extraordinary effects are much stronger than the normal metals. Also because of spin-orbit effects, the magnetization couples to the current density and there is an interaction between the spin and the orbit of the electron motion. Kohler’s rule can be extended for ferromagnetic materials as:

$$\frac{\Delta\rho}{\rho} \propto a \left( \frac{H}{\rho} \right)^2 + b \left( \frac{M}{\rho} \right)^2$$

Where  $b$  is a constant of proportionality.



### 2.3. Anisotropic Magnetoresistance (AMR)

The discussion of magnetoresistance effects in this section is restricted to the changes in electrical resistance in ferromagnetic metals associated with the direction of magnetization relative to the applied current: this is known as anisotropic magnetoresistance. This effect was discovered in 1857 by Thomson<sup>7</sup> and sometimes it is called as the orientation effect due to its dependence upon the orientation of the magnetization to the applied current. In general, the resistance of a ferromagnetic metal varies as:

$$\rho(\theta) = \rho_{\perp} + \Delta\rho \cos^2(\theta)$$

The change in resistivity  $\Delta\rho$  is a minimum when the magnetization and the electric current are perpendicular ( $\rho_{\perp}$ ) and is a maximum when they are parallel ( $\rho_{\parallel}$ ).<sup>8, 63</sup> The values of  $\rho_{\parallel}$  and  $\rho_{\perp}$  can be measured experimentally in typical scans as shown in Figure 2.2. The change in resistivity between the parallel and perpendicular states,  $\Delta\rho$  is defined by the relation:

$$\Delta\rho = \rho_{\parallel} - \rho_{\perp}$$

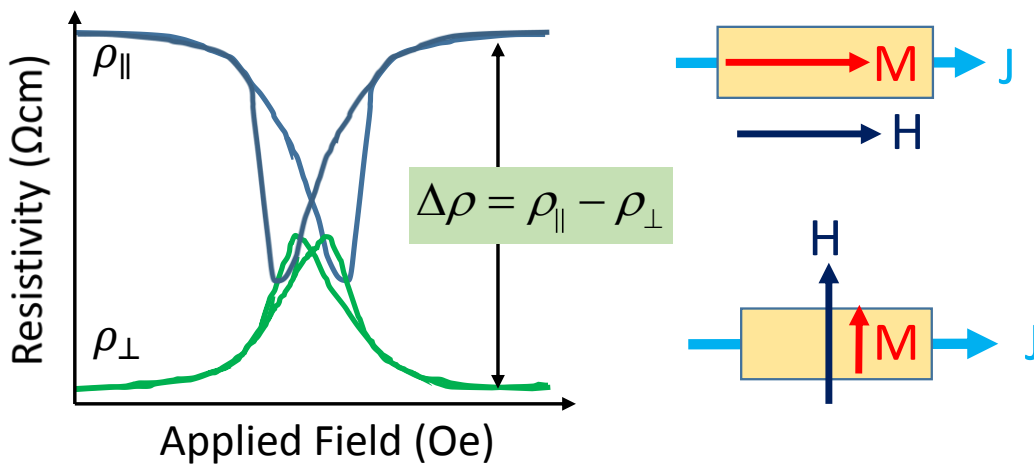


**Figure 2.2.** The typical anisotropic magnetoresistance in a ferromagnetic metals and alloys and its corresponding schematics to show the orientation of magnetization and current density.

In contrast to OMR, the effect is anisotropic, where  $\Delta\rho_{\perp}$  decreases with field and  $\Delta\rho_{\parallel}$  increases with field.

## 2.4. Giant Magnetoresistance (GMR)

Giant Magnetoresistance (GMR) is a quantum mechanical magnetoresistance effect in which the magnetic multilayers are composed of an alternative stack of thin magnetic and nonmagnetic layers. The magnetic layers are coupled through the nonmagnetic layers in either a ferromagnetic or antiferromagnetic configuration depending on the thickness of the nonmagnetic layers. In 2007 Nobel Prize in physics has been awarded to Albert Fert and Peter Grunberg for their independently discovered giant magnetoresistance (GMR) effect in 1988.<sup>2,3</sup> This discovery is considered to be the beginning of the new generation of the spin based electronics. After the discovery of GMR effect, read heads of hard disk drives were commercialized, where the GMR sensor reads the data written on the disc. Figure 2.3 (b) shows the structure of magnetic multilayers composed of magnetic (Fe) and nonmagnetic (Cr) superlattices and Figure 2.3 (a) shows its corresponding magnetoresistance curves at  $T = 4.2$  K. The magnetoresistance value of -50% was observed.

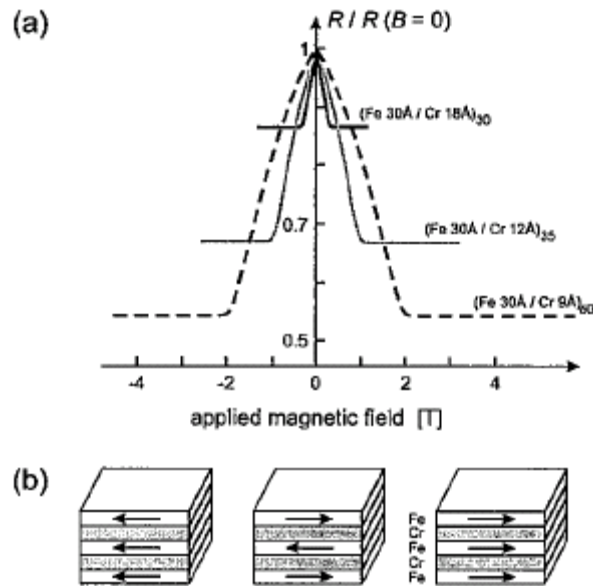


**Figure 2.3.** Magnetoresistance of three Fe/Cr superlattices at 4.2K. Here the current flow direction and the applied magnetic field are along the [110] axis in the plane of the layers<sup>2</sup>

The GMR effect requires two important characteristics. (1) The change of relative orientation of the magnetization in magnetic layers could be easily controlled by an external magnetic field. (2) The thickness of films must be less than the mean free path of the electrons.

## 2.5. Tunneling Magnetoresistance

Tunneling magnetoresistance (TMR) effect is an extension to the GMR effect, in which the magnetoresistance is governed by the similar quantum mechanical laws. The schematic representation of TMR effect is shown in Figure 2.4, where the two magnetic layers are separated by a thin insulating layer and a bias voltage is employed to pass the current between two ferromagnetic layers. The change of tunneling current in magnetic tunnel junctions depends on the relative magnetizations of the two ferromagnetic layers. TMR effect is larger than GMR effect by about a factor of 10 and currently being exploited as a better mechanism for read heads of modern hard disk drives, TMR or magnetic tunnel junction, is also the basis of MRAM, a new type of non-volatile memory, logic devices and sensors.

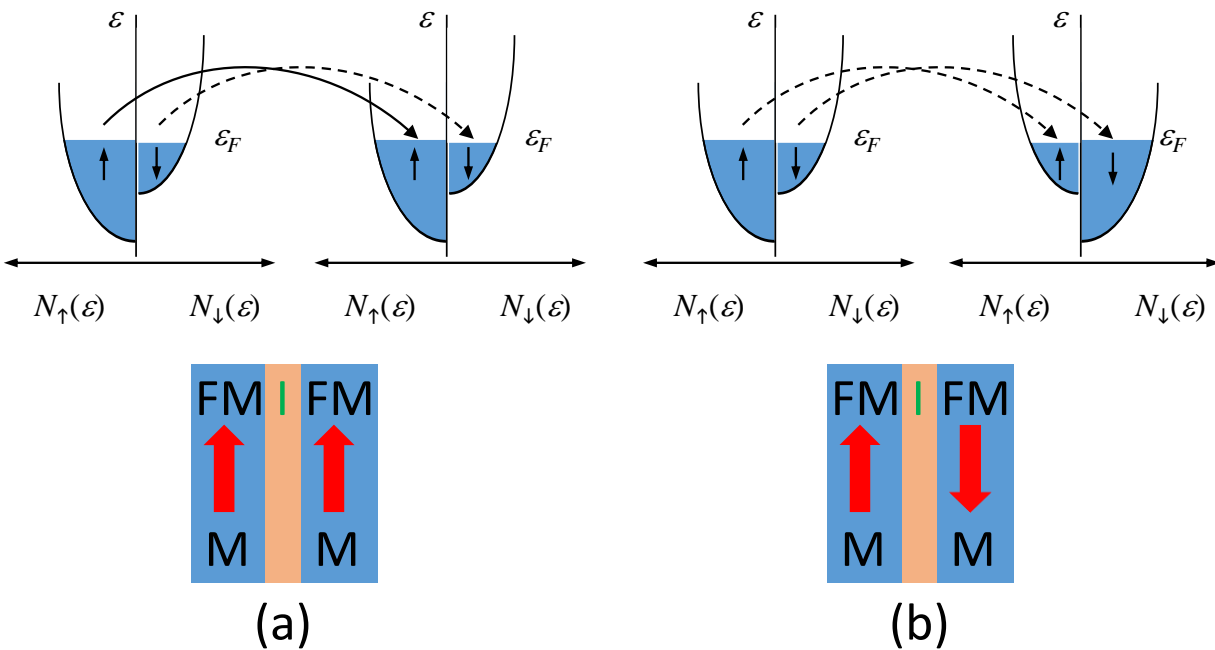


**Figure 2.4.** Schematic illustration of the tunneling magnetoresistance (TMR) effect by means of spin dependent tunneling. In a magnetic tunnel junction, the density of states of both ferromagnetic layers determines whether a large current (a) or small current (b) tunnel through.

Ferromagnetic materials consists of intrinsic magnetization due to the different density of states for up and down spins. It means that the spin states available for one spin orientation higher than the other. The spin transport takes place in this device based on the quantum mechanical tunneling after applying a bias across the barrier. The basic working principle is that due to the application of bias voltage across the barrier, electrons will tunnel from the FM1-FM2 via tunnel barrier depending on the availability of free states for that particular spin orientation. As shown in Figure 2.4, if the two magnetic layers are parallel 2.4 (a), a majority of electrons in FM1 will find many states of similar orientation in the other FM2, causing a large current to tunnel through and a lowering of overall resistance. If two magnetic layers are anti parallel 2.4 (b), both spin directions will encounter a bottleneck in either of the two ferrimagnets, resulting in a higher total resistance.

The tunneling current between the two electrodes separated by an insulating barrier can be calculated on the basis of Fermi's golden rule.

$$I = 2e \frac{2\pi}{\hbar} \int_{-\infty}^{\infty} |M(E)| N_1(E - eV) N_2(E) [f(E - eV) - f(E)] dE$$

Where,  $N_1$ ,  $N_2$  are the density of states for up and down spins.

## 2.6. Magnetoresistance in a non-local spin valve

In 1985, Johnson and Silsbee introduced the concept of spin valve during their study of spin accumulation in metals,<sup>4</sup> and developed extensively by other research groups for spin transport and detection in metals,<sup>9, 10</sup> GaAs,<sup>25, 64</sup> Si,<sup>65, 66</sup> and graphene.<sup>12</sup> Figure 2.5 shows the typical nonlocal spin valve (NLSV) geometry used to detect pure spin currents and also to estimate the spin lifetimes via the Hanle effect.

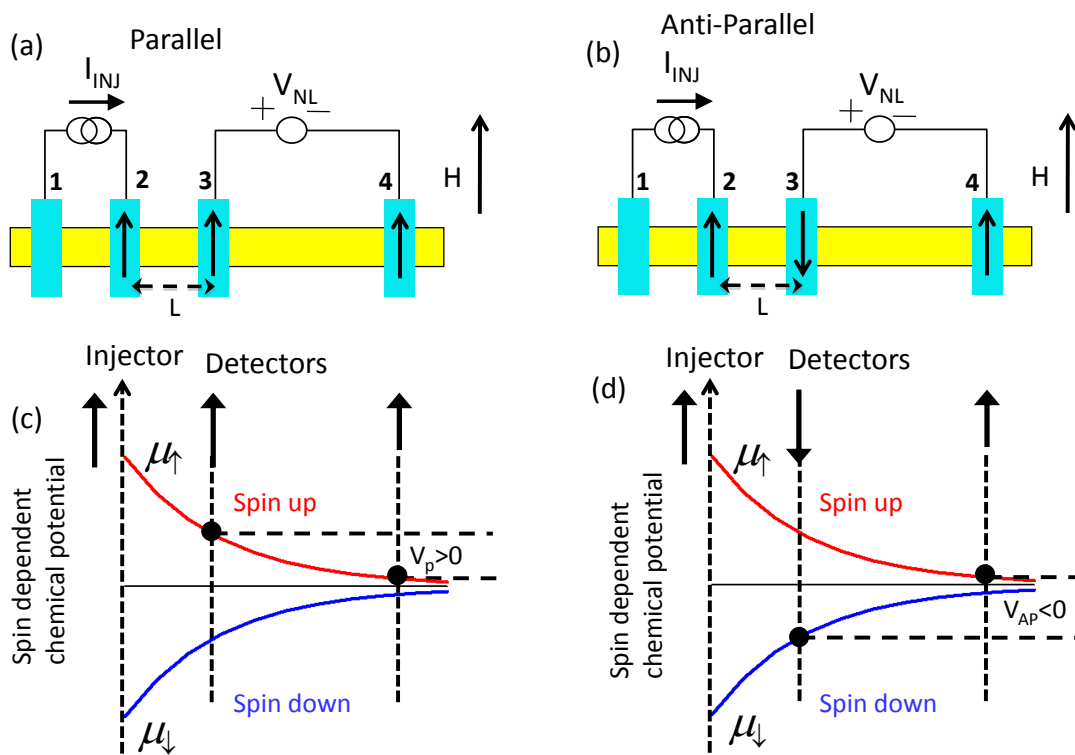


**Figure 2.5.** (a-b) Schematic view of four terminal NLSV device with (a) parallel and (b) antiparallel magnetization of the spin injector and detector. (c-d) The spin splitting of the electrochemical potential  $\Delta\mu$  corresponding spin accumulation produced by spin injection from contact 2. Depending on the direction of magnetization, the  $V_{NL}$  measured at contact 3, either spin up (c) or spin down branch (d) of the chemical potential.

The concept is based up on the fact that, the generated spin from the point of contact will diffuses away independently of the direction of charge current path. As shown in Figure 2.5, the FM metal with tunnel barrier contact 2, inject a spin polarized current into the semiconductor channel. When a bias current applied between contact 1 and 2, the spin polarized current will diffuse into the semiconductor channel and travel to the detector contact 3, which is placed outside of the contact 1 and 2. The detector contact 3 senses the spin-splitting of the chemical potential,  $\Delta\mu = \mu_{\uparrow} - \mu_{\downarrow}$  corresponding spin accumulation resulting from spin diffusion away from the FM injector, contact 2.<sup>67</sup>

Once the spin is accumulated from the injector ferromagnetic contact, it decays with increasing distance from the injector contact with a certain spin diffusion length  $\lambda_{sf}$ . The voltage obtained at the detector contact of FM 3 is proportional to the difference of chemical potential  $\Delta\mu$  and the projection of the semiconductor spin polarization onto the contact magnetization. Therefore one can use some mechanism to manipulate the semiconductor spin polarization (magnitude or orientation) to encode or process information with the pure system, and directly read out the result as a voltage at this third contact.<sup>67</sup>

There are two key concepts to be familiar in NLSV geometry:

- Separate and distinguish a pure spin current from a spin polarized charge current
- The efficient detection of a real voltage induced by the spin accumulation.

The nonlocal magnetoresistance can be defined as,

$$MR = \frac{(V_P - V_{AP})}{I_{INJ}}$$

where,  $V_P$  and  $V_{AP}$  are the sensing voltages when magnetizations of injecting and detecting ferromagnets are parallel and anti-parallel, and  $I_{INJ}$  is the injection current.

### Nonlocal magnetoresistance in nanowire based spin valves:

Nanowire spintronic devices embrace possible applications based on carrier control and tunable spin-orbit interaction. Hence, spin injection, detection, and control of spin in accessible manner in these nano devices is particular interest. In this direction, several semiconducting nanowires, such as germanium<sup>14</sup>, silicon<sup>15, 16</sup> and other III-V NWs,<sup>17, 18</sup> have been explored for the spin transport channel in a nonlocal spin valve (NLSV) geometry.

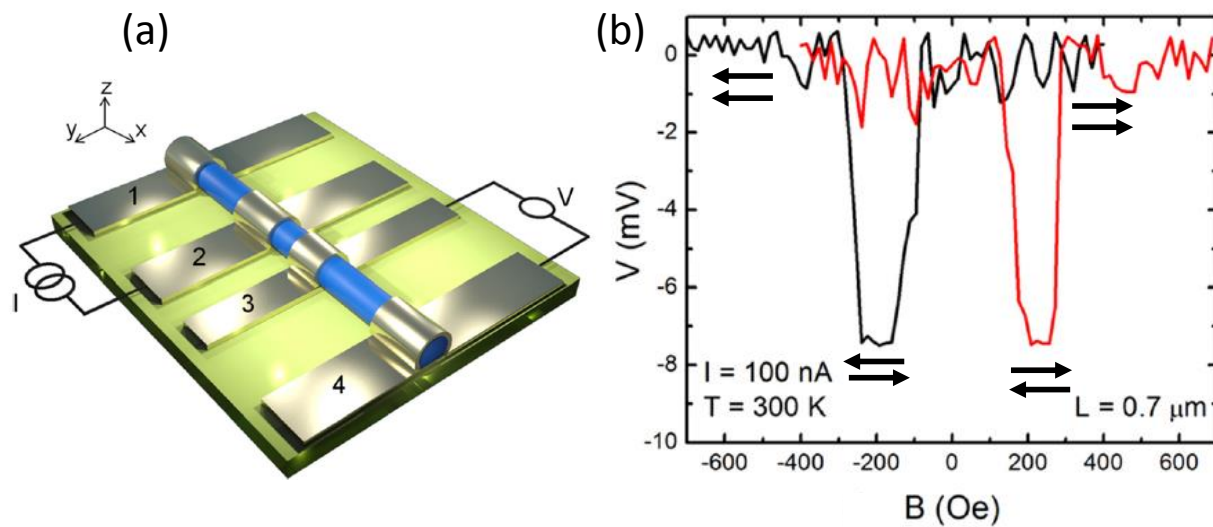


**Figure 2.6.** (a) Schematic layout of the four terminal NLSV. (b) Nonlocal magnetoresistance characteristic of the GaN nanowire at room temperature under in plane magnetic field. The arrows indicate the relative orientation of the injector (contact 2) and detector (contact 3).<sup>27</sup>

## 2.7. Magnetoresistance due to weak localization (WL)

In metal or semiconductors system weak localization effect is caused by the constructive interference of two phase coherent electronic waves propagating in opposite directions along a same closed trajectory.<sup>68-70</sup> This effect gives rise to a suppression of conductivity. When a magnetic field is applied perpendicular to the system, the constructive interference is broken as a result of a phase difference between the two electronic waves. The suppression of conductivity is gradually removed in increasing the magnetic field consequently a positive magneto conductivity appears usually within in a small magnetic field window around 0 T. The effect displays itself as a positive correction to the resistivity of a metal or semiconductor. This is shown in Figure 2.7(a).

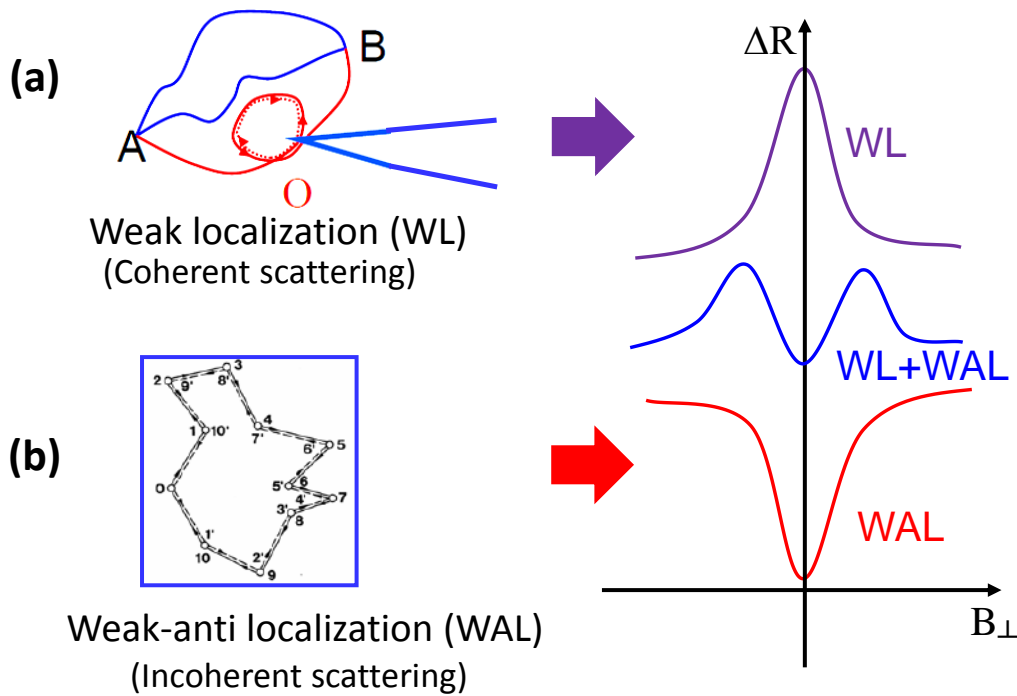


**Figure 2.7.** Transport in a diffusive regime: (a) Weak localization due to constructive interference. (b) Weak-anti localization due to incoherent scattering of electron waves.



However, the WL effect is sensitive to the spin-orbit interaction. In a system with spin-orbit coupling the spin of a carrier is coupled to its momentum. The spin of the carrier rotates as it goes around a self-intersecting path, and the direction of this rotation is opposite for the two directions about the loop. Because of this, the two paths along any loop interfere destructively which leads to the change of sign in magnetoconductivity. This is referred as the weak anti localization effect<sup>70</sup> shown in Figure 2.7(b). In general WL & WAL effect is used to measure dephasing, spin-orbit scattering, tunneling times, etc.

The appearance of weak anti localization in a two-dimensional system is thus suggestive of the presence of spin-orbit coupling. The Hamiltonian for this coupling is given by

$$H(k) = \hbar \boldsymbol{\sigma} \cdot \boldsymbol{\Omega}(k)$$

Where  $\boldsymbol{\sigma}$  is the vector Pauli matrices,  $k$  is the electron wave vector and  $\boldsymbol{\Omega}$  is an odd function of  $k$ .

In the case of two dimensions, Hikami-Larkin Nagaoka equation<sup>70</sup> for the change of conductivity due to WL or WAL takes the following expression.

$$\begin{aligned} \sigma(B) - \sigma(0) = & + \frac{e^2}{2\pi^2\hbar} \left[ \ln\left(\frac{B_\phi}{B}\right) - \psi\left(\frac{1}{2} + \frac{B_\phi}{B}\right) \right] \\ & + \frac{e^2}{\pi^2\hbar} \left[ \ln\left(\frac{B_{SO} + B_e}{B}\right) - \psi\left(\frac{1}{2} + \frac{B_{SO} + B_e}{B}\right) \right] \\ & + \frac{3e^2}{2\pi^2\hbar} \left[ \ln\left(\frac{(4/3)B_{SO} + B_e}{B}\right) - \psi\left(\frac{1}{2} + \frac{(4/3)B_{SO} + B_e}{B}\right) \right] \end{aligned}$$

Where  $\psi$  and  $B_\phi$  corresponds to the digamma function and the phase coherence characteristic field.  $B_{SO}$  is the spin-orbit characteristic field and  $B_e$  in the elastic characteristic field.

When in the limit of strong spin orbit coupling  $B_{SO} \gg B_\phi$ , the above equation simplified to the following form:

$$\sigma(B) - \sigma(0) = \alpha \frac{e^2}{2\pi^2\hbar} \left[ \ln\left(\frac{B_\phi}{B}\right) - \psi\left(\frac{1}{2} + \frac{B_\phi}{B}\right) \right]$$

Where, the value of  $\alpha$  is -1 for WL and +1/2 for WAL.

## 2.8. Spin-orbit interaction and Hall effects

SOI refers to the coupling of spin with the orbital motion of electrons. In addition to AMR, SOI also gives rise to the other interesting transport properties called as anomalous Hall effect (AHE) and spin Hall effect (SHE) as well as electric field-induced spin accumulation in two-dimensional electron gas (2DEG).<sup>71</sup> Although most of the theoretical studies are on bulk systems, there are several experimental studies are performed on mesoscopic or nanosize systems. In this section, the concepts of SOI, AME and SHE are briefly discussed.

### 2.8.1. Spin-orbit interaction

SOI and its corresponding Hamiltonian is given by

$$H_{so} = -\frac{e\hbar}{4m^2c^2} (\boldsymbol{\sigma} \cdot [\mathbf{E} \times \mathbf{p}])$$

$$\simeq \frac{e\hbar}{2m^2c^2} \left( \frac{dV}{rdr} \right) (s.l)$$

Where  $E$  is an electric field induced by a potential gradient  $dV/dr$ ,  $c$  is the light velocity, and  $l$  is the orbital angular momentum. There are several origins of the internal electric field<sup>71</sup>:

- Inversion asymmetry of the lattice such as the zincblende structure. The SOI is called Dresselhaus-type SOI.<sup>72</sup>
- Inversion asymmetry of the structure such as the 2DEG. The SOI is called Rashba-type SOI.<sup>73</sup>
- $l-s$  coupling on atoms.
- Potential gradient caused by impurity potential and  $l-s$  coupling of atoms.

The first three types of SOI are known as intrinsic SOI since they exist in uniformly in the system, the last one is called an extrinsic SOI as it is caused by impurity potentials. The SOI in semiconductors is usually caused by the Dresselhaus and/or the Rashba-type SOI, while that in metal and alloys may be related to the  $l-s$  coupling.

### 2.8.2. Anomalous Hall effect

In 1879, the Hall effect was discovered by Edwin Hall,<sup>74</sup> during his studies about the force acting on a charged particle under an external electric ( $E_{\text{ext}}$ ) and a magnetic fields ( $H_{\text{ext}}$ ). This effect refers to the "ordinary" Hall effect. According to this effect, when the electrons travel under the influence of magnetic field, because of the Lorentz force the electrons will deflect into the direction of  $E_{\text{ext}} \times H_{\text{ext}}$ . If we talk about ferrimagnets, usually there are two contributions to the Hall effect, the "ordinary" Hall effect and the "anomalous" Hall effect (AHE). The Hall resistivity  $\rho_H$  is thus given as

$$\rho_H = R_0 H + 4\pi R_s M$$

In the above equation, the first term belongs to the ordinary Hall effect and the second term belongs to the anomalous Hall effect. The Coefficient  $R_0$  is known as the ordinary Hall coefficient and  $R_s$  is known as the anomalous Hall effect coefficient.

### 2.8.3. Spin Hall effect

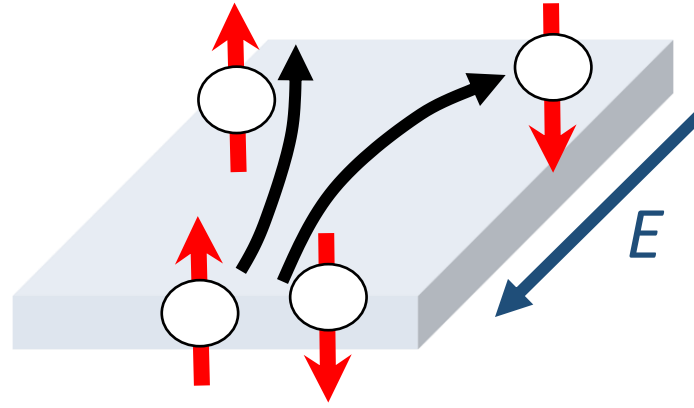


**Figure 2.8.** Schematic illustration of the spin hall effect.

For non-magnets, although the two charge Hall currents cancel and no Hall voltage develops, spin-dependent scattering still produces the up and down “spin” currents (flow of spins) that flow in the opposite directions, as long as the SOI is non-vanishing. Therefore we thus believe a Hall effect solely with spin, which is called spin Hall effect (SHE).<sup>71</sup> A schematic view of SHE is shown in Figure 2.8. The extrinsic SHE is responsible for the observed spin Hall current if it is originated from the scattering of electrons by impurity potentials with SO interaction.<sup>75, 76</sup> The spin Hall device studies are placed in a broader context of the field of spin injection, manipulation, and detection in non-magnetic conductors.

Apart from semiconductors, the SHE is also observed in transition metals and normal metals in which the SOI exists. The experimental observation of inverse SHE in Al, Pt was realized by few research groups,<sup>22, 77</sup> by injecting the spin-polarized current from ferromagnetic metal into a non-magnetic metal. A schematic illustration of the inverse SHE is shown in Figure 2.9. The injected spin current from ferromagnetic metal gives rise to a spin dependent chemical potential shift. Since the chemical potential shift decays with increasing the distance from the point of the spin injection, a Hall current is induced. Here, the spatial dependence of the spin-down and spin-up chemical potentials have opposite signs, and down-spin and up-spin Hall currents flow into opposite directions.<sup>71</sup> In a study of realistic tight-binding model, the large value of the spin Hall conductivity has also been predicted for Pt and transition metals.<sup>78, 79</sup>

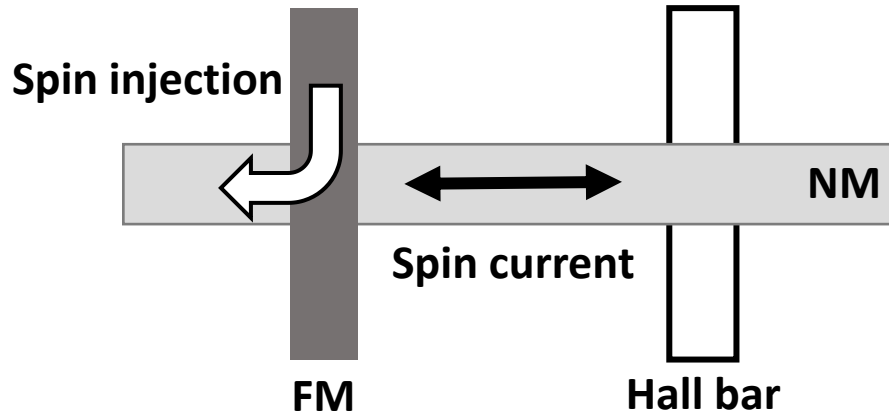


**Figure 2.9.** Schematic illustration of experimental setup to measure inverse SHE.

## 2.9. Control of magnetism by electric fields

The ultimate goal of 'spintronics' is to combine ferromagnets with semiconductors to develop the electronic devices that exploits the spin of electrons as well as charge. One aim is to integrate information storage with information processing, but a broader goal of spintronics is to develop new functionality that does not separately in a semiconductor or ferromagnet. Based on this motivation, the researchers are searching for 'emergent behavior' in combined ferrimagnet/semiconductors structures, in which the whole is more than the sum of its parts.<sup>80</sup> In this regard, in 2000 Ohno et al. provides a striking example of such behavior. In their invention, electrical manipulation of the magnetic phase transition was first observed in a thin film of magnetic semiconductor (In,Mn)As, which was used as a channel material in a field effect transistor.<sup>81</sup> This is shown in the above Figure. 2.10. The anomalous Hall effect has been used to probe the magnetization ( $M$ ), and the effect on this material from an applied electric field. Later on investigations into the electric field control of magnetism have expanded to cover a wide range of magnetic semiconductors<sup>80</sup> which are in the form of bulk or thin films, including group II-VI,<sup>82-84</sup> group III-V,<sup>81, 85-87</sup> group IV,<sup>88</sup> wide gap materials,<sup>89</sup> and topological insulators.<sup>90, 91</sup>

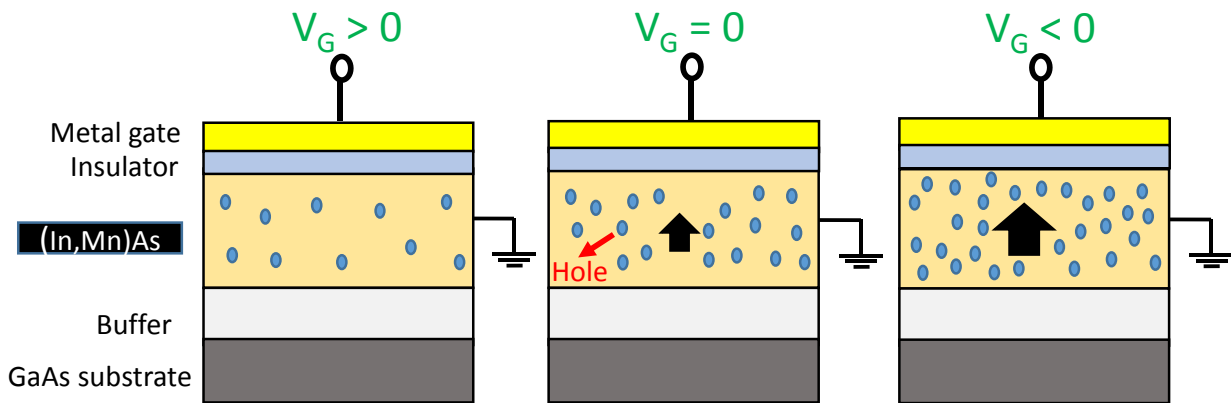


**Figure 2.10.** An electrically controlled magnetic switch designed by Ohno et al,<sup>81</sup> where the field effect control of the hole induced ferromagnetism in magnetic semiconductor (In,Mn)As field effect transistor. The cross section of the metal insulator semiconductor field effect transistor is shown in the above figure. The applied gate voltage ( $V_G$ ) controls the hole (filled circles) concentration in the semiconductor channel. Negative  $V_G$  increase the hole concentration, resulting in enhancement of ferromagnetic interaction among Mn ions, whereas the positive  $V_G$  has an opposite effect. The schematic arrow in the above figure shows the magnitude of the Mn magnetization. The buffer layer corresponds to the InAs/(Al,Ga)Sb/AlSb structure.

## Chapter 3

### Experimental Techniques

This chapter describes the experimental techniques applied in the research discussed in this thesis.

#### 3.1. Device fabrication procedure

This section introduced about the experimental procedure we approached in order to fabricate the high quality ZnO nanowire field effect transistor device to study the gate tunable magnetotransport properties.

Electron beam lithography was used to define multiple electrode on the nanowire (NW). The device fabrication procedure involves several steps and are displayed in the above Figure 3.1.

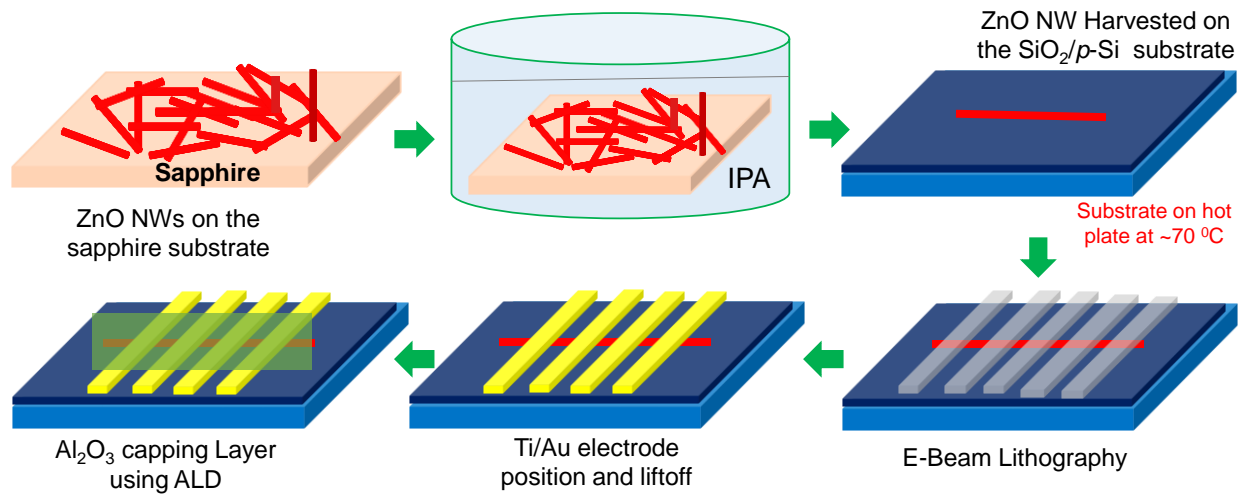


**Figure 3.1.** Experimental procedure for ZnO NW device fabrication

To fabricate the device:

- The as-grown ZnO NWs on sapphire substrate were suspended in IPA solution. A slight sonication was performed to extract the NWs from the sapphire substrate.
- While transferring nanowires on to the SiO<sub>2</sub> (300 nm)/*p*-Si substrate, the temperature of hot plate, on which the SiO<sub>2</sub> (300 nm)/*p*-Si substrate was maintained at 60<sup>0</sup>C ~ 70<sup>0</sup>C to evaporate the IPA solution quickly.
- The extracted NWs from the sapphire substrate were transferred onto a SiO<sub>2</sub> (300 nm)/*p*-Si substrate with a pre-defined number patterns as shown in Figure 3.2.
- The pre-defined number patterns on the SiO<sub>2</sub> (300 nm)/*p*-Si substrate as shown in Figure 3.2 was transferred by using photolithography. These number patterns serves as reference sites to find the position of the NW in the 1cmx1cm sample size.
- Explore the sample by using optical microscope/SEM to find the location of the suitable nanowire site to fabricate the device.
- Using AutoCAD software, the multiple electrodes were designed to the NW located site on the 1cmx1cm sample with the help of reference number patterns.
- After spin coating with PMMA resist, with the help of AutoCAD file consists of electrodes design and the reference patterns on the substrate, electron beam lithography defines the electrode patterns on the NW.
- After the electron beam lithography writing process, the sample was developed in MIBK: IPA solution. (see Figure 3.3 (a))
- The lithographically patterned sample was then transferred to the ALD chamber to perform Argon plasma treatment in order to remove the PMMA residues and the other contaminants at the contact area.
- After Argon plasma treatment the samples were immediately transferred to the high vacuum system incorporated with the electron beam and thermal evaporation electrode deposition techniques. The evaporation of titanium (Ti) adhesion layer is done by electron beam evaporator technique, and followed by this step the gold (Au) electrode was deposited using thermal evaporation technique.
- Followed by the electrode deposition, liftoff was performed to remove the unwanted PMMA and then using optical microscope/SEM the device was inspected.
- After the liftoff process, the device was transferred to the ALD chamber for annealing and Al<sub>2</sub>O<sub>3</sub> capping layer deposition.



- After takeout from the ALD chamber, the wiring was performed and then transferred to the PPMS chamber for the electric and magnetotransport measurements.



**Figure 3.2.** The image of Reference number patterns, transformed onto SiO<sub>2</sub> substrate to identify the location of nanowire while performing e-beam lithography.

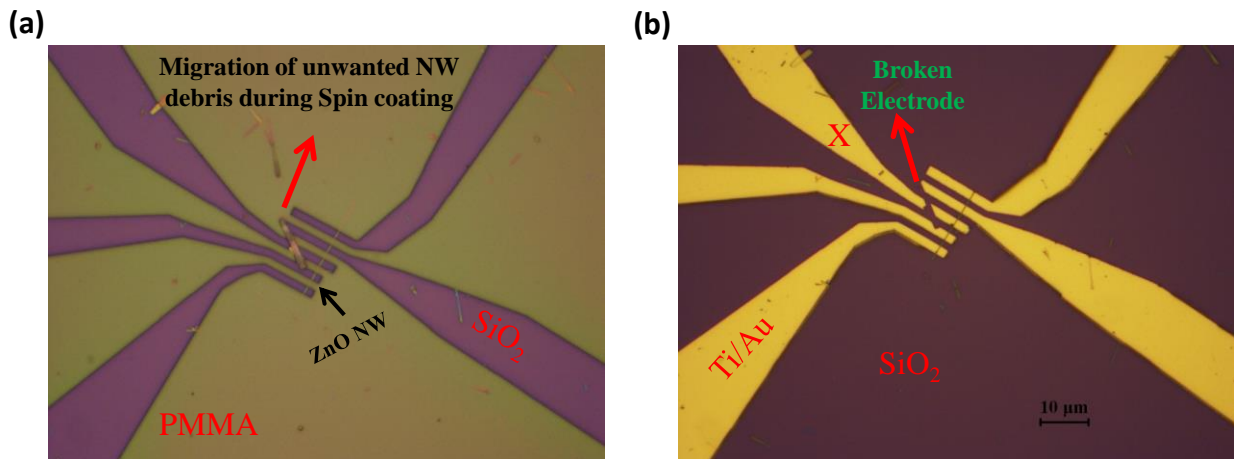
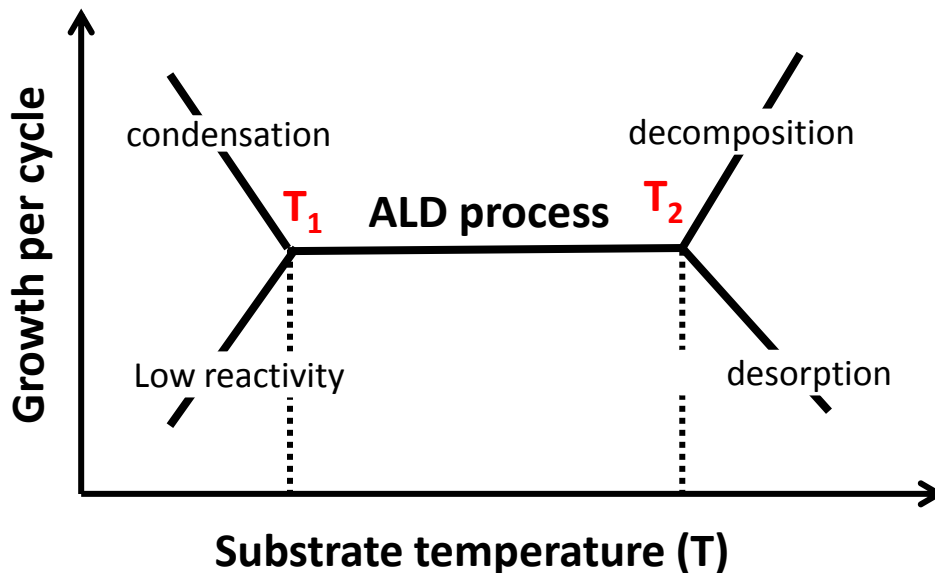


**Figure 3.3.** (a) Optical microscope image taken after the e-beam lithography processing and development. (b) Optical microscope image taken after the process of lift-off step. Figure (a and b) also shows that, during the spin coating process, sometimes the unwanted nanowire debris will migrate into the NW location and causes the electrode damage.

### 3.2. Atomic layer deposition (ALD)

Atomic layer deposition (ALD) is an advanced vapor phase technique used to coat high quality thin films on a desired substrates. In contrast to chemical vapor deposition (CVD) and physical vapor deposition (PVD), in ALD the deposition of high quality thin films is achieved based on the self-limiting surface chemical reactions. In ALD process, the intrinsic surface control mechanism is based on the saturation of an individual, sequential self-limiting surface reactions between the precursor molecules and the substrate surface. In CVD and PVD where the saturation mechanism takes place based on the time of growth or the concentration of reactant whereas in ALD process, the saturation mechanism takes place based on the number of reaction cycles. Due to its ability of layer by layer growth, the number of reaction cycles is proportional to the thickness of the film. Thus, ALD is particularly advantageous in depositing high quality ultrathin films with highly uniform and conformal coating for several applications. There is another advantage of ALD is that the film can be deposited at lower substrate temperatures compared to the CVD process. However, there is a so called temperature window for the ALD process; because, the adsorption of precursor to the desired surface is mainly thermally driven.

The above schematic shows the general temperature window of an ALD process.



In order to prevent the condensation of any of the reactants, the substrate temperature must be required greater than  $T_1$  (high enough) at which ALD process will takes place. If condensation happens during an ALD cycle, uncontrollable or undesired chemical reactions might happen, resulting in the formation of impure and porous films. However, if the temperature is too high (greater than  $T_2$ ) an undesirable

decomposition of reactants will occur. Furthermore at very large temperatures (greater than  $T_2$ ), CVD reactions will take place and because of this uncontrollable and undesired film depositions will occur. Moreover, there is an effect which might exist more likely at higher temperatures called as re-evaporation effect, causes the decreasing growth per cycles versus temperature.

### **Mechanism:**

To demonstrate the underlying mechanism of ALD processes, a deposition process of  $\text{Al}_2\text{O}_3$  using trimethylaluminum (TMA) and water ( $\text{H}_2\text{O}$ ) precursor is shown in Figure 3.4.

The deposition of  $\text{Al}_2\text{O}_3$  by using ALD process takes four repetitive steps:

- (1) Aluminum source TMA precursor induce surface reactions with the reactive sites (OH groups figure (a)) on a substrate and form an intermediate layer. The intermediate layer will form by release of  $\text{CH}_4$  as the byproduct (figure (b and c)).
- (2) A purging phase following the self-terminated reaction to evacuate the over supplied non reacted TMA and gaseous byproduct  $\text{CH}_4$ .
- (3) Supply of oxygen precursor  $\text{H}_2\text{O}$  to start a second surface reaction ( figure (d) ) with the reactive groups of the intermediate layer to produce target  $\text{Al}_2\text{O}_3$  as well as new active sites (OH groups figure (e))
- (4) Another purging phase to evacuate the non-reacted oversupplied  $\text{H}_2\text{O}$  precursor and gaseous byproduct  $\text{CH}_4$ .

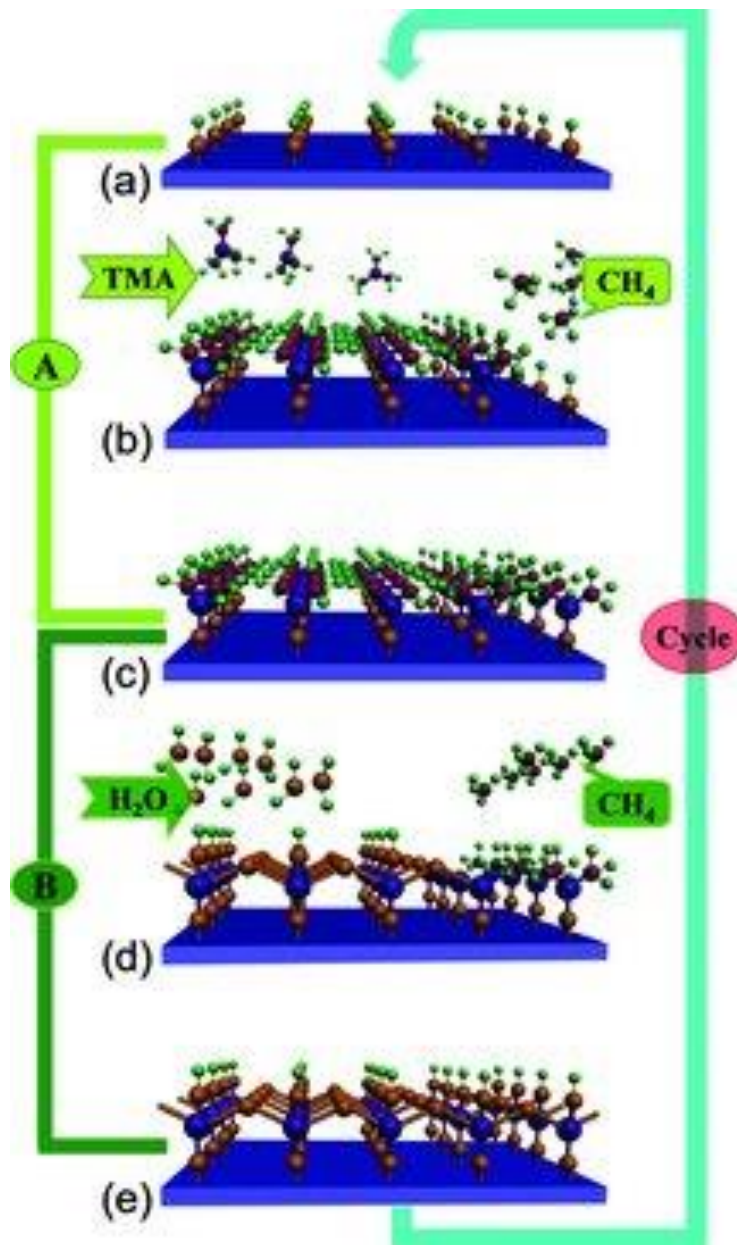


**Figure 3.4. The visualization of ALD process by depositing  $\text{Al}_2\text{O}_3$  using TMA and  $\text{H}_2\text{O}$  precursors.**

(a) The surface of the substrate initially covered with hydroxyl groups. (b) Formation of new intermediate layer after reacting TMA molecules with hydroxyl groups. (c) The substrate covered with new intermediate layer. (d) Reaction between  $\text{H}_2\text{O}$  molecules and intermediate layer, leading to the target  $\text{Al}_2\text{O}_3$  and new hydroxyl groups. (e) The substrate again covered by hydroxyl groups. [Reproduced from Meng, X.B. et al., 2012.<sup>92</sup>]

**Experimental set up:**

The experimental setup for ALD (SVTA ALD system) is shown in the above Figure 3.5. The SVTA ALD system is a versatile research deposition tool for thermal or plasma enhanced ALD. The ALD system is integrated with the RoboALD automation software, which increases the process reproducibility.

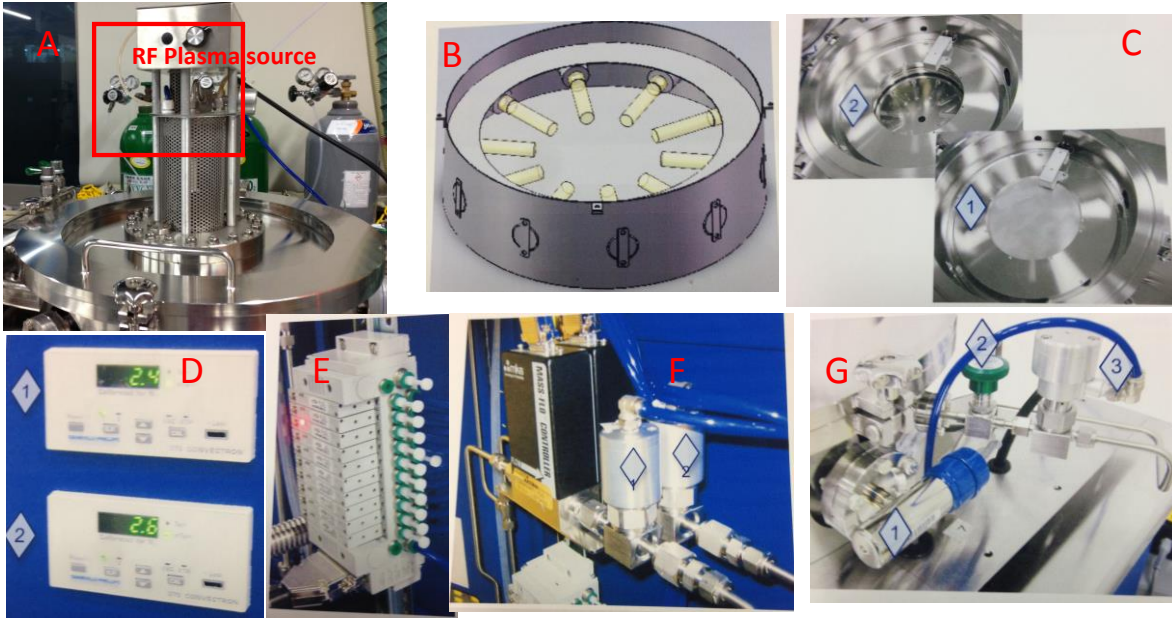


**Figure 3.5.** Experimental setup for ALD: Various components of SVTA ALD system. [Extracted From SVTA ALD Manual]

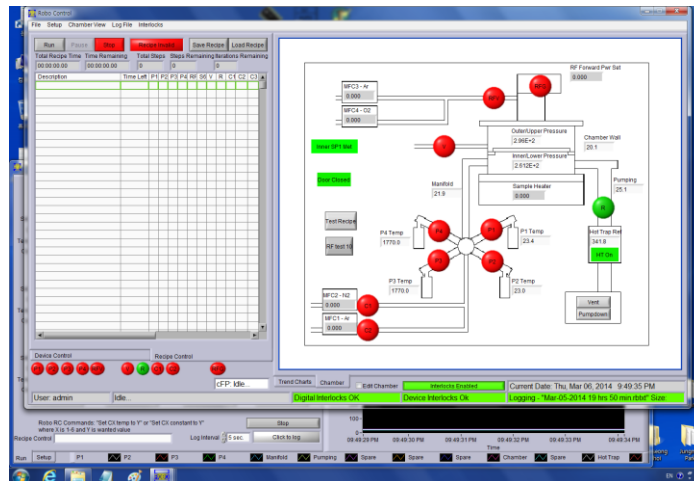


**Figure 3.6.** The picture of the RoboALD software main page. The RoboALD software is written in LabView language and ranges from complete manual operation of each component to full recipe automation.

The SVTA ALD system equipped with many components for ALD process. Out of which there are a few components are layout in Figure 3.5. This section is intended to give brief overview of the components displayed in the above Figure 3.5:

- (A) Growth chamber integrated with the R.F. Plasma source. The chamber includes convenient hand knobs for assuring reliable vacuum seal.
- (B) Sample heating lamps mounted on the bottom of the growth chamber, and are housed in a shield of Inconel that allows the substrate to be heated while keeping the surrounding cool.
- (C) Inner chamber lid: Removable lid provides flexibility to switch from thermal mode ALD processes to open chamber ALD processes using the RF Plasma source.
- (D) Gauge controllers placed on the front of the console door. Controllers provides convenient visual display of both inner (2) and outer (1) chamber pressure and provide communication to the ROBO software
- (E) Pneumatic distribution manifold provides air actuation to all pneumatic valves on the system.
- (F) Carrier gas flow meters is plumbed with two mass flow controllers. Either Argon (2) or Nitrogen (1) can be selected for carrier gas.
- (G) Chamber venting and pressure gauge: (1) Convenient pressure gauge has a range of 1 mTorr to 1000 Torr. (2) Manual flow control valve (2) for venting. (3) Pneumatic valve for Robo controlled venting.

### **Experimental procedures:**

In an ALD process, the precursors are loaded into different cylinders and then inserted to the ALD system. To deposit the target film, the substrate is placed in the ALD chamber and then created vacuum by using the pump down option in the Robo software. Also, assigned the temperature of the substrate, manifold, chamber wall and pumping by using Robo software. In this, Robo software is written in LabView language and ranges from complete manual operation of each component to full recipe automation. During ALD process, different precursors are supplied in an alternating manner for particular defined time set and also between the supplies of each precursor there is a purging step to clean out the byproducts and oversupplied precursors. In order to maintain a stable operation for high quality films with desired thickness, one needs to carefully keep an eye with the pressure curve which shows good repetition with time.

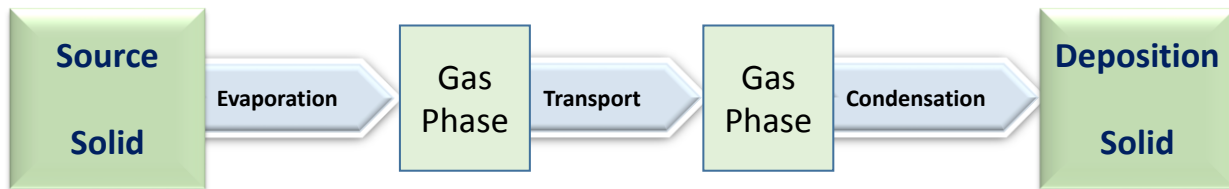


### 3.3. Physical vapor deposition

Physical vapor deposition (PVD) is a method to deposit thin films by vaporizing source materials and then condensing the vapor on the desired substrate. This process is purely physical and does not involve any chemical reactions. In general, PVD takes the following processing steps in order to get successful deposition.

- Evaporation
- Transport
- Condensation

The process can be summarized in the following flow chart.



PVD used in a variety of applications including fabrication of micro/nano electronic devices, optical and conductive coatings, surface modifications, diffusion barriers etc.

In this thesis, to fabricate the ZnO NW FET devices for electric and magnetotransport studies, thermal evaporation and electron beam evaporation techniques was utilized to deposit the electrode materials.

This section briefly introduce the thermal and electron beam evaporation laboratory setup and operation.

#### 3.3.1. Thermal Evaporation:

Thermal evaporation is the one of the PVD techniques, in which the source material is heated in a vacuum chamber until its surface atoms have acquired the sufficient energy to leave the surface. Once the source material is evaporated, the vacuum allows vapor particles to travel directly to the target substrate. Here, heat supplied to the source is through a resistive heating boat. The resistive heating boat used for the deposition of gold (Au) electrode was Tungsten. The typical current flows through the Tungsten boat in order to evaporate Au source to achieve deposition rate  $\sim 1 \text{ \AA/s}$  is  $\sim 55 \text{ A}$  in high vacuum condition.

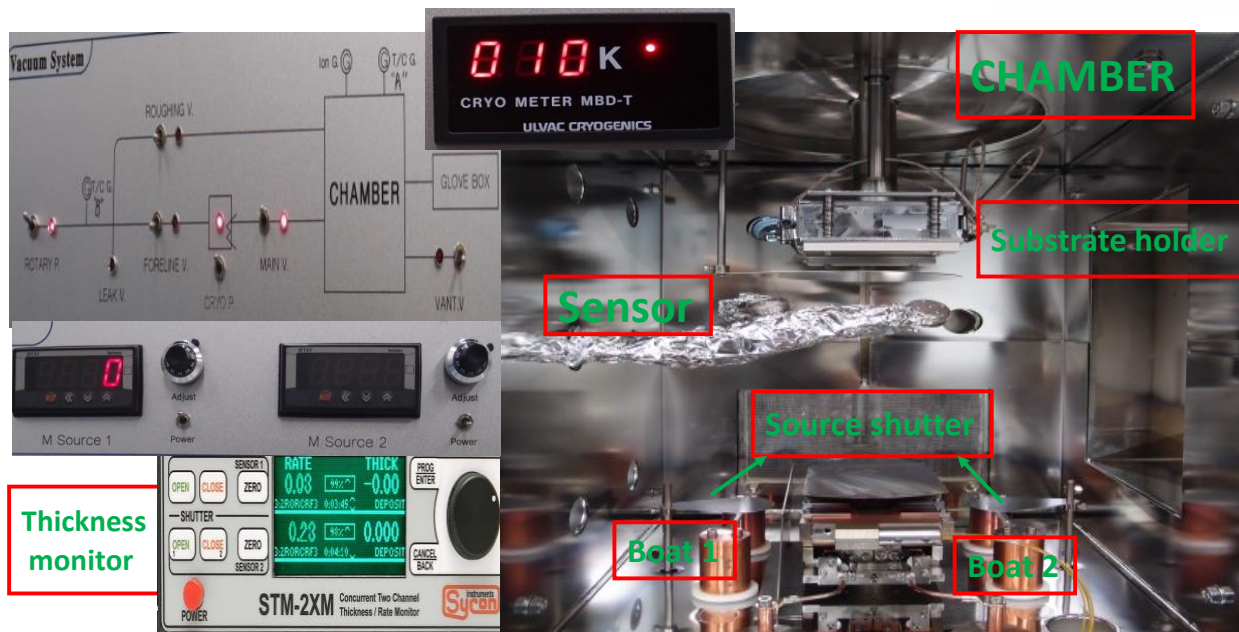


**Figure 3.7.** Experimental setup for thermal evaporation technique. Thermal evaporation technique was used to deposit the gold (Au) electrode to the ZnO NW during device processing.

**Advantages:**

- It is simple, robust and widespread in use and also cheaper heating arrangement
- Higher evaporation rate can be achieved at low cost and typical evaporation rate is 1-50 Å/sec
- High quality films could be obtained

**Drawbacks:**

- It is not easy to evaporate heavy metals due to insufficient temperatures
- There is a possibility of metallic boat can form an intermetallic alloy with the evaporate source
- There is a possibility of Expose substrates to visible and infrared radiation



### 3.3.2. Electron beam evaporation:

In this technique, the high energy electron beam is focused on the evaporant source. The electrons are emitted by a hot filament and then accelerated by a DC voltage source; a typical voltage source is 3 – 10 kV. The electron beam is focused on the evaporant source by a magnetic field arrangement, typically by bending beam through  $\sim 270^\circ$ . An additional lateral magnetic field is applied to produce x-y sweep. The evaporant sits on the water-cooled crucible. Multiple pocket rotary crucibles can be arranged to have sequential deposition of layers with a single pump down. The schematic illustration of electron beam evaporation working procedure is shown in above figure.

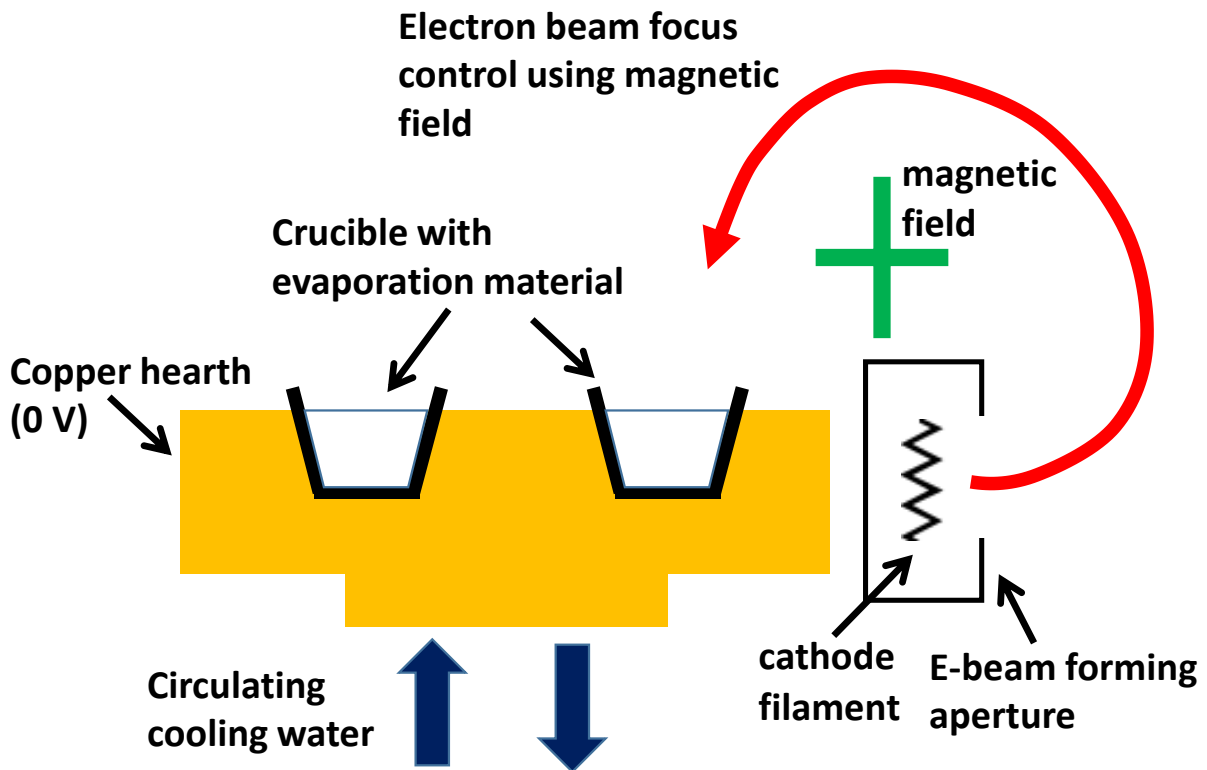
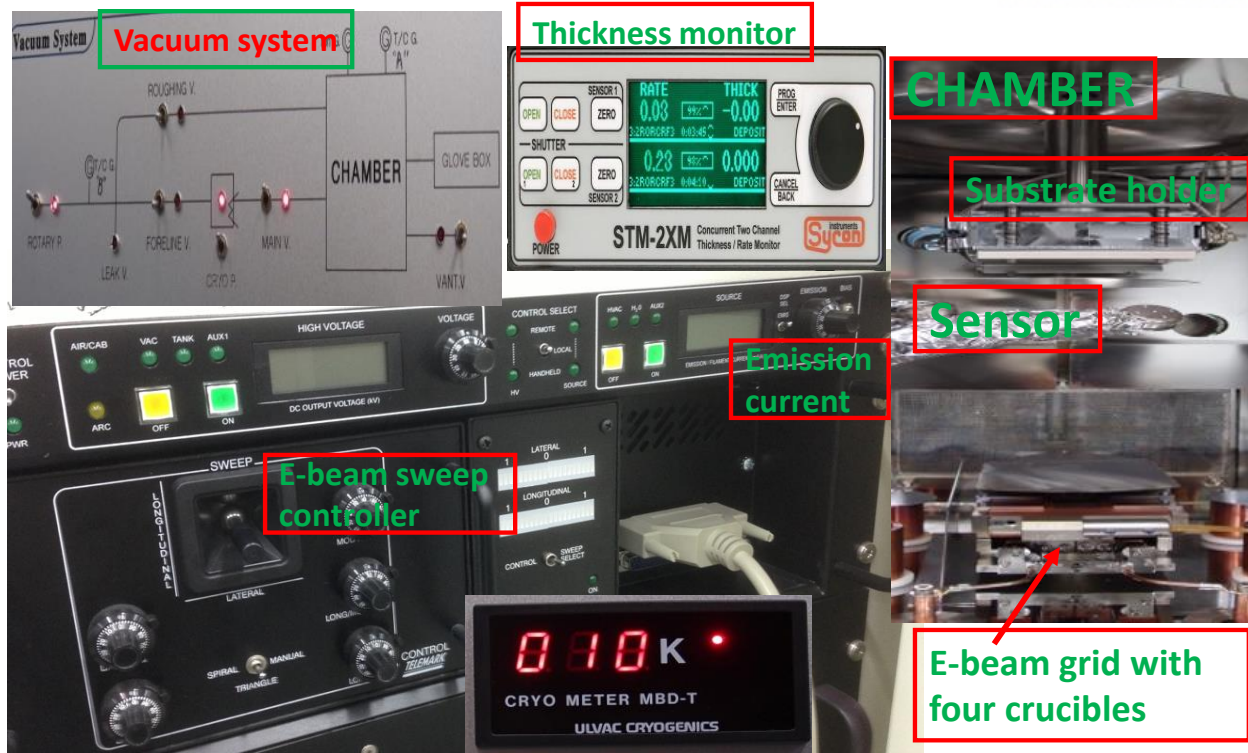


Figure 3.8. Schematic illustration of the electron beam evaporation technique



**Figure 3.9.** Experimental setup for electron beam evaporation technique. This technique was used to deposit various types of materials such as titanium (Ti), aluminum oxide ( $\text{Al}_2\text{O}_3$ ), iron (Fe), and cobalt (Co) during device fabrication process.

The advantages of this technique are as follows.

**Advantages:**

Extremely versatile and achieve higher temperatures greater than  $3000^\circ\text{C}$

Deposition rate precisely controllable and also typical high deposition rate 1-100  $\text{\AA}/\text{sec}$

Since the heating can be much localized, the highest temperature materials also can be evaporated

High quality film can be obtained

**Drawbacks:**

Complex systems are required

Expensive to maintain

Exposes substrates to secondary electron radiation

### 3.4. Electrical measurement setup

Electric and magnetic transport measurements were carried out using Quantum Design physical property measurement system (PPMS). PPMS includes the Even Cool dewar consists the liquid-helium bath in which the probe is immersed. The probe incorporates the superconducting magnet, sample chamber, power source, and the basic temperature control hardware. The picture of PPMS and electric measurement setup is shown in the above Figure 3.10 (a). The sample chamber consists of universal 12-pin platform that contacts the bottom of an installed sample puck. The installation of sample puck in the Ever cool chamber takes place with the help of sample puck holder. Figure 3.10 (b and c) shows the image of standard puck (sample holder) and rotatory puck. Ever cool serves as temperature, electric and magnetic field controller. In the ever cool chamber the high vacuum option allows to perform measurements in the high vacuum conditions. The chamber can be annealed up to 390 K and cooled down to 1.8 K in liquid helium environment. The magnetic field can be controlled up to  $\pm 9$  T.



**Figure 3.10. Electrical measurement setup.** (a) Physical property measurement system and electric measurement setup, where the measurement was taken by using Keithley electric instrument. (b) Standard sample puck and (c) rotator puck (for angle dependent measurements) for various magnetic field ( $-9$  T to  $+9$  T) and temperature dependent measurements.

The temperature of the sample is monitored by a temperature controller which was inbuilt in the PPMS chamber. The gate voltage controlled magneto transport properties of the ZnO NW FET device was characterized by using Keithley K2636A. The voltage was also read out using Keithley K2182 nano voltmeter. All electric measurements, PPMS options were together controlled by using Multivu and LabVIEW software installed in PPMS computer.

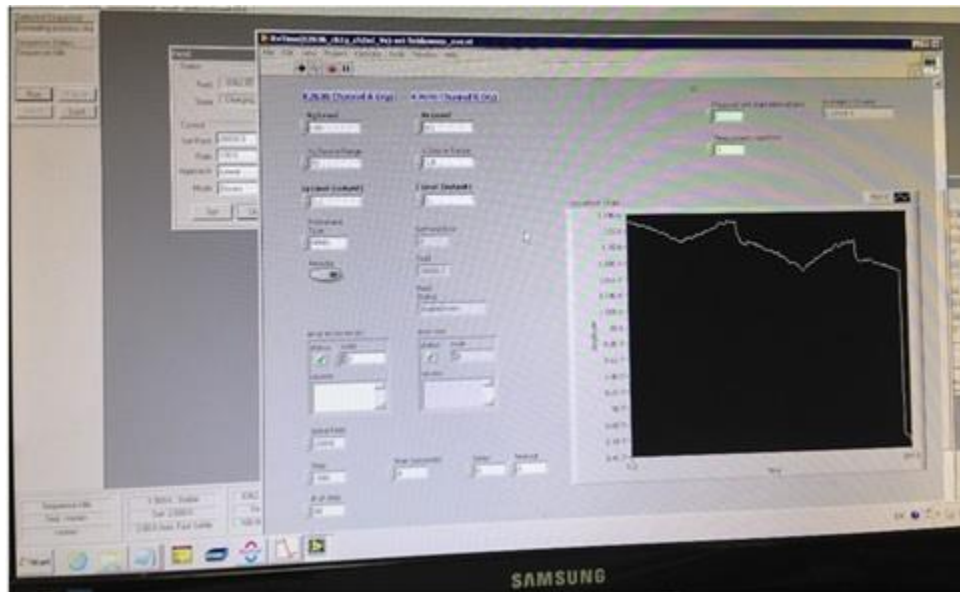


**Figure 3.11.** Installed LabVIEW software in a PPMS computer to control all electric measurements and PPMS options together with the help of Multivu software.

### 3.5. Physical property measurement system

Physical Property Measurement System (PPMS) is a versatile instrument consists of  $\pm 9$  T superconducting magnets in a Ever Cool helium dewar with the temperature range of 1.8-390K. PPMS offering several combinations of electrical measurements at various temperatures and magnetic fields.

- Magnetotransport measurements
- Conductivity, superconducting critical temperatures estimation
- Heat capacity and thermal transport options
- AC transport, Hall Effect measurements
- Rotating sample holder allows to rotate sample for  $360^\circ$  in the magnetic field range of  $\pm 9$  T and collect the set of angle dependent measurements for detailed analysis
- VSM option for the measurements of M-H hysteresis loop and Temperature dependent magnetization
- Also, the open software architecture allows for additional types of electrical measurements

#### Ever cool Helium Dewar

Basic setup of dewar consists the liquid-helium bath in which the probe is immersed. The probe incorporates the superconducting magnet, sample chamber, power source, and the basic temperature control hardware. The pump is connected to evacuate the sample chamber during measurements. The sample chamber incorporates an universal 12-pin platform and each of the experimental options uses its own specific insert. The PPMS is fully controlled by the user friendly and sophisticated Multivu software. Most of the experimental options can be operated in the temperature range 1.8 – 390 K with applied magnetic fields up to  $\pm 9$  T. The major components of the PPMS probe are shown in Figure 3.12.

In order to do electrical measurements, the sample is attached to a sample puck which has up to 12 electrical leads for performing I-V curves, DC/AC resistivity, Hall Effect, magnetotransport etc. Also the facility of horizontal rotator allows any of these measurements with 360-degree sample rotation under varying magnetic fields and temperatures.

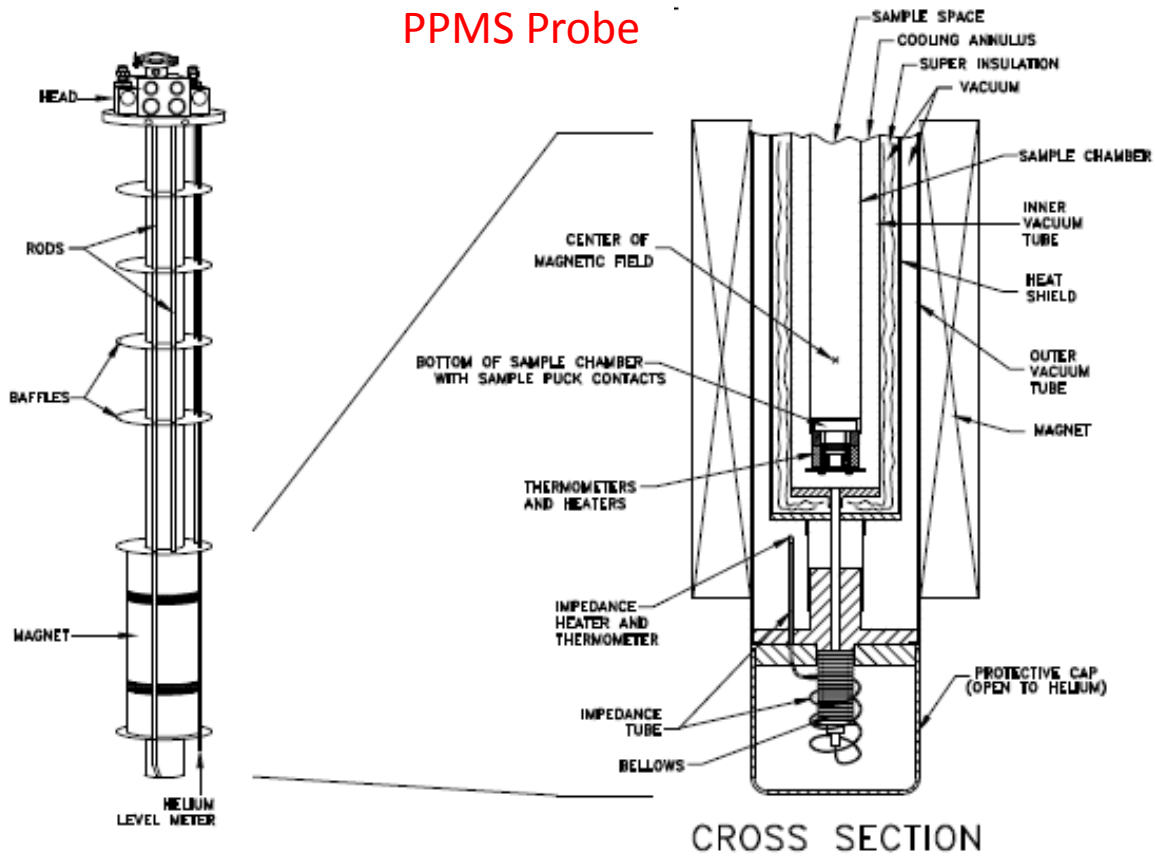
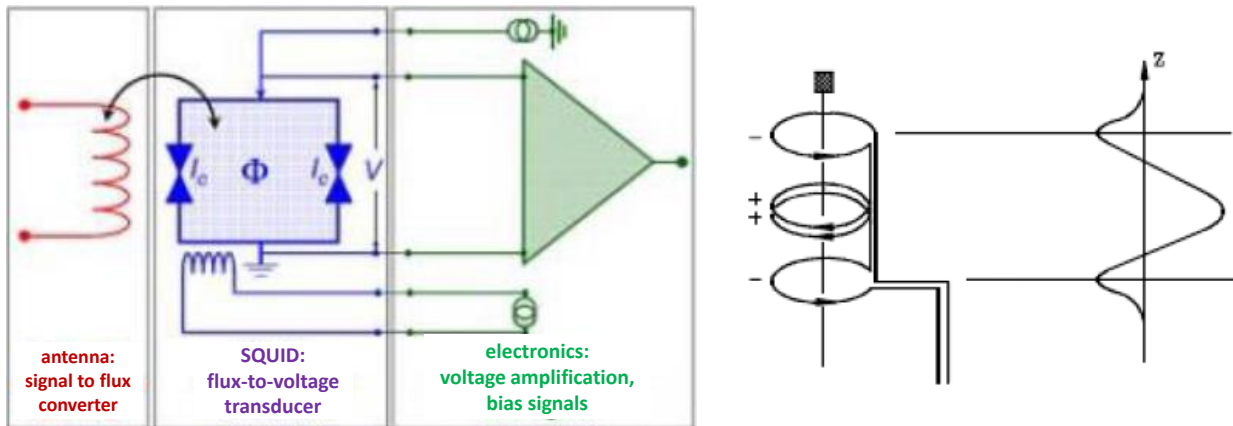


Figure 3.12. Major components of the PPMS probe [Extracted from Quantum design PPMS manual].



### 3.6. Magnetic property measurement system

The Magnetic property measurement system MPMS3 SQUID VSM is a versatile instrument which offers one of the most effective and sensitive ways of measuring magnetic properties. The MPMS3 commercial SQUID magnetometer can be considered as modification of the extraction method for the magnetization measurement. Advantage over the "classic" method comes from the use of superconducting material for the detection coils instead of the classical ohmic conductor. The detection coil consists of the loop of superconducting wire separated by two Josephson's junctions. When the sample is moved up and down it produces an alternating magnetic flux in the pickup coil. The magnetic signal of the sample is obtained via a Superconducting pick-up coil with 4 windings. The voltage between the two junctions is a periodic function of the magnetic flux inside the loop. Compared to the conventional magnetometers, the SQUID offers much higher sensitivity. In principle, signals corresponding to the magnetic flux quantum  $h/2e$  can be detected. The scheme of the magnetometer is in the Fig. 3.13 (left). Typical response curve, i.e. induced voltage as a function of the position of the sample with respect to the coil set is shown in the Fig. 3.13 (right). The sensitivity of the device is upto  $10^{-8}$  emu.



**Figure 3.13.** Scheme of the MPMS SQUID magnetometer (left), geometry of the detection coil and sample response curve (right) [From QD MPMS manual].

The operation of Magnetic property measurement system takes the following steps in order to measure the magnetic moment of a given sample.

(1) Sample mounting, (2) Sample loading (3) Centering sample (4) measure sample

Sample mounting:

This is very important step in order to extract the accurate measurement of the sample. For the accurate magnetic moment measurements, the magnetic signature of the sample holder should be measure before inserting the sample. The magnetic contribution of the sample holder should subtract from the total magnetic signal in order to estimate the accurate magnetic moment of a give sample.

Sample loading:

In this step, the sample holder with mounted sample need to attach to the sample rod before loading into the MPMS chamber. During the attachment, the sample holder should be handle carefully to avoid contamination from the hands.

Centering Sample:

This step is very important for the accurate measurements. In this step, for the accurate measurements, the sample must be centered within the detection coils. Specify the sample offset so that it may be properly centered during measurements.

Measure sample:

- Choose the type of measurement, such as Moment Vs Field or Moment Vs Temperature.
- Write the sequence, to automate the magnetic field, temperature and data collection.



## Chapter 4

# ZnO nanowires: Growth and characterization

---

### 4.1. Introduction

#### ZnO and its applications

ZnO is a wide-band-gap semiconductor with a direct gap of  $E_G \sim 3.3$  eV at room temperature. It preferentially crystallizes in the hexagonal wurtzite-type structure (see figure 4.1) which is the stable phase of ZnO at room temperature. Along the hexagonal c-axis, adjacent polar lattice planes of zinc and oxygen are found. Every oxygen atom is surrounded tetrahedrally by four zinc atoms and vice versa. Zinc-blende and rock-salt phases also exist, but these phases are only stable under high pressure. The bonding between adjacent atoms of zinc oxide is found to be covalent, but with a partial ionic bonding component. Due to the partially ionic bonding and the lack of an inversion center, ZnO is a piezoelectric material.<sup>93</sup>

ZnO involves promising applications in the fabrication of transparent electronics,<sup>94</sup> spintronics,<sup>95</sup> photonics, shorter wavelength optoelectronics,<sup>96</sup> Photovoltaic<sup>97</sup> and sensors.<sup>98</sup> Compared to the GaN ( $\sim 25$  meV), ZnO has higher exciton binding energy,  $\sim 60$  meV, and fascinates it with higher light emission efficiency for brighter UV/ blue lasers and LEDs. Although the room temperature electron Hall mobility of single crystal ZnO has slightly lower ( $\sim 200$  cm<sup>2</sup>/V) than that of the GaN, it exhibits higher saturation velocity. Also, ZnO exhibits higher radiation resistive than that of the GaN, therefore might have possible applications in space and nuclear. The easier achievable growth on cheap substrates such as glass and plastic, makes ZnO as special candidate to fabricate low-cost devices. ZnO is also considered to be a much needed DMS material in spintronic research due to its Curie temperature well above the room temperature (RT). Also ZnO serves as the best host material for doping with transition metals, noble metals, and rare earth metals.

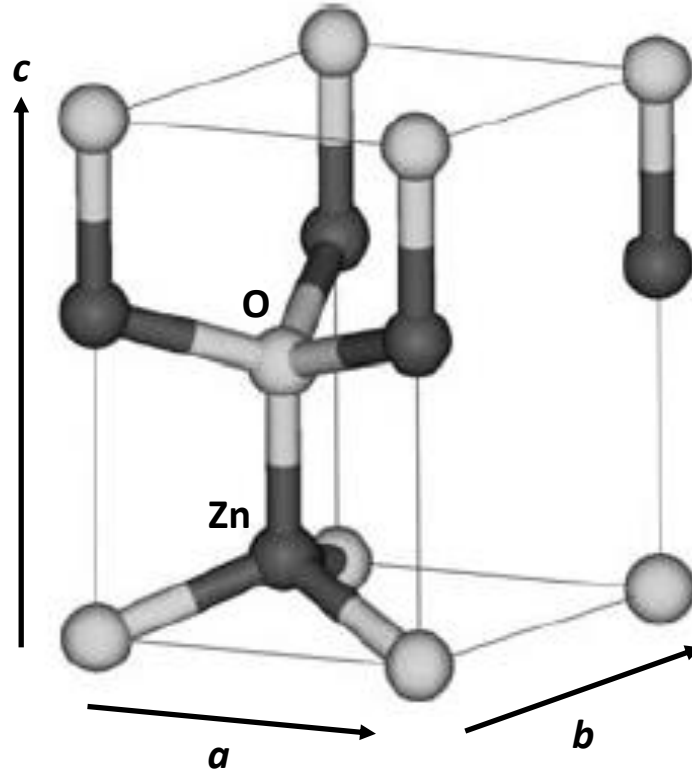


**Figure 4.1.** Schematic view of the primitive unit cell of the wurtzite type ZnO crystal structure. The light grey spheres corresponds to oxygen, whereas dark spheres corresponds to zinc. The base plane primitive translation vectors  $a$  and  $b$  include an angle of  $120^\circ$  and  $c$  is orthogonal to them.<sup>93</sup>

## Synthesis of ZnO nanostructures: Different Methods

A wide variety of methods are available to synthesize ZnO nanostructures. In general, these methods can be divided into two categories: vapor-phase growth and solution-phase growth. Figure 4.2 represents the various growth methods for synthesis of ZnO nanostructures.<sup>99</sup>

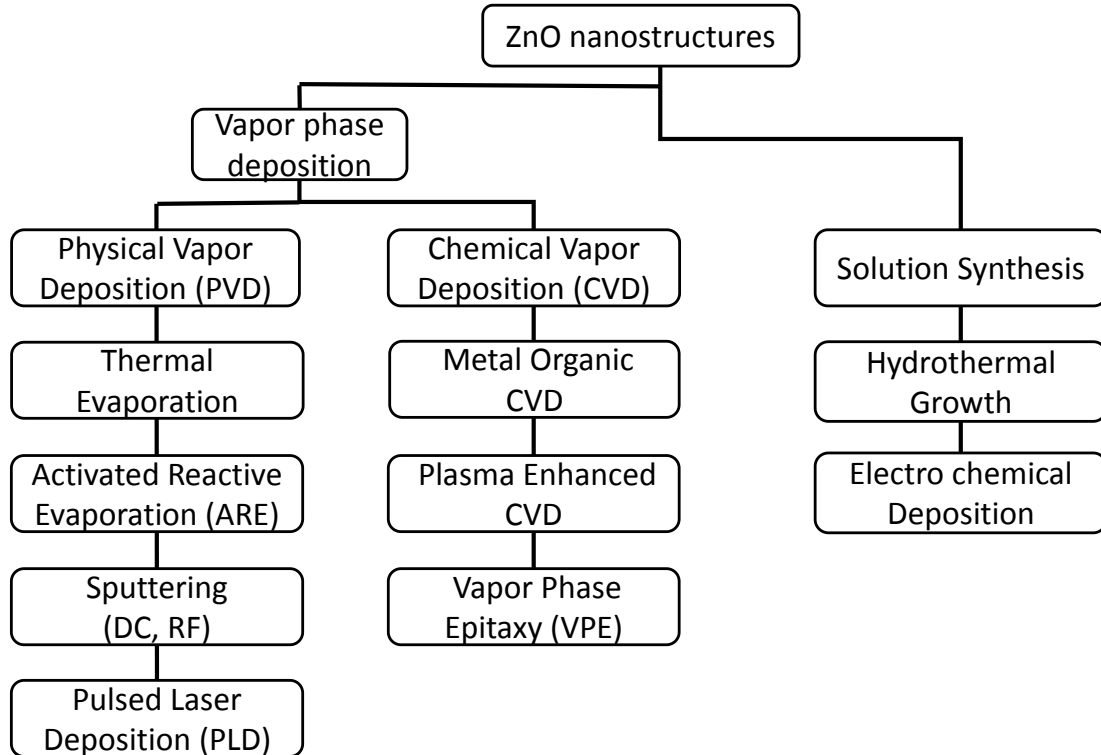


**Figure 4.2.** Schematic chart representing various methods employed in the growth of ZnO nanostructures

In the following sections, the growth and characterization of ZnO nanowires utilized in the framework of this thesis is presented.

## 4.2. Experiment: Synthesis of ZnO nanowires using CVD method

ZnO NWs used in our devices were synthesized by chemical vapor deposition (CVD) technique on a sapphire substrate<sup>100</sup>. A 3-nm-thick Au film was initially deposited on the substrate, followed by rapid annealing at 300°C for 1 min in ambient nitrogen. As is well known, Au film aggregates into well-separated Au nanoparticles, which can enhance the growth of the NWs. An alumina boat with pure Zn and ZnO powders (99.9%, Alfa Aesar) was introduced into a quartz tube furnace and the sapphire substrate with Au nanoparticles was placed downstream of the boat. The tube was initially evacuated to 10 mtorr. Then, Ar gas (100 sccm) containing traces of oxygen was introduced into the tube. The furnace temperature was increased to approximately 900 °C and maintained at this temperature for 1 h for the growth. After the reaction, the furnace was cooled to room temperature by flowing Ar. The schematic illustration of the growth mechanism of ZnO NWs using CVD technique is shown in Figure 4.3.

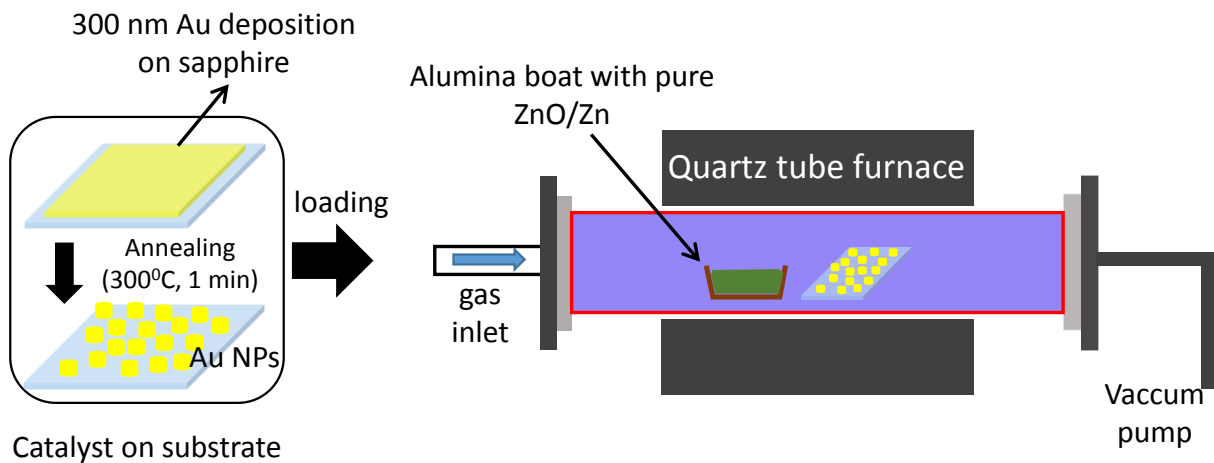


**Figure 4.3.** Schematic illustration of the growth mechanism of ZnO nanowires using CVD method

The Scanning electron microscopy (SEM) image of ZnO NWs on sapphire substrate grown by CVD method is shown in the above figure.

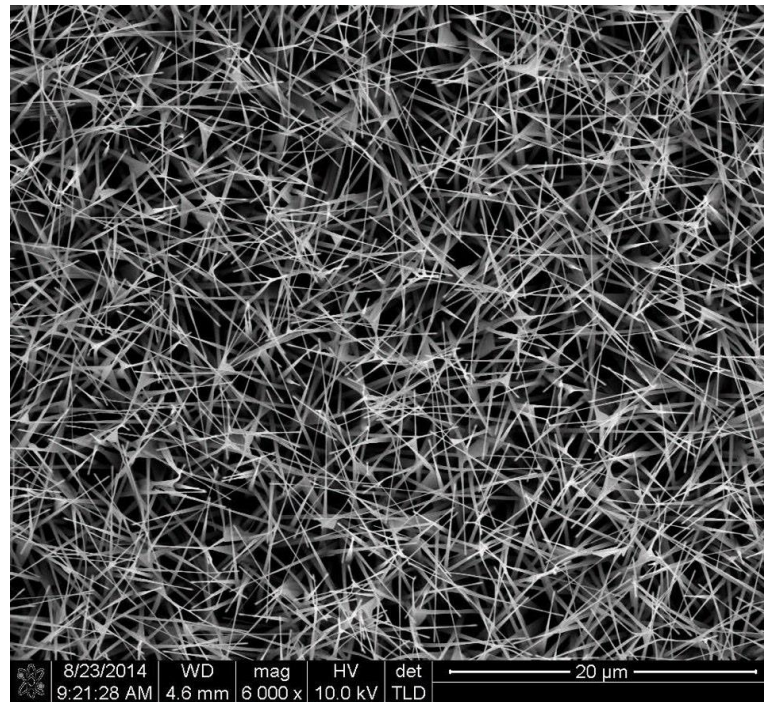


**Figure 4.4.** Scanning electron microscopy (SEM) image of an assembly of ZnO NWs grown by CVD method.

### 4.3. Characterization of ZnO nanowires

#### 4.3.1. Results and Discussion: XRD and HR-TEM analysis

To confirm the crystal structure and composition of CVD-grown ZnO NWs, we characterized our samples by using X-ray diffraction (XRD), high-resolution transmission electron microscopy (HRTEM), and X-ray photoelectron spectroscopy (XPS). The XRD pattern of the ZnO NWs grown on the sapphire substrate is displayed in Figure 4.5. According to the X-ray results, our CVD-grown ZnO NW formed a hexagonal wurtzite structure. Figure 4.6 shows the HRTEM image of our ZnO NW sample and the inset displays the corresponding selected area electron diffraction (SAED) pattern. Both the HRTEM image and SAED pattern clearly confirm uniform growth of the ZnO NW along the c-axis of the hexagonal wurtzite structure.

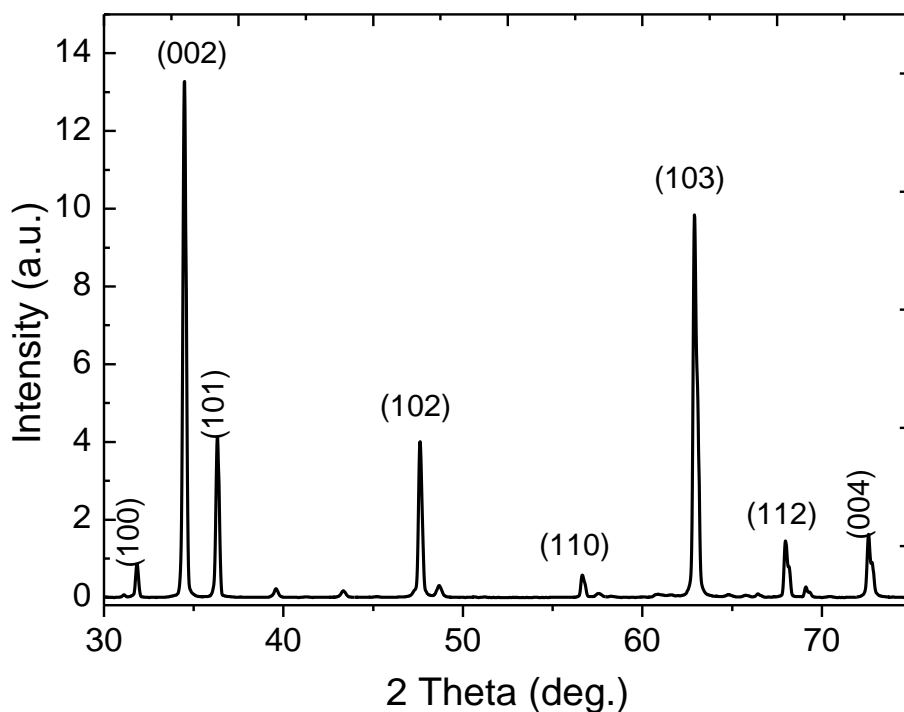


**Figure 4.5. Structural characteristics of ZnO NWs grown by the CVD method.** (a) XRD pattern of as-grown ZnO NWs grown on a sapphire substrate by CVD method.

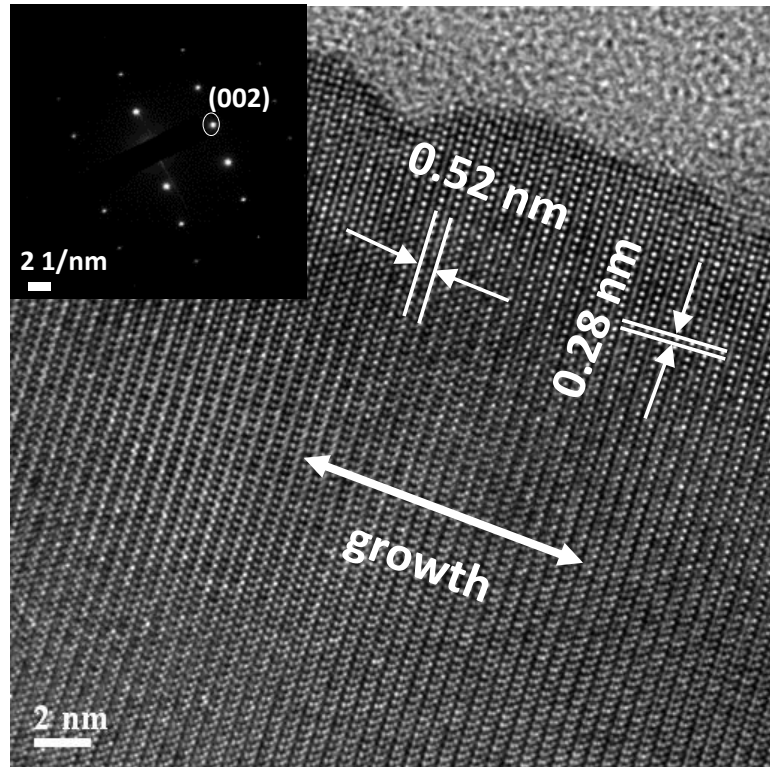


**Figure 4.6.** HR-TEM image of ZnO NW shows growth in the c-axis direction of the hexagonal wurtzite phase. Inset shows the corresponding SAED pattern.

4.3.2. Results and Discussion: XPS analysis

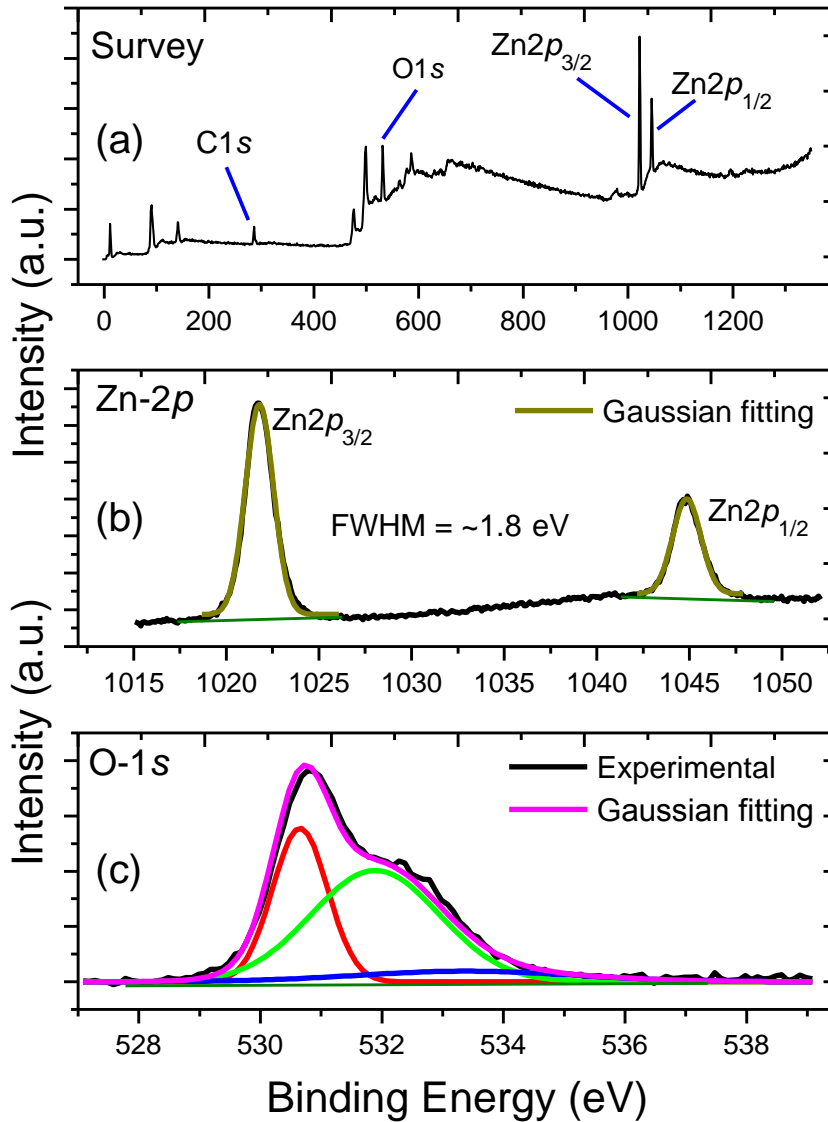


**Figure 4.7. Elemental characteristics of ZnO NWs grown on the sapphire substrate.** (a) Survey XPS spectrum of ZnO NWs on the sapphire substrate. (b-c) Magnified views on the XPS spectrum corresponding to the Zn-2*p* (b) and O-1*s* (c) core level regions.



Figure 4.7 displays XPS results for the assembly of as-grown ZnO NWs. XPS was performed to investigate whether impurities and other undesirable chemical residues had formed on the sample during the synthesis. The XPS survey of the as-grown ZnO NWs shown in Figure 4.7(a) indicated the presence of Zn, O, and adventitious C, but no other contaminants in our sample.<sup>101</sup> An XPS spectrum of the ZnO NWs (Figure 4.7(b)) displayed two peaks, corresponding to Zn-2*p*<sub>3/2</sub> and Zn-2*p*<sub>1/2</sub>. These peaks were observed to be approximately symmetric and centered at ~1021.7 and ~1044.8 eV, indicative of Zn<sup>2+</sup> in ZnO.<sup>102</sup> The linewidths (FWHM) of these peaks were measured to be about 1.8 eV. Both the positions and linewidths of these peaks are consistent with the pure ZnO NW phase.<sup>101</sup> Figure 4.7(c) displays the XPS spectra of the O-1*s* core level region in our sample. To gain insight into the oxygen vacancies in the ZnO NWs, the O-1*s* core level spectrum was deconvoluted into multiple Gaussians. These peaks were observed to be located at about 530.6 eV, 531.8 eV, and 533.4 eV, respectively. The highest binding energy peak at 533.4 eV is generally attributed to chemisorbed oxygen on the ZnO NW surface (blue curve). The lowest binding energy (530.6 eV) component is associated with the O<sup>2-</sup> ions in hexagonal wurtzite ZnO phase (red curve). The medium binding energy (531.8 eV) component arose from O<sup>2-</sup> in the oxygen-deficient regions of the ZnO matrix<sup>102, 103</sup> (green curve). Therefore, the XPS analysis clearly showed that our as-grown ZnO NWs accommodated noticeable amounts of oxygen vacancies, but no transition metal contamination. Therefore, the observed ferromagnetism in our studied ZnO NW assembly may be confidently associated with the spin host from oxygen vacancies in the matrix of the ZnO wurtzite phase.

## 4.4. Ferromagnetism in ZnO NWs

### 4.4.1. Introduction

There is current interest in the development of dilute magnetic semiconductors (DMS) exhibiting ferromagnetic behavior for spin-based transistors, light emitting diodes, and sensors. Among the various DMSs, ZnO is a promising spin source since it epitomizes DMS with  $T_c$  well above room temperature (RT). Dietl et al. prediction of critical temperatures for various semiconductors are shown in Figure 4.8.<sup>104</sup> In particular, magnetization of ZnO can be induced by either transition ion doping and/or by intrinsic defects, such as oxygen vacancy ( $V_O$ ) and zinc vacancy ( $V_{Zn}$ ). In particular,  $V_O$ -induced RT ferromagnetism in as-grown ZnO nanowires (NWs) has been well established.<sup>46, 50</sup> The  $V_O$ -induced emissions in the photoluminescence (PL) spectra in as-grown ZnO NW are always concomitant with the presence of ferromagnetism<sup>46-50</sup>. The presence of  $V_O$  defects as well as ferromagnetism in ZnO can be eliminated by annealing the ZnO in an oxygen environment, and these features can be even resurrected by vacuum annealing<sup>48, 51</sup>. It has been shown that formation of  $V_O$  energetically attracts interstitial Zn ( $I_{Zn}$ )<sup>52</sup>. While the former presents as a deep level trap, the latter forms a shallow donor level. Thus, the pair creation of defects causes ZnO to be a primarily  $n$ -type semiconductor<sup>52</sup>. An electron spin resonance (ESR) study showed that singly charged deep levels from  $V_O$  can host unpaired electron spins<sup>53</sup>.

In this section, we show the magnetic property of our CVD grown ZnO nanowires utilized in the context of this thesis is presented.

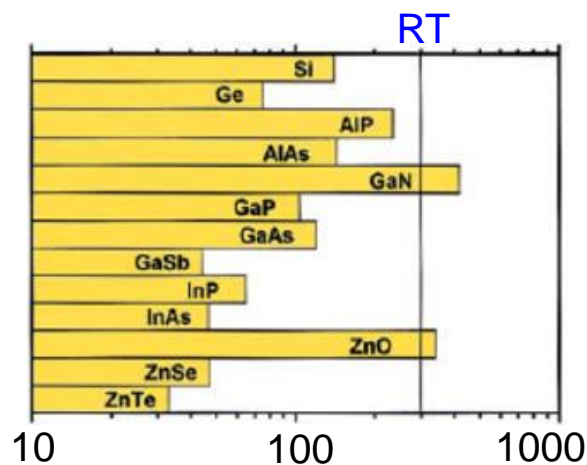
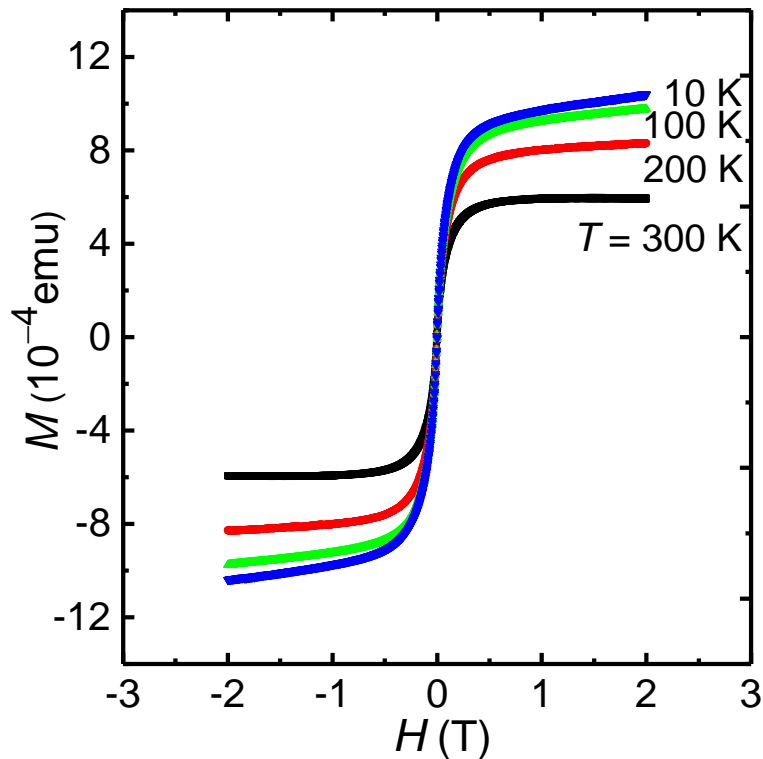


**Figure 4.8.** Dietl et al. predicted of critical temperatures for various Mn-doped  $p$ -type semiconductors (diluted magnetic semiconductors).<sup>104</sup>

#### 4.4.2. Results and Discussion

##### SQUID measurement

ZnO NWs used in our study were synthesized by chemical vapor deposition on a sapphire substrate. Figure 4.9 displays the  $M$ - $H$  hysteresis loops for an assembly of ZnO NWs grown on a sapphire substrate. The measurements were taken at  $T = 300$  K, 200 K, 100 K, and 10 K using a Quantum Design superconducting quantum interference device (SQUID). The diamagnetic contribution from the sapphire substrate was carefully subtracted. Robust ferromagnetic moment with small coercivity ( $\sim 10$  Oe) can be well observed at 300 K.



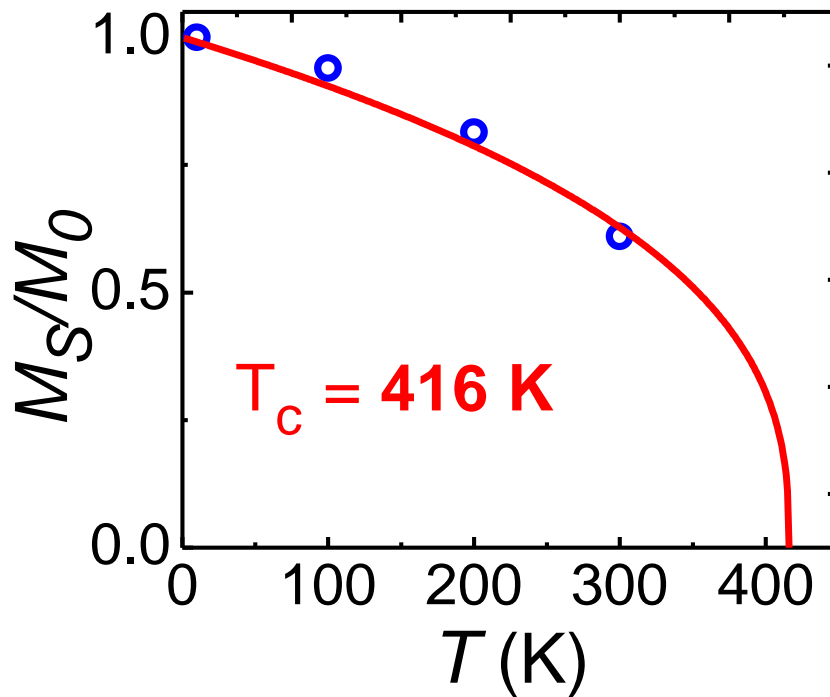
**Figure 4.9.** Magnetization as a function of magnetic field measured at  $T = 300$ , 200, 100 and 10 K for an assembly of ZnO NWs.

Figure 4.10 displays the temperature dependence of the saturation magnetization, which was fitted to the power-law

$$M_s(T)/M_0 = (1 - T/T_c)^\beta$$

The obtained  $\beta$  was 0.365, which corresponds to the 3D Heisenberg model.<sup>105</sup> The critical temperature  $T_c$  was estimated to be 416 K, significantly higher than room temperature (RT). Here,

$$M_0 = M_s(T = 0) \approx M_s(T = 10\text{K})$$



**Figure 4.10.** Normalized saturation magnetization ( $M_s/M_0$ ) as a function of temperature. The estimated Curie temperature to be well above room temperature (approximately 416 K)

## 4.5. Conclusions

In conclusion, we discussed the growth and characterization of ZnO NWs grown by chemical vapor deposition (CVD) technique. The crystal structure and composition of ZnO NWs were studied by X-ray diffraction (XRD), high-resolution transmission electron microscopy (HRTEM), and X-ray photoelectron spectroscopy (XPS). According to the X-ray results, our CVD-grown ZnO NW formed a hexagonal wurtzite structure. Furthermore the HRTEM image and SAED pattern clearly confirm uniform growth of the ZnO NW along the c-axis of the hexagonal wurtzite structure.

We also studied the magnetic properties of as grown ZnO NWs grown by CVD method. The magnetic property was observed from 300K to 10K by using super conducting quantum interface device (SQUID). The ferromagnetism in our ZnO NWs was observed well above the room temperature.

## Chapter 5

# ZnO nanowire field effect transistor

---

### 5.1. Introduction

The "transistor" or "transfer-resistor" is a semiconductor device used to control the resistance between two terminals by using a third terminal. In a bipolar transistor, the current between collector and emitter can be controlled by the much smaller current at the base (third) terminal. The first realization of a bipolar transistor was pioneered by Bardeen, Brattain, and Shockley in 1947.<sup>106, 107</sup>

A different approach to realize transistor was first patented by Julius Edgar Lilienfeld in 1925.<sup>108</sup> In a field effect transistor, the current flow between two terminals (source and drain) is controlled by the electric field from the third terminal (gate). In contrast to the bipolar transistor, the third terminal is capacitively coupled and is not in direct contact with the semiconductor. The schematic view of a typical Al<sub>2</sub>O<sub>3</sub>-capped ZnO NW device is shown in Figure 5.1(a).

### Transport parameters

Using  $I_d$  vs  $V_g$  curve (Figure 5.3), the field-effect mobility can be estimated by

$$\mu = \frac{dI_d}{dV_g} \times \frac{L^2}{V_{ds} \times C_{ox}} \quad (5.1)$$

where,  $g_m = dI_d/dV_g$  is the transconductance,  $V_{ds}$  is the source-drain voltage.  $C_{ox}$  is the gate capacitance and defined as,

$$C_{ox} = \frac{2\pi\epsilon_{ox}\epsilon_0 L}{\ln\left(4t_{ox}/d\right)} \quad (5.2)$$

where  $\epsilon_0 = 8.85 \times 10^{-14}$  F/cm is the vacuum permittivity,  $d = 120$  nm is the diameter of the ZnO NW, and  $t_{ox} = 300$  nm is the thickness of the back-gated dielectric.

Using Drude model, the carrier concentration ( $n$ ) can be estimated as,

$$n = 1/\rho q\mu \quad (5.3)$$

where  $\rho$  is the resistivity of the NW,  $q$  is the charge of the electron.

The resistivity  $\rho$  can be further estimated as,

$$\rho = R \frac{A}{L} \quad (5.4)$$

where  $R$  is the resistance of the NW,  $A$  is the area of cross section of the NW, and  $L$  is the channel length.

Then, the  $k_{Fl}$  values were estimated from the free electron model according to

$$k_{Fl} = \frac{\hbar(3\pi^2)^{2/3}}{e^2\rho n^{1/3}} \quad (5.5)$$

## 5.2. Experiment: Device fabrication

To fabricate the device, the as-grown ZnO NWs were sonicated and suspended in IPA solution, which were transferred to a SiO<sub>2</sub> (300 nm)/*p*-Si substrate. The transferred NWs on SiO<sub>2</sub>/Si substrate were inspected by using optical microscope and identified the NW for device fabrication. Electron beam lithography was used to define multiple electrodes on the NW. Before the electrode (Ti (10 nm)/Au (120 nm)) deposition, argon plasma etching was performed to improve contact resistance between Ti/Au and the ZnO NW.<sup>109</sup> After performing a lift-off process in acetone, samples were transferred into an atomic layer deposition chamber and were annealed for 4 hours prior to the deposition of the 15 nm-thick Al<sub>2</sub>O<sub>3</sub> capping layers. Post annealing was then done for 3 hours. The substrate temperature was maintained at 120 °C throughout the annealing and Al<sub>2</sub>O<sub>3</sub> deposition process. Note that these low-temperature annealing procedures also assist in the formation of Ohmic contacts between Ti/Au and the ZnO NW.<sup>110</sup> The schematic view of a typical Al<sub>2</sub>O<sub>3</sub>-capped ZnO NW device is shown in 5.1(a). Figure 5.1(b) shows the corresponding SEM image of a ZnO NW FET device with multiple electrodes.

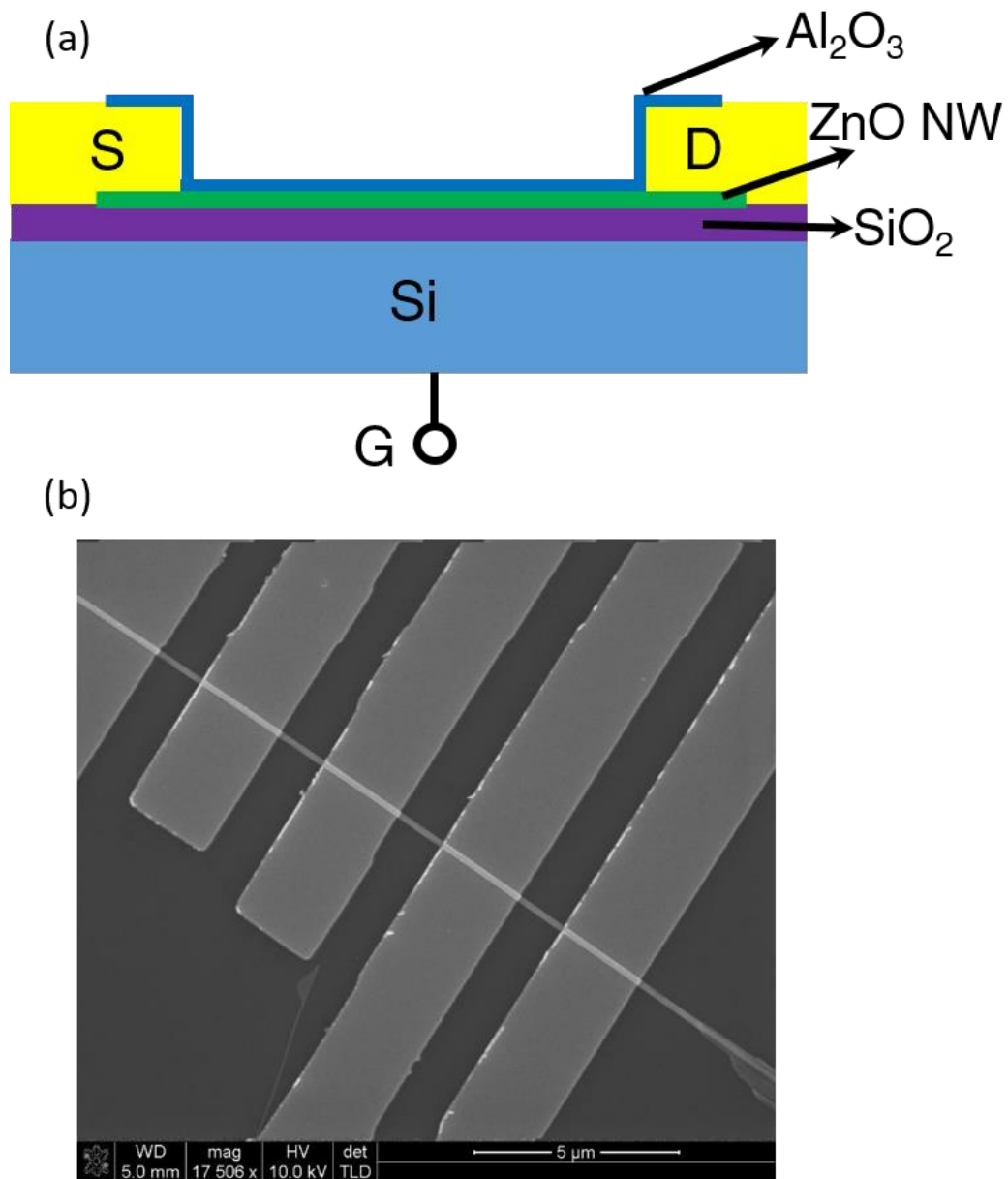
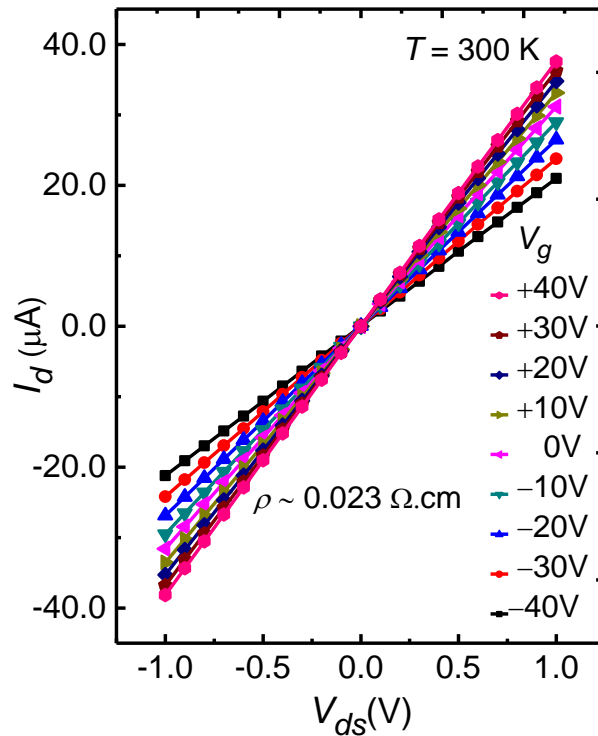


**Figure 5.1.** (a) Schematic illustration of a typical  $\text{Al}_2\text{O}_3$ -capped ZnO NW FET device and (b) its corresponding SEM image with multiple electrodes. Here, the effective channel length was  $L = 1.5 \mu\text{m}$ .



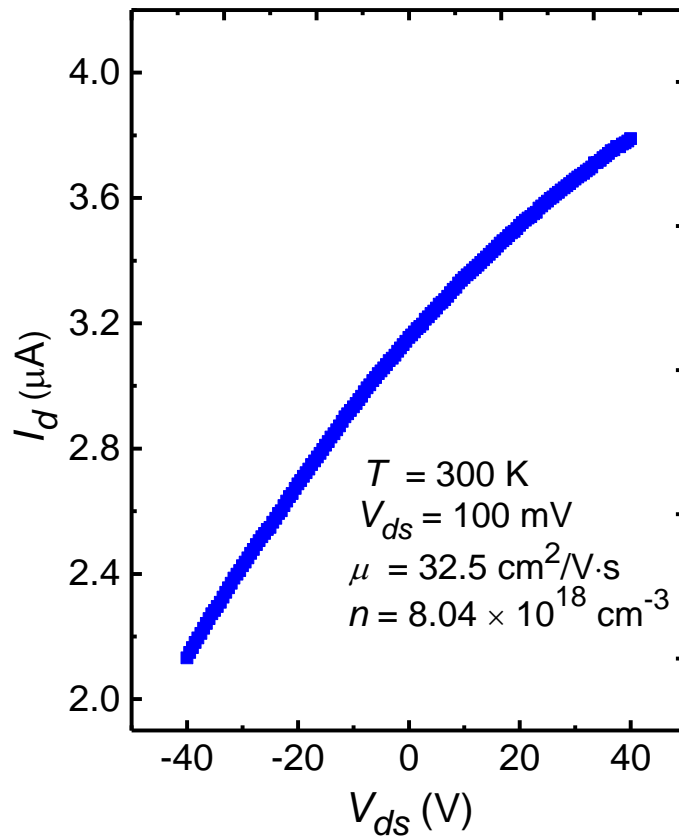
### 5.3. Results and Discussion

Transport properties of all our devices were characterized by using a Quantum Design physical property measurement system (PPMS). Figure 5.2 shows the  $I_d - V_{ds}$  characteristics at various gate voltages at room temperature. The linear  $I-V$  curves confirm the excellent Ohmic contact between our ZnO NW and the Ti/Au electrode. Therefore, we can effectively avoid other effects from field-dependent impurity scattering at the interface when we characterize the MR of a two-terminal FET discussed in the following chapter. The resistivity of the ZnO NW was estimated to be  $\rho \sim 0.023 \Omega \cdot \text{cm}$  at  $V_g = 0 \text{ V}$ .



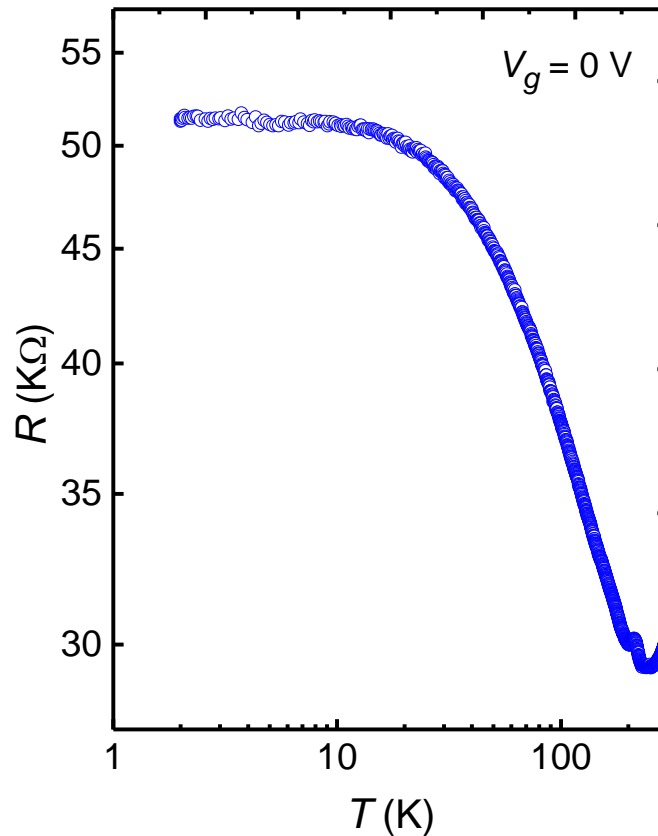
**Figure 5.2.**  $I-V$  characteristics of the studied ZnO NW at  $T = 300 \text{ K}$ . The extracted resistivity was determined to be  $\rho \sim 0.023 \Omega \cdot \text{cm}$  at  $V_g = 0 \text{ V}$ .

Figure 5.3 shows the FET characteristics of the ZnO NW at room temperature, which exhibits the majority carriers are  $n$ -type. This device characteristic indicates  $V_O$  rather than  $V_{Zn}$  is the main source for the native doping in our studied sample. The field-effect electron mobility ( $\mu$ ) and carrier concentration ( $n$ ) extracted from the FET curve were estimated to be  $\sim 32.5 \text{ cm}^2/\text{V}\cdot\text{s}$  and  $\sim 8.04 \times 10^{18} \text{ cm}^{-3}$  by using the equations shown in the above section. Here, the effective channel length and diameter of the ZnO NW was  $L = 1.5 \text{ }\mu\text{m}$  and  $d = 120 \text{ nm}$ .



**Figure 5.3.** The corresponding  $V_g$ - $I_d$  characteristics at  $V_{ds} = 100 \text{ mV}$ . The obtained field-effect mobility was  $\mu = 32.5 \text{ cm}^2/(\text{V}\cdot\text{s})$ , and the carrier density was  $n = 8.04 \times 10^{18} \text{ cm}^{-3}$ .

Figure 5.4 shows the temperature dependence of the resistance of the ZnO NW device at  $V_g = 0$  V. When the temperature was decreased below 250 K, the resistance of the device increased, indicating that the studied NW follows semiconductor behavior. But the change of resistance with temperature was not large, which reveals that this NW was natively doped and lies near the metal-insulator transition region.<sup>56, 57</sup> Above 250 K, the device resistance displays anomalous increase. This behavior could be also understood if the native doping concentration of our studied batch of sample is at the crossover of the metal-insulator transition. Then, the ZnO NW can behave like metal at high enough temperature because nearly all the electrons at the shallow donor levels are activated. However, as temperature decreases, activation energy plays more important role for the device resistance. As discussed in the chapter 7, the shallow donor levels in the ZnO typically lie at  $\sim$  tenths of meV below the conduction band edge. This energy scale and the temperature of the turning point for the device resistance are qualitatively consistent together.



**Figure 5.4.** Temperature dependent transport of ZnO NW device at  $V_g = 0$  V.

### Estimation of gate dependent $k_{Fl}$ value at $T = 2\text{ K}$

Figure 5.5(a) displays the transport characteristics of the ZnO NW FET device at 2K. Using Eqn 5.1, the estimated mobility ( $\mu$ ) at  $V_g = 0\text{ V}$  was  $21.49\text{ cm}^2/\text{V}\cdot\text{s}$ .

The carrier density ( $n$ ) at  $V_g = 0\text{ V}$  based on the Drude model can be obtained from

$$\sigma = ne\mu \Rightarrow n = \frac{\sigma_0}{e\mu} \approx 7.54 \times 10^{18}\text{ cm}^{-3} \quad (5.6)$$

where  $\sigma_0$  is conductivity at  $V_g = 0\text{ V}$ . Using  $n$  (at  $V_g = 0\text{ V}$ ) as the reference value, we estimated the carrier density (left axis of Figure) in the channel region for various gate voltages from  $V_g = -40\text{ V}$  to  $V_g = +40\text{ V}$ .

The  $k_{Fl}$  values were estimated from the free electron model according to Eqn 5.5. As shown Figure 5.5(b), the calculated  $k_{Fl}$  values (right axis) were found to be less than unity, indicating the studied ZnO NW system to be in the strongly localized regime.

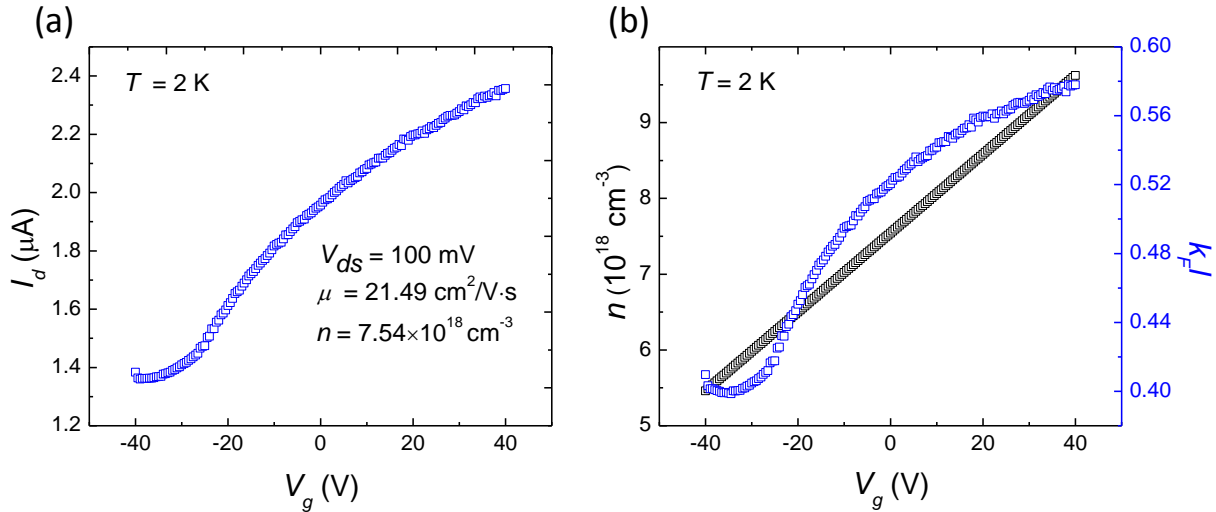


**Figure 5.5. FET behavior and transport parameters at  $T = 2\text{ K}$ .** (a)  $V_g$ - $I_d$  curve of ZnO NW FET device at  $V_{ds} = 100\text{ mV}$ . At  $V_g = 0\text{ V}$ , the carrier density was estimated to be  $n = 7.54 \times 10^{18}\text{ cm}^{-3}$  and the mobility to be  $= 21.49\text{ cm}^2/\text{V}\cdot\text{s}$ . (b) The carrier density  $n$  (left axis) and the corresponding  $k_{Fl}$  value (right axis) as a function of  $V_g$ .

## 5.4. Conclusions

In conclusion, we fabricate and characterized the ZnO nanowire FET devices. The measurements at room temperature shows that good ohmic contact between Ti/Au and ZnO NW. The mobility was estimated to be  $\sim 32.5 \text{ cm}^2/\text{V} \cdot \text{s}$  at 300 K. The temperature dependent resistance measurement and carrier concentration at  $V_g = 0 \text{ V}$  reveal that the studied ZnO NWs were natively doped and lies at the crossover of the metal-insulator transition. Furthermore, we estimated the  $k_{Fl}$  value less than unity, which indicates that the NWs used for our study are in the strongly localized regime ( $k_{Fl} < 1$ ).

## Chapter 6

# Gate-tunable magnetotransport in ferromagnetic ZnO nanowire FET devices

---

### 6.1. Gate-tunable spin exchange interactions and magnetoresistance

#### 6.1.1. Introduction

Electrical manipulation of magnetization has grown as an essential ingredient in rapidly evolving spintronic research.<sup>80, 81</sup> Switching of nano-scale magnetization can be induced by a spin-polarized current *via* spin-transfer torque,<sup>111, 112</sup> domain wall motion,<sup>113, 114</sup> and/or spin-orbit torque,<sup>115, 116</sup> which are being increasingly utilized for magnetic memory devices under development. Apart from current dissipation, the electric field itself can also be used to control the magnetism in various materials, especially in dilute magnetic semiconductors (DMSs).<sup>80, 81, 117, 118</sup> A gate-voltage-induced accumulation of charge could alter magnetic exchange interactions<sup>80</sup> and eventually lead to changes in magnetic moment, coercivity, anisotropy, and transition temperature. Semiconductor spintronics has garnered increasing attention due to the concept behind the spin field-effect transistor (spin-FET), where the spin precession is governed by the gate-controllable Rashba field.<sup>26, 119</sup> Tuning the magnetization of the source and drain in the spin-FET architecture offers additional state variables in future state-of-the-art electronic applications.

Recently, several nonmagnetic semiconductor NWs, such as silicon,<sup>15, 16</sup> germanium,<sup>14</sup> and other group III–V NWs,<sup>17, 18</sup> have been explored for the spin transport channel with spin sources from conventional ferromagnetic electrodes. Engineering local ferromagnetism of NWs in an accessible manner can promote efficient spin injection<sup>120, 121</sup> and allow the realization of NW-based all-in-one spin FET. Moreover, incorporating electrical tunability of ferromagnetism in NW systems enables us to directly control the source of spins, which can be served as an additional state variable in future nanospintronics. However, comprehensive study on the NW systems for the gate voltage control of ferromagnetism is still lacking and no study has revealed full conversion of magnetoresistance (MR) with electrical field only. Ferromagnetic ZnO NW is particularly interesting candidate for displaying electric field-induced drastic change of MR since the mechanism of magnetic ordering in this system is governed by the carrier concentration, as discussed previously. Thus, the effect of gate voltage on spin exchange coupling in ZnO NWs could significantly vary depending on the initial doping level. It is also desirable to investigate the PL spectra in

individual ZnO NWs and their evolution under gate voltage, since defect-related emissions are directly associated with electron spins in this system.

## 6.2. Results and analysis

### Gate-tunable inversion of magnetoresistance in ferromagnetic ZnO NW

One of the characteristic features of ferromagnetism in ZnO is magneto-transport, which can be used to probe spin-exchange interactions. Here, we demonstrate the effects of gate voltage on magneto-transport in ferromagnetic ZnO NW FET at various temperatures. Figure 6.1 shows the schematic illustration of the magnetotransport of ZnO NW FET device, where the magnetic field ( $H$ ) was applied perpendicular to the axial direction of the NW.

Figure 6.2 displays the MR, defined as  $\Delta\rho/\rho_0 = [\rho(H) - \rho(0)]/\rho(0)$ , measured at  $T = 2\text{K}$  under various gate voltages for  $H = -2\text{ T}$  to  $+2\text{ T}$ . When  $V_g$  was swept from  $-40\text{ V}$  to  $+50\text{ V}$ , the sign of the MR changed from negative to positive. At an intermediate bias ( $+10\text{ V} < V_g < +30\text{ V}$ ), both positive and negative contributions coexisted in the MR. Figure 6.3 shows the magnitude of MR determined at  $H = +1.5\text{ T}$  and field-effect resistance (blue) at  $2\text{ K}$ . While sweeping  $V_g$  from  $-40\text{ V}$  to  $+50\text{ V}$ , the MR was found to change from  $-10.9\%$  to  $4.3\%$ . This dramatic tuning of MR by varying the gate voltage in ferromagnetic ZnO NWs has not been explored before. Recently, Chang *et al.* reported the modulation of MR in Mn-doped ZnO NWs by up to  $2.5\%$  by varying the gate voltage between  $-40\text{ V}$  and  $+40\text{ V}$  at  $2\text{ K}$  and  $7\text{ T}$ . However, magnetic ordering in ferromagnetic ZnO NWs relies highly on the carrier concentration, so that gate voltage-induced MR can significantly vary depending on the initial doping level. According to the observed temperature dependent conductivity, our studied ZnO NWs are typically in the metal-insulator transition regime, which could lead to gate-induced fully converting MR behavior.

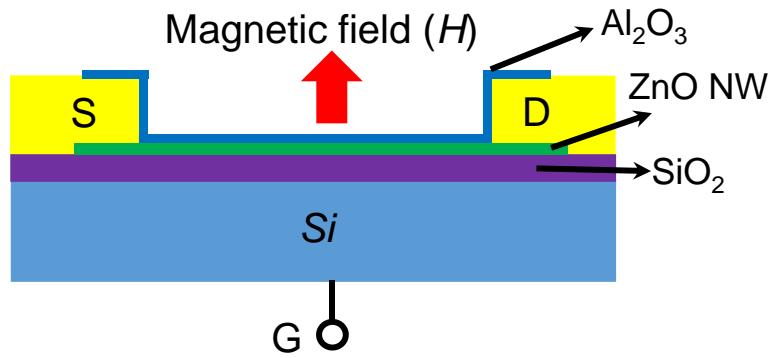


**Figure 6.1.** Schematic view of the magnetotransport in ZnO NW FET device, where the magnetic field is applied perpendicular to the axial direction of the NW.

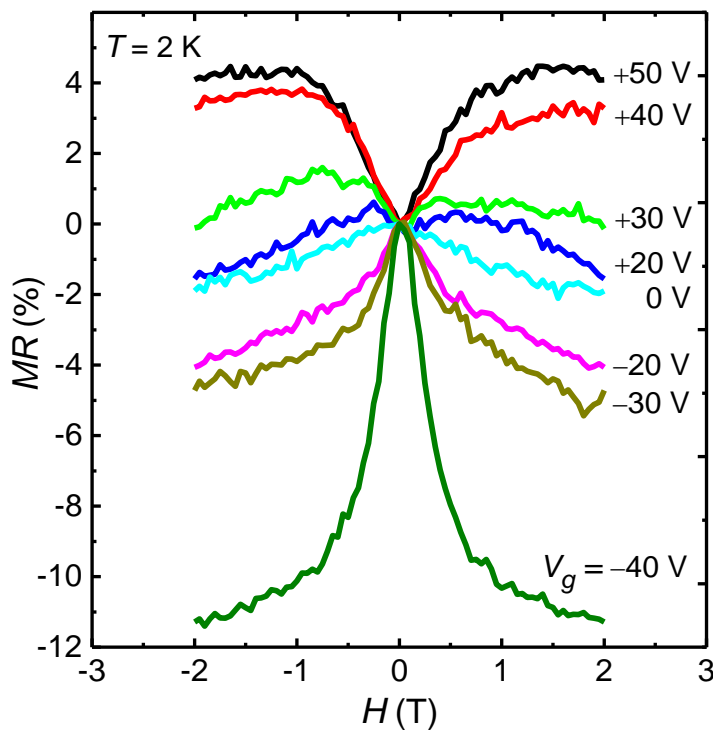


**Figure 6.2.** Gate-dependent magnetotransport of a single ferromagnetic ZnO NW FET device. Gate voltage induced inversion of magnetoresistance from negative to positive was observed under various gate voltages  $V_g$  between  $-40$  V and  $+50$  V at 2K.



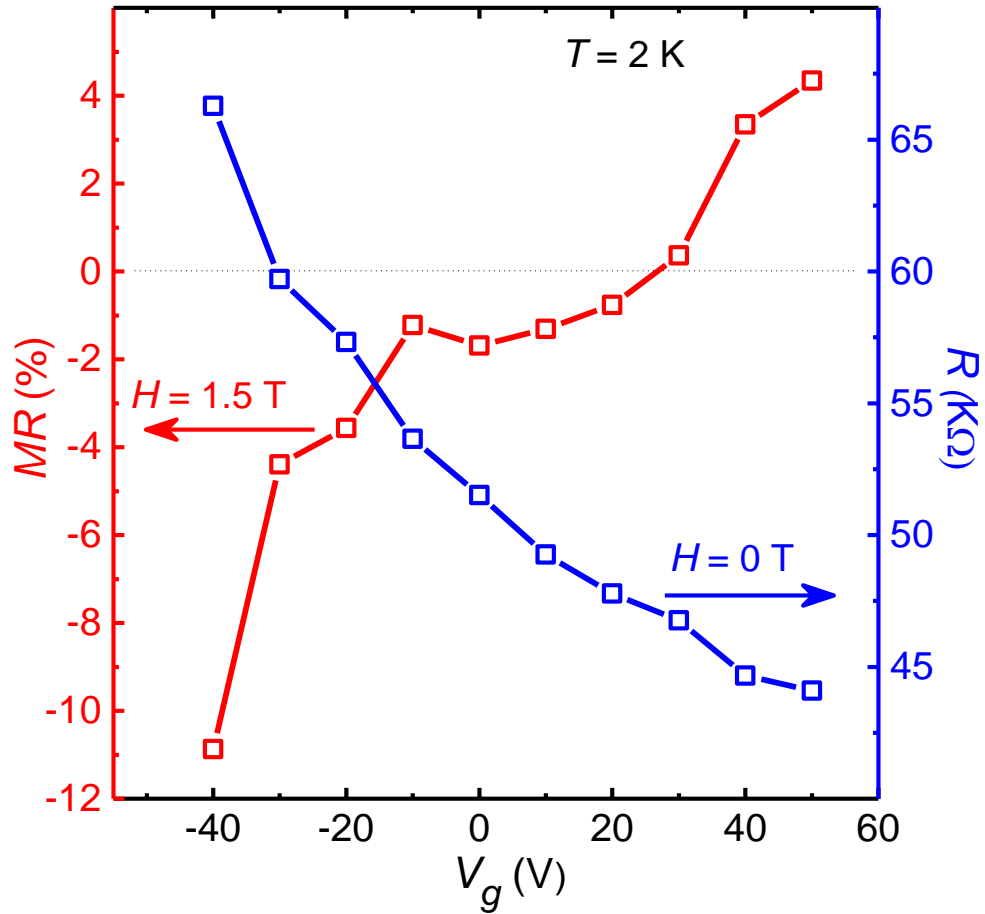


**Figure 6.3.** Gate-dependent MR value of a single ferromagnetic ZnO NW FET device at  $H = 0$  and 1.5 T,  $T = 2$  K. Left axis shows the magnitude of MR as a function of gate voltage, where the MR value is dramatically tuned upon sweeping the gate voltage from  $-40$  V to  $+50$  V at 2 K. Right axis shows the field effect resistance as a function of gate voltage at  $H = 0$  value.

### Temperature dependent magnetotransport of ferromagnetic ZnO NW

The magnitudes of measured MRs at  $V_g = -40$  V and  $-30$  V under various temperatures. The magnitudes of negative MRs decreased with increasing temperature. Figures 6.4 show the temperature dependent behavior of the MR measured at  $V_g = -40$  V and  $-30$  V.

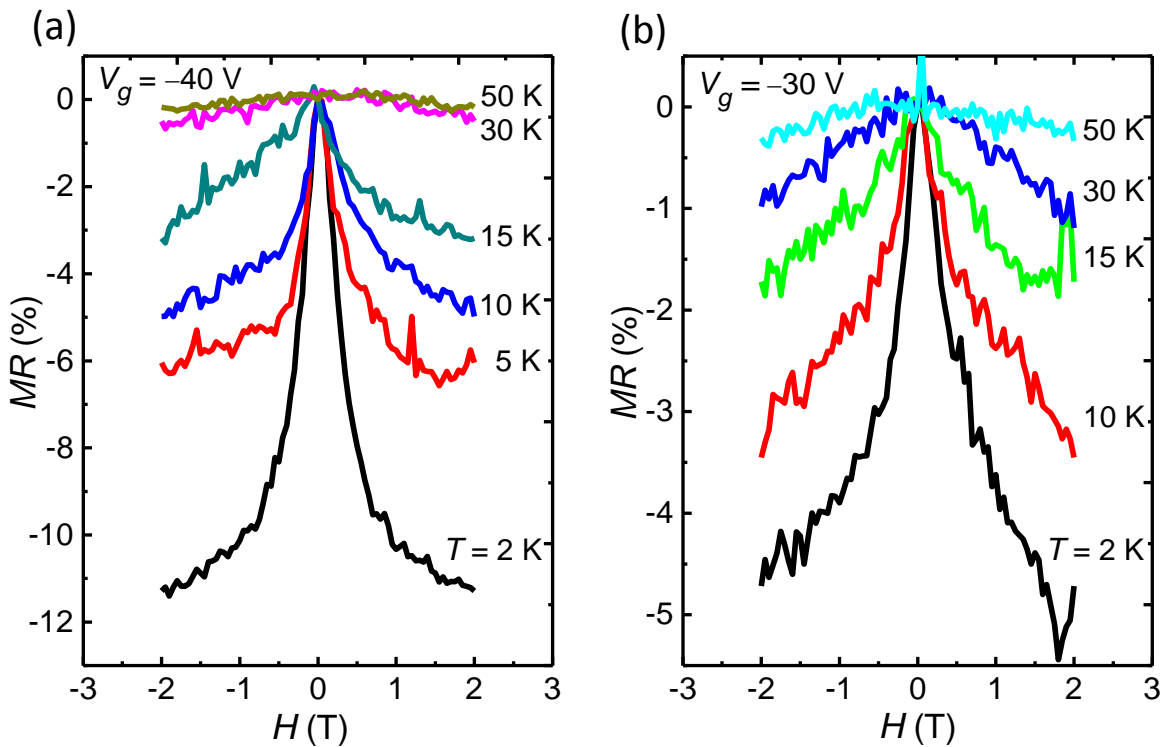


**Figure 6.4. Temperature dependent magnetotransport of a single ferromagnetic ZnO NW.** The observed negative MR for (a)  $V_g = -40$  V and (b)  $V_g = -30$  V under various temperatures. The temperature dependent behavior shows that, the magnitude of MR was dramatically decreased as the temperature was increased.

The magnitudes of measured MRs at  $V_g = +50$  V and  $+40$  V under various temperatures. The magnitude of MR was dramatically decreased as temperature was increased and it turns out to be a negative at 30 K, and then became negligible at 50 K. This temperature dependent inversion of MR sign for  $V_g = +50$  V and  $+40$  V under varied temperatures is shown in above Figure 6.5.

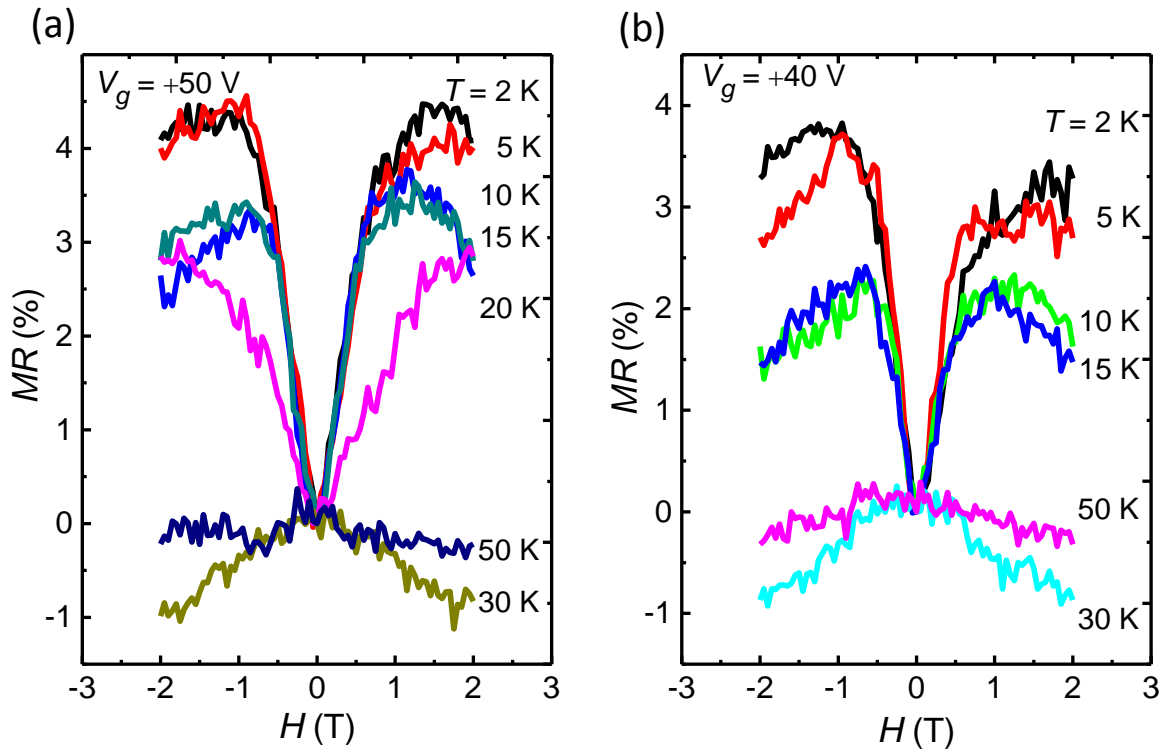


**Figure 6.5.** Temperature dependent magnetotransport of a single ferromagnetic ZnO NW. The observed negative MR for (a)  $V_g = +50$  V and (b)  $V_g = +40$  V under various temperatures. The temperature dependent behavior shows that, the magnitude of MR was dramatically decreased as the temperature was increased and at  $T = 30$  K the sign of MR was inverted from positive to negative before it reaches to the negligible value at 50 K.

The temperature dependence of MR under various gate voltages at  $H = +1.5$  T are summarized in Figure 6.6. When the temperature was lowered to below 30 K, the MR bifurcated into positive and negative values according to the applied gate voltage, and its magnitude increased as the temperature was decreased further.

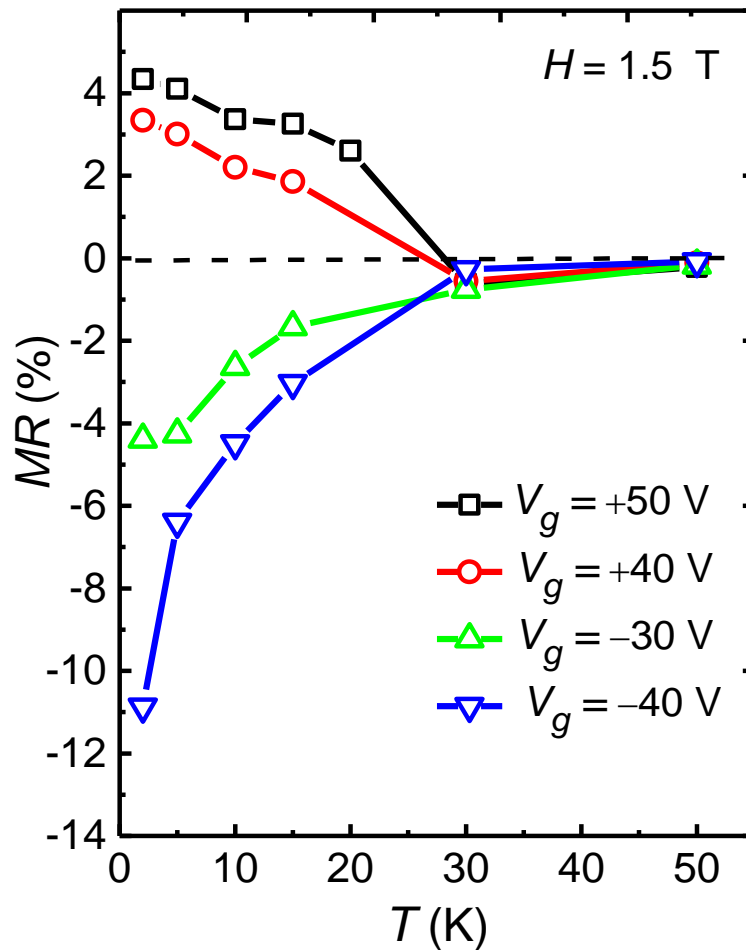


**Figure 6.6.** Summary of temperature dependent magnetotransport of a single ferromagnetic ZnO NW under various gate voltages at  $H = 1.5$  T. When the temperature was lowered to below 30 K, the MR bifurcated into positive and negative values according to the applied gate voltage, and its magnitude increased as the temperature was decreased further.

## Fitting of experimental results with semi-empirical model

Here, we adopted a semi-empirical model from Khosla and Fischer,<sup>122</sup> which describes magneto-transport based on spin-dependent scattering in a system of localized moments with itinerant electrons. The magneto-transport in DMS has been often described within this semi-empirical model.<sup>123, 124</sup> This model was also successfully employed to describe the behavior of MR in undoped,<sup>125</sup> Co-doped,<sup>126, 127</sup> Mn-doped, and Ga-doped ZnO thin films<sup>128</sup> as well as of Al-implanted ZnO NWs.<sup>129</sup> The semi-empirical model of Khosla and Fischer<sup>122</sup> is composed of both positive and negative contributions as follows.

$$\frac{\Delta\rho}{\rho_0} = -a^2 \ln(1 + b^2 H^2) + \frac{c^2 H^2}{1 + d^2 H^2} \quad (6.1)$$

The negative component in Eqn 6.1 is associated with the third-order expansion of the spin exchange Hamiltonian between localized moments and itinerant electrons. Here,  $H$  is the applied magnetic field and  $a$  and  $b$  are parameters given by

$$a = A_1 J D(\varepsilon_F) [S(S + 1) + \langle M^2 \rangle] \quad (6.2)$$

$$b^2 = \left[ 1 + 4S^2 \pi^2 \left( \frac{2JD(\varepsilon_F)}{g} \right)^4 \right] \left( \frac{g\mu_B}{\alpha k_B T} \right)^2 \quad (6.3)$$

where  $J$  is the exchange interaction energy,  $D(\varepsilon_F)$  is the density of states (DOS) at the Fermi level,  $\langle M^2 \rangle$  is the average of the square of the magnetization,  $\mu_B$  is the Bohr magneton,  $k_B$  is Boltzmann constant, and  $\alpha$  is a numerical factor that is on the order of unity.<sup>130, 131</sup> The quantities  $S$  and  $g$  are the total spin and the effective Lande  $g$  factor of the localized magnetic moments, respectively. The parameter  $A_1$  is a measure of the spin scattering contribution to the total MR.

The positive component in Eqn 6.1 is derived from a two-band model<sup>122, 123, 132</sup> with asymmetric conductivities for spin-split sub-bands. The coefficients  $c$  and  $d$  are related to the band parameters and are given by

$$c^2 = \frac{\sigma_1 \sigma_2 (\mu_1 + \mu_2)^2}{(\sigma_1 + \sigma_2)^2} \quad (6.4)$$

$$d^2 = \frac{(\sigma_1 \mu_2 - \sigma_2 \mu_1)^2}{(\sigma_1 + \sigma_2)^2} \quad (6.5)$$

where  $\mu_i$  and  $\sigma_i$  are the mobilities and conductivities of the carriers in the two sub-bands. The subscripts 1 and 2 denote the majority-spin and minority-spin carriers, respectively.

## Discussion

Gate-field-induced inversion of MR, especially in semiconductor systems, is often attributed to the tuning of Rashba spin-orbit coupling<sup>133</sup>. Here, the gate-controlled Rashba SOC affects the phase coherence of carrier electrons, which leads to a change in the quantum interference of self-crossing trajectories, and eventually switches charge transport from the weak localization (WL) limit to the weak anti-localization (WAL) limit.<sup>69, 70</sup> However, one has to be careful about describing MR in terms of quantum corrections because phase coherence can be easily destroyed with a small applied magnetic field, and the typical magnetic field windows for MR changes by WL and WAL are narrow (on the order of  $\sim 100$  Oe).<sup>134</sup> But, the MR in our sample was observed to persist in a relatively strong field. Besides, both WL and WAL effects occur only in the weakly localized limit ( $k_F l > 1$ ). In our case, the  $k_F l$  was estimated to be  $\sim 0.5$ , indicating our sample to be in the strongly localized regime. There are also other possible candidates for the mechanisms of the observed positive and negative MRs.<sup>135</sup> In particular, quantum correction in variable range hopping can produce both positive and negative MR.<sup>136, 137</sup> Other mechanisms, such as wave function shrinkage<sup>138</sup> and electron spin blockade<sup>139</sup> can lead to positive MR. However, the temperature dependence of the positive MR in these mechanisms can be scaled as  $T^{-2}$ ,<sup>135</sup> which is far from what we have observed in our system (see Figure 6.6).

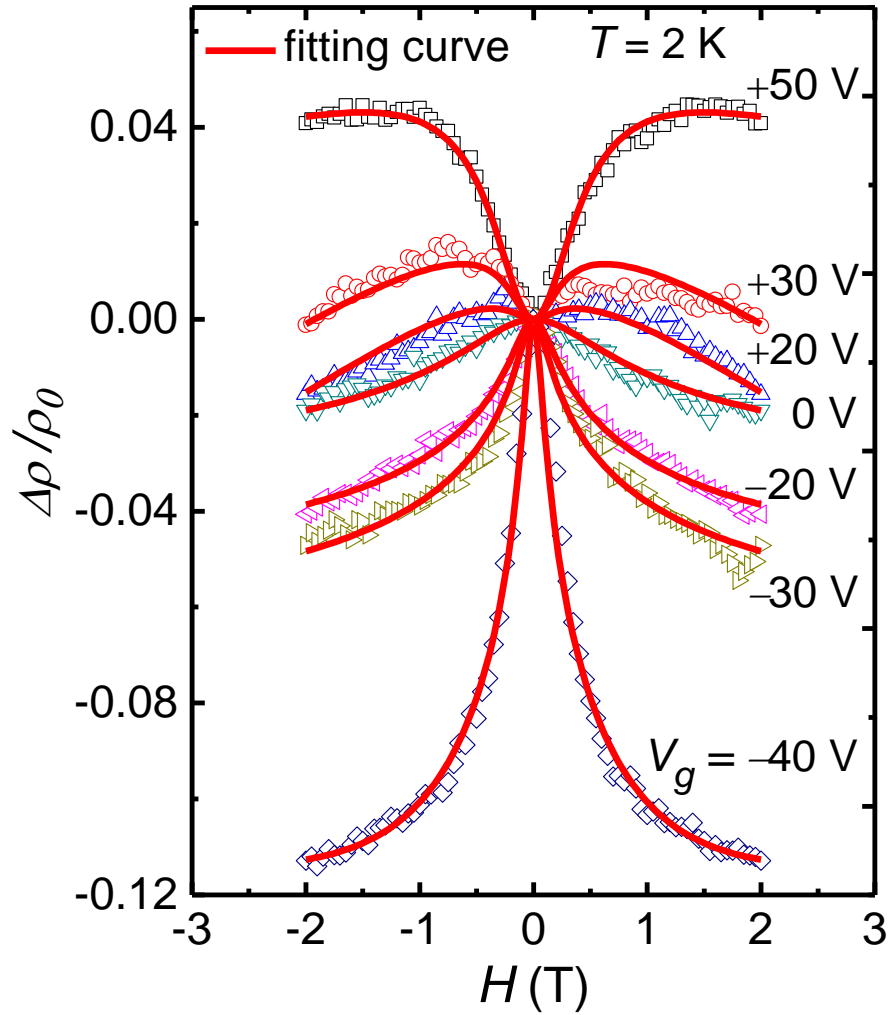


**Figure 6.7.** Description of the fit of a semi-empirical model to the measured MR values. Eqn 6.1 curves fit to the measured MR values at  $T = 2$  K for various gate voltages in ZnO NW. All curves fit well to the collected data over all gate voltages.

Figure 6.7 display curves from Eqn 6.1 of semi-empirical model fit to the measured MR values. All curves fit well to the collected data over all applied gate voltages. The obtained fitting parameters  $a$ ,  $b$ ,  $c$ , and  $d$  are listed in Table 6.1. As shown in Figure 6.8, the value of  $b$ , which determines the magnitude of negative MR, was found to decrease as the gate voltage was increased from  $-40$  V to  $+30$  V. In DMS film, it was also found that the increasing magnetic doping suppress the negative MR component.<sup>123</sup> Having stronger exchange between localized moments weakens the change in degree of moment alignment by the application of an external field. Since negative MR originates from spin-dependent scattering by localized moments, enhanced exchange interactions reduce the magnitude of the MR. Figure 6.9 displays the band parameters  $c$  and  $d$  as a function of gate voltage at 2 K. The obtained band parameters  $c$  and  $d$  are strongly depending on the applied gate voltage. This bias dependent behavior of fitting parameters might be associated with the enhanced exchange interaction with increasing gate voltage.

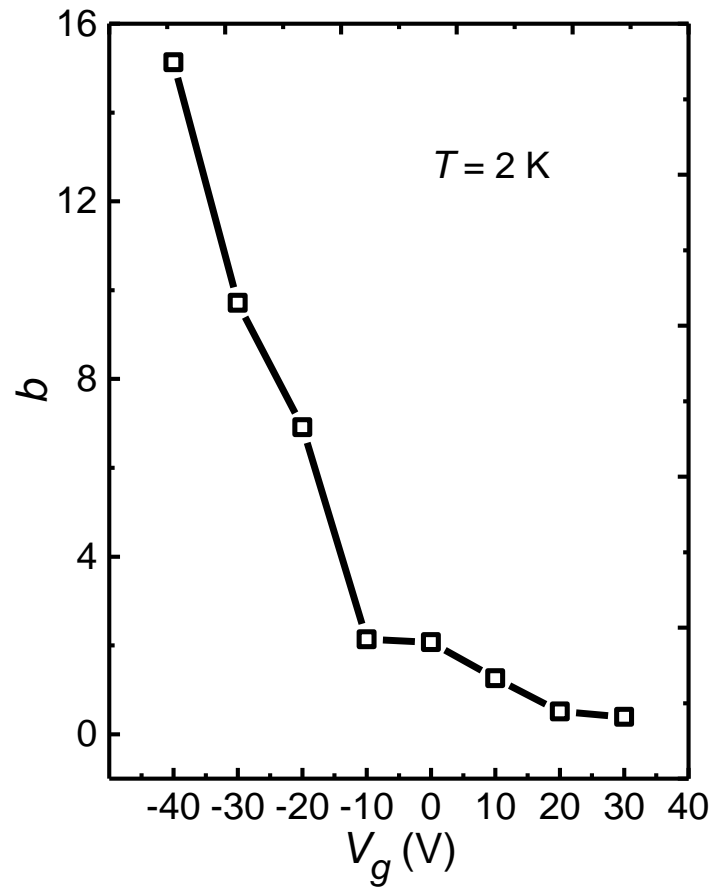
We further display curves from Eqn 6.1 of semi-empirical model to the measured temperature dependent MR values for various gate voltages  $V_g = +50$  V,  $+40$  V,  $-30$  V and  $-40$  V. Eqn 6.1 produces qualitatively good fits over a wide temperature range as shown in Figures 6.10 (a-d). The extracted fitting parameters  $a$ ,  $b$ ,  $c$ , and  $d$  for the observed MR values are listed in Tables 6.2-6.3.

Figure 6.11 displays the plot of  $b$  vs  $T^{-1}$  for gate voltages  $V_g = -40$  V and  $-30$  V. The obtained plot of  $b$  vs  $T^{-1}$  showing the linearity down to 10 K. This behavior well corresponds to Eqn 6.3 of the semi-empirical model. However, large deviation in  $T^{-1}$  behavior of parameter  $b$  was observed below 10 K. This might be associated with the enhanced  $g$  factor at lower temperature due to increased spin relaxation. Similar trend in temperature dependent  $g$  factor has been reported in DMS system of (Ga,Mn)As.<sup>140</sup> Figure 6.12 shows the plot of the obtained band parameters  $c$  and  $d$  as a function of temperature at  $V_g = 50$  V, The band parameters  $c$  and  $d$  are tuning with temperature at particular gate voltage.



**Table 6.1:** Parameters describing the fit of the semi-empirical model to the observed MR values for various gate voltages at  $T = 2$  K

	$V_g$	$a$	$b$	$c$	$d$
@ $T = 2$ K	-40	0.1411	15.132	0.09224	0.34218
	-30	0.09222	9.7133	0.02722	0.3146
	-20	0.08805	6.91347	0.02661	0.28654
	-10	0.08002	2.13303	0.02547	0.26572
	0	0.08415	2.07536	0.01971	0.1945
	+10	0.09521	1.25917	0.25321	4.406
	+20	0.16616	0.50926	0.28567	4.26552
	+30	0.18678	0.38903	0.4876	3.8796
	+40	0.08311	0.45422	0.50177	2.53848
	+50	0.1032	0.49211	0.51995	2.28376



**Figure 6.8.** The obtained fitting parameter  $b$  as a function of gate voltage  $V_g$  at  $T = 2$  K.

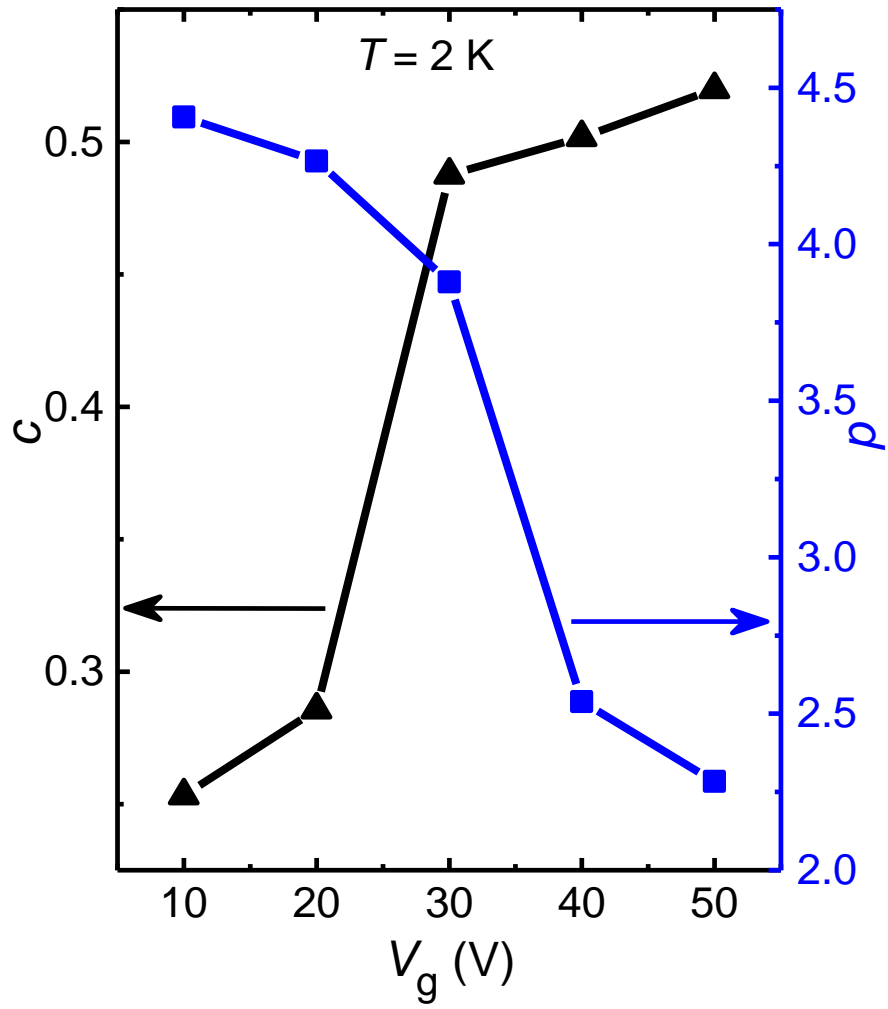


**Figure 6.9.** The obtained fitting parameters  $c$  and  $d$  of Eqn 6.1 obtained at  $V_g = +50 \text{ V}$ .

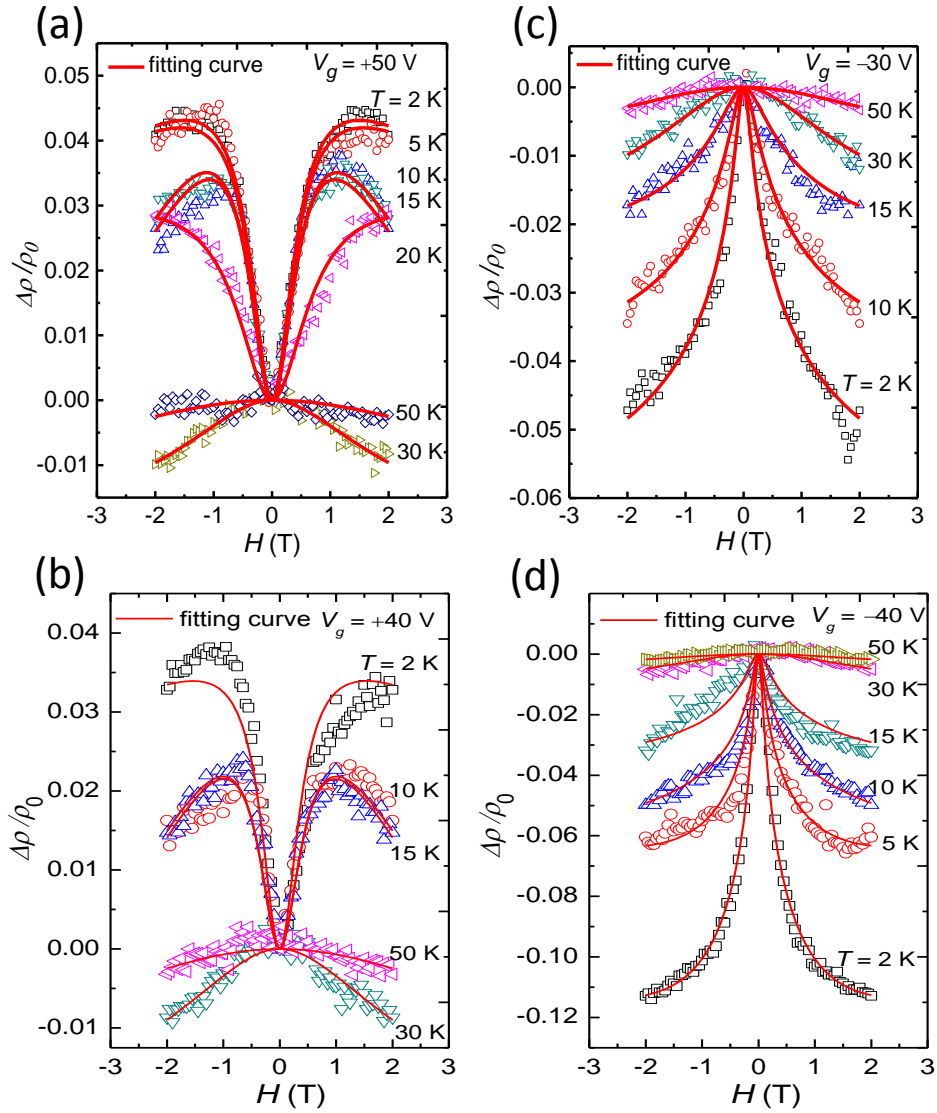


**Figure 6.10.** Description of MR in ferromagnetic ZnO NW by fitting the measured values with a semi-empirical model of Eqn 6.1. (a-b) Fitting the measured values with semi-empirical model, at a gate voltage of  $V_g = +50$  V and +40 V under varied temperatures. The MR values were observed to decrease with increasing temperature, and became negative at around 30 K. The MR was negligible at 50 K. (c-d) Fitting measured MR values with a semi-empirical model, at a gate voltage of  $V_g = -30$  V and -40 V under varied temperatures. In all above cases, the experimental values are in good agreement with the semi empirical model.

**Table 6.2:** Parameters describing the fit of the semi-empirical model to the observed MR values for various temperatures at  $V_g = -40$  V and  $-30$  V

	$T$	$a$	$b$	$c$	$d$
@ $V_g = -40$ V	2	0.1411	15.132	0.09224	0.34218
	5	0.10648	13.73	0.06145	0.2601
	10	0.09007	11.63	0.0243	0.253
	15	0.07665	6.823	0.0223	0.2304
	30	0.07466	0.66433	0.0151	0.16
	50	0.07774	0.4316	0.021	0.1309
@ $V_g = -30$ V	2	0.09222	9.7133	0.02722	0.3146
	10	0.08294	5.58	0.02396	0.2441
	15	0.07041	3.32	0.0213	0.2014
	30	0.08834	0.90507	0.0201	0.1584
	50	0.0898	0.4227	0.01991	0.12595

**Table 6.3:** Parameters describing the fit of the semi-empirical model to the observed MR values for various temperatures at  $V_g = +40$  V and  $+50$  V

	$T$	$a$	$b$	$c$	$d$
@ $V_g = +40$ V	2	0.08311	0.45422	0.50177	2.53848
	5	0.08233	0.41	0.456	2.45
	10	0.16299	0.44298	0.401	2.24658
	15	0.16785	0.4401	0.4	2.245
	30	0.094	0.71811	0.0156	0.128
	50	0.09	0.30019	0.0035	0.009
@ $V_g = +50$ V	2	0.1032	0.49211	0.51995	2.28376
	5	0.09928	0.471179	0.50189	2.24453
	10	0.18417	0.4621	0.469	2.10707
	15	0.1861	0.4434	0.4609	2.04361
	20	0.09	0.2	0.25722	1.41466
	30	0.09125	0.82057	0.01822	0.132
	50	0.09168	0.31024	0.0076	0.009

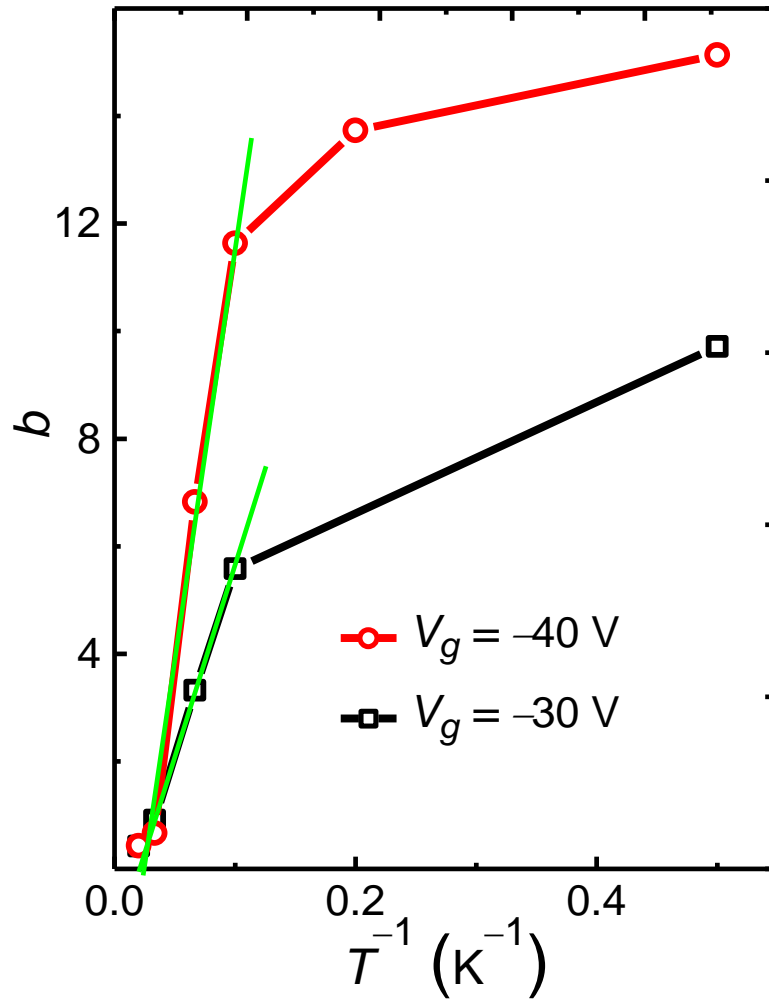


**Figure 6.11.** The obtained fitting parameter  $b$  as a function of temperature for gate voltages  $V_g = -40 \text{ V}$  and  $-30 \text{ V}$ .

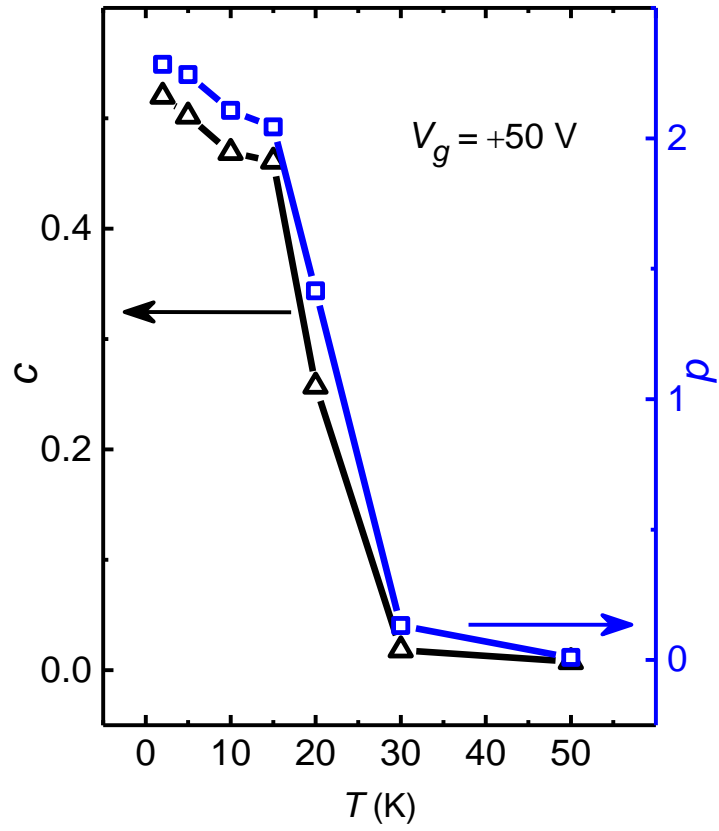


**Figure 6.12.** The temperature dependent parameters  $c$  and  $d$  of Eqn 6.1 obtained at  $V_g = +50$  V.



## Reproducibility of the Results

In this section, we show the reproducibility of the gate-induced inversion of MR in our ferromagnetic ZnO NW devices. As discussed in the previous section, the behavior of MR in ZnO NWs strongly depends on the doping level. Within the same batch of sample, all the MR characteristics were found to be reproducible despite a number of device fabrication processes.

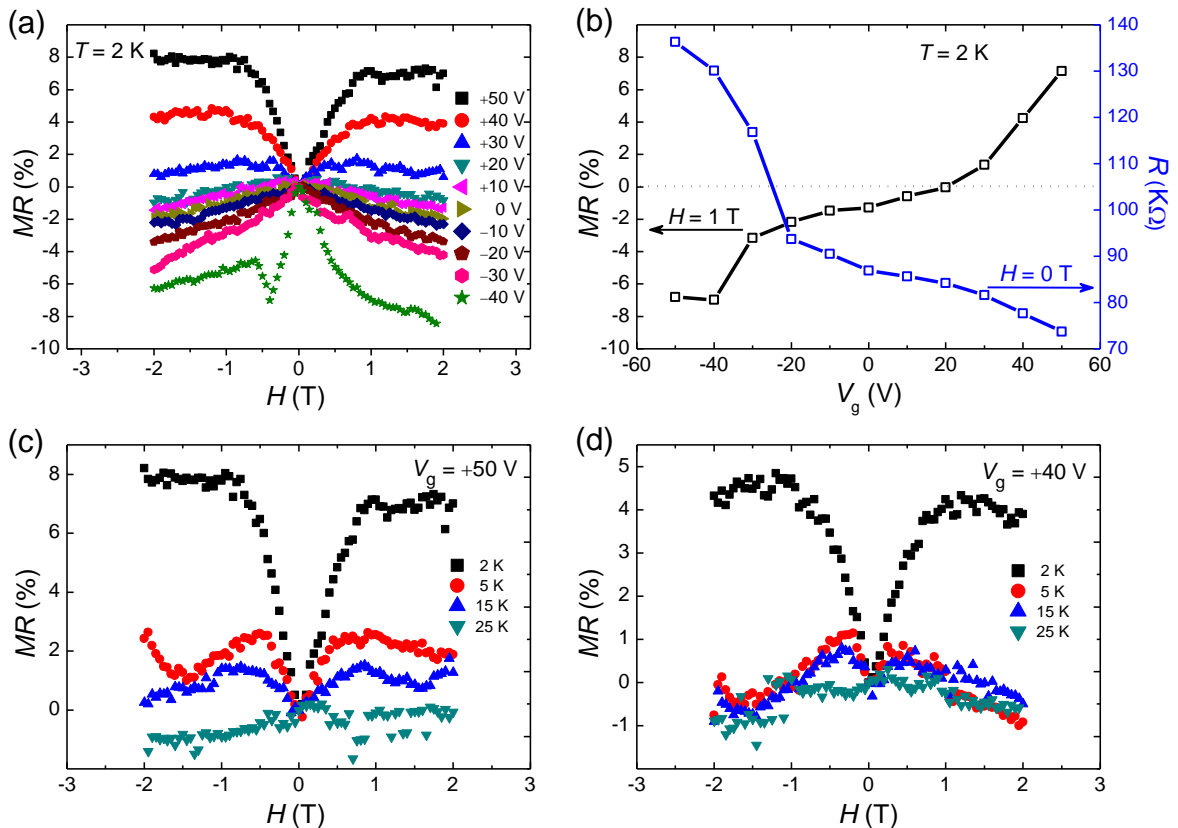


**Figure 6.13: Reproducibility of the gate dependence of MR in our ferromagnetic ZnO NW FET (device B).** (a) Gate-tunable inversion of MR at  $T = 2$  K. (b) Gate-dependent MR value of at  $H = 0$  and 1 T,  $T = 2$  K. Left axis shows the magnitude of MR as a function of gate voltage, where the MR value is dramatically tuned upon sweeping the gate voltage from  $-40$  V to  $+50$  V at 2K. Right axis shows the field effect resistance as a function of gate voltage at  $H = 0$  value. (c-d) Temperature dependence of MR collected at  $V_g = +50$  V and  $+40$  V.

### 6.3. Threshold voltage dependence of Giant magnetoresistance in ferromagnetic ZnO NW FET devices

In general, charge transport in ZnO NWs strongly relies on the native doping level and varies from hopping to the weakly localized limit<sup>56, 57</sup>. Thus, the magnetic exchange interaction between randomly distributed defect-induced spins is also subject to the doping concentration. Therefore it would be very intriguing to study how the influence of the initial level of native defects and applied gate voltage on the performance of the ZnO NW FET devices and its corresponding magneto transport studies.

In this section, we study how the effects of native defects on electric and magneto-transport in ferromagnetic ZnO NW FET device. Here we fabricated and characterized three types of NWs, whose initial doping levels lies from insulating regime to the metal-insulating transition regime. According to the observed transport studies we confirm that, the NW used for device # 1, typically lies in the insulation regime, whereas the NW used for device # 3, 2, lies near the metal-insulator transition regime. Figure 6.14 displays the device # 1, magnetoresistance (MR), defined as  $\Delta\rho/\rho_0 = [\rho(H) - \rho(0)]/\rho(0)$ , measured at  $T = 2\text{K}$  under gate voltages  $V_g = +35\text{ V}$  and  $+40\text{ V}$  for  $H = -3\text{ T}$  to  $+3\text{ T}$ . In this study the magnetic field ( $H$ ) was applied perpendicular to the axial direction of the NW. As shown in Figure 6.14 (a), the giant MR was observed and tuned by the back-gate voltage  $V_g$  swept from  $+35\text{ V}$  to  $+40\text{ V}$ . Figure 6.14 (b) shows the maximum extracted value of magnitude of MR (right axis) and zero field resistance (left axis) as a function of gate voltage  $V_g$  at  $2\text{ K}$ . While sweeping  $V_g$  from  $+35\text{ V}$  to  $+50\text{ V}$ , the MR was found to change from  $\sim 50\%$  to  $\sim 73\%$ . Figure 6.15 shows the performances of the three type devices as explained above. 6.15 (a) shows the conductance as a function of  $V_g$  at  $T = 300\text{ K}$ . The performance of field effect conductance is significantly varies for three types of NWs with different initial native doping levels. Figure 6.15 (b) shows the corresponding MR curves for Devices # 1 and 3 at  $V_g = +40\text{ V}$  and  $T = 2\text{ K}$ . The inset shows the extracted MR value as a function of device number (#) at  $V_g = +40\text{ V}$  and  $H = 1\text{ T}$ . The value of MR decrease while moving from device #1 (NW lies at the insulation regime) to device # 3 (NW lies at the metal-insulator transition regime). However, magnetic ordering in ferromagnetic ZnO NWs relies highly on the carrier concentration, so that gate voltage-induced MR can significantly vary depending on the initial doping level. From the observation of the MR value and its dependence on the initial doping level of NW and the value found to be increasing while moving from near metal-insulator transition to insulator regime. However further comprehensive studies are needed to conclude the above result.

Giant Magnetoresistance in ZnO NWs

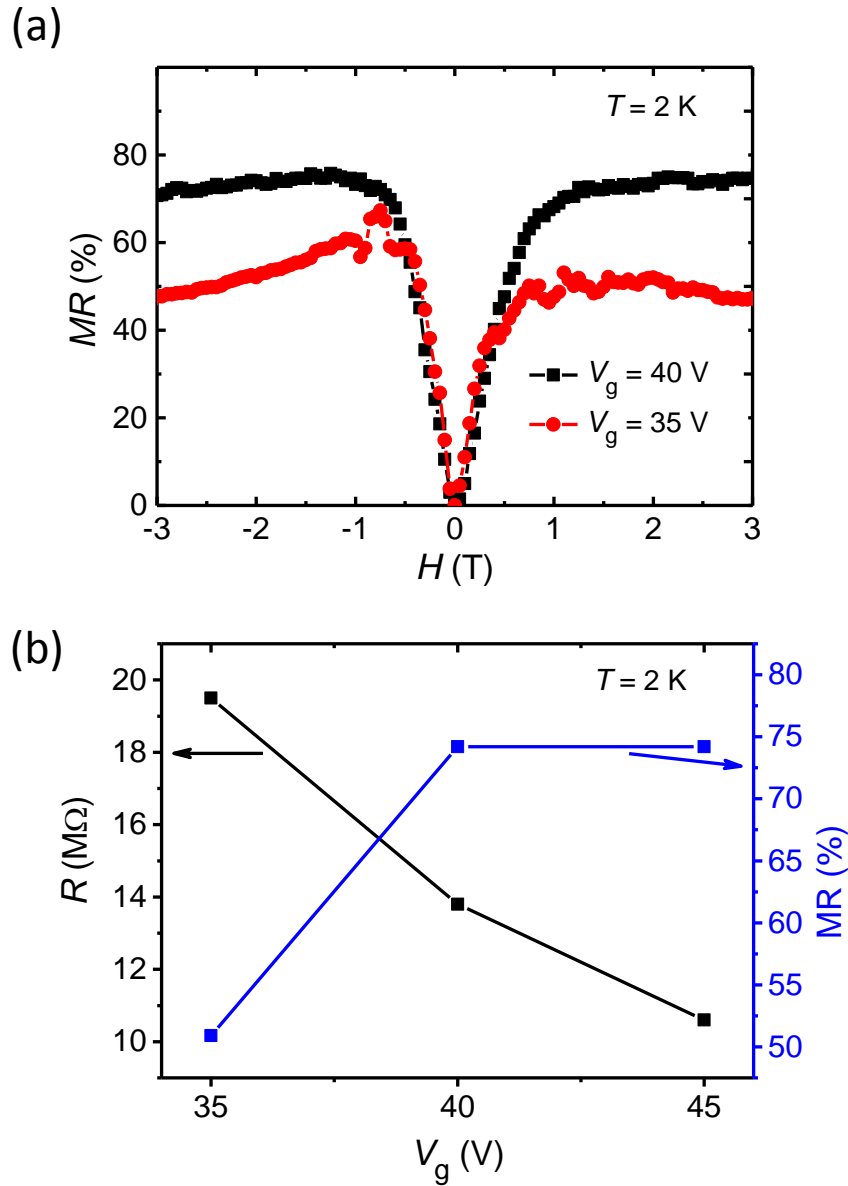


**Figure 6.14. Gate-dependent magnetotransport of a ferromagnetic ZnO NW.** (a) Gate voltage induced tuning of giant magnetoresistance for  $V_g = +40$  V and  $+35$  V at  $T = 2$  K. (b) The right axis shows the extracted value of maximum MR, and left axis shows the zero field resistance as a function of gate voltage.

Comparison of the obtained MR values for three types of ZnO NWs

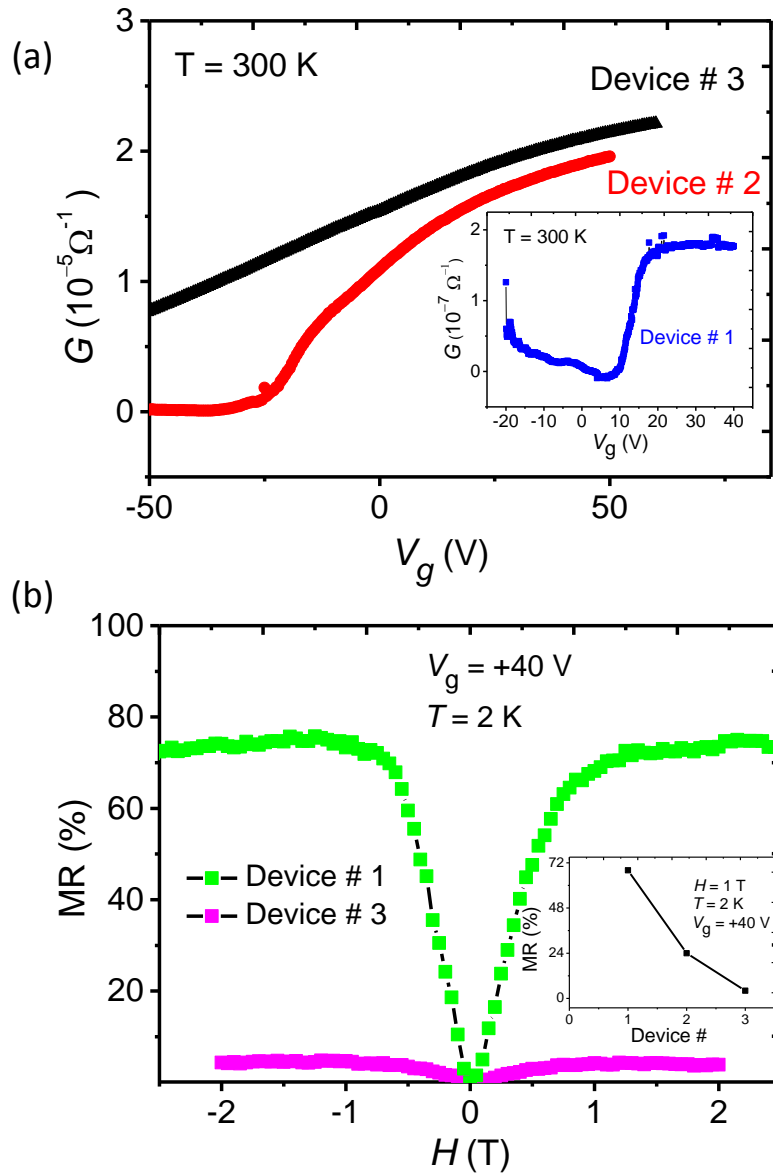


**Figure 6.15.** (a)  $V_g$ - $I_d$  characteristics of a ZnO NW FET devices at  $T = 300$  K. The FET characteristics of the Devices # 1,2,3 was governed by the native doping concentration in ZnO NWs, where Device #1 lies at the insulator regime, devices # 2,3 lies at the crossover of metal-insulator transition regime. (b) The corresponding MR curves for Devices # 1 and 3 at  $V_g = +40$  V. The inset shows the extracted MR value as a function of device number (#) at  $V_g = +40$  V and  $H = 1$  T.

## 6.4. Conclusion:

In summary, we have shown the ability to dramatically change MR in ferromagnetic ZnO NWs by applying gate voltage for wide range of temperature. Changes in the carrier concentration induced by the gate voltage greatly influenced the MR signal, whose sign was observed to change from negative to positive when the gate voltage was swept from  $-40$  V to  $+50$  V. We note that such a full conversion of MR was observed for ZnO NW with the initial doping level lying at metal-insulator transition regime. The behavior of the observed MR fits well the semi-empirical model of Khosla and Fischer. The obtained fitting parameters show that the gate voltage-induced carrier concentration facilitates exchange interactions between localized moments. The observed effect of applying a gate voltage on the PL spectrum of an individual device (shown in chapter 7) was also consistent with magnetic ordering through carrier-mediated exchange interactions, which can be effectively tuned by the applied gate voltage. We also studied the gate tunable giant MR value at  $T = 2$  K in ZnO NW FET device with the initial doping level of NW lies at the insulator region. While sweeping  $V_g$  from  $+35$  V to  $+50$  V, the large extracted value of MR was found to change from  $\sim 50\%$  to  $\sim 73\%$ . Furthermore, we also observed the MR value and its dependence on the initial doping level of NW. We found that the MR value increasing while moving from near metal-insulator transition to insulator regime.

Our study solely displayed fully controllable MR in NW system by applying electrical field only. Along with efforts for realizing spintronic device with nano-materials, accessible tuning of ferromagnetism in NW is highly desirable for the functional operation of spintronic device, where device resistance switches depending on the magnetic alignment of ferromagnetic layers. ZnO NW exhibits rich variation of robust ferromagnetic properties compared to other DMS systems. However, its relatively low mobility needs to be improved to facilitate coherent spin transport. Further challenge for the realization of fully functional spin-FET using ZnO NW is the incorporation of Rashba spin-orbit coupling, which has never been demonstrated in this system. Nevertheless, our study has shown the ability to markedly manipulate the ferromagnetism in a NW system, which provides the promise of additional degrees of freedom for data processing in future nano-spintronics.

## Chapter 7

# Gate-tunable photoluminescence study of single ferromagnetic ZnO nanowire FET devices

---

### 7.1. Experiment: UV Confocal microscopy

The PL spectral imaging of a single ZnO NW device with gate voltage control was performed using the confocal method shown in the schematic of Figure 7.1. A 355-nm-wavelength laser line of a diode-pumped solid-state laser was used for the PL excitation. A 0.9 NA objective lens was used to tightly focus the laser light onto the sample, and the PL emission from the sample was collected with the same objective lens and guided to the spectrometer equipped with a cooled charge-coupled device (CCD), which was synchronized with the scanning of the sample stage. The laser power applied to the sample was typically 50  $\mu$ W and an acquisition time of 150 ms per pixel was used for PL spectral imaging. Spectral images for which each pixel contained the full PL spectrum were obtained for back gate voltages of 0 V and +30 V.

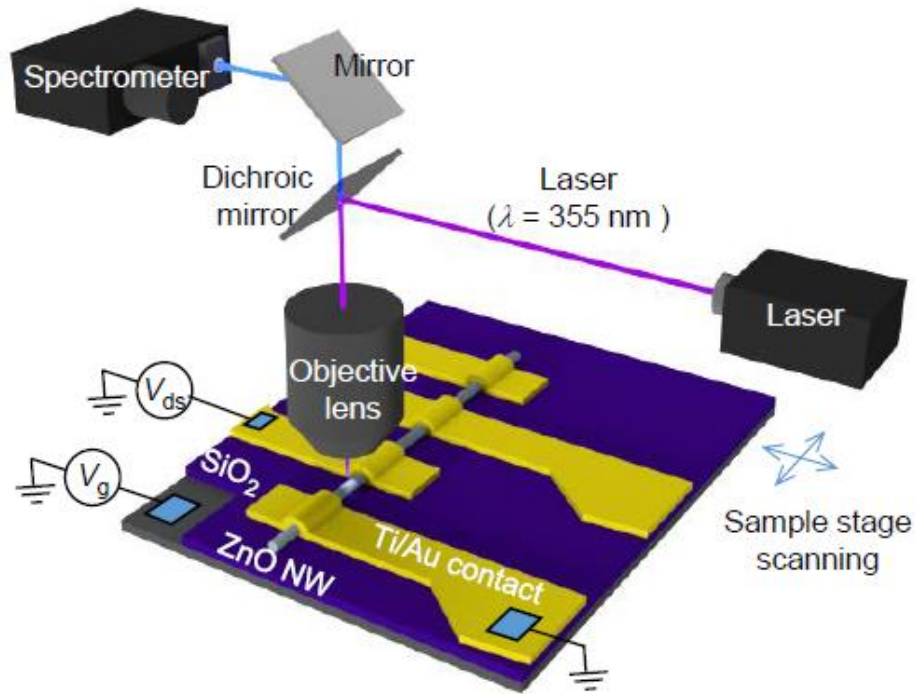


**Figure 7.1.** Schematic view of the UV confocal PL spectral imaging of a single ZnO NW device with the application of gate voltage. The laser power applied to the sample was typically 50  $\mu\text{W}$  and an acquisition time of 150 ms per pixel was used for PL spectral imaging.

## 7.2. Results and Discussion

### 7.2.1. PL imaging of a Single ZnO NW FET Device

In order to clarify the presence of ferromagnetism and oxygen vacancies in the studied ZnO NW FET, we performed a UV confocal PL study for the individual device using a lab-made confocal microscope as shown in Figure 7.1. Typical PL intensity mapping for individual ZnO NW device is shown in Figure 7.2(a), which was collected by an excitation of 355 nm laser line.

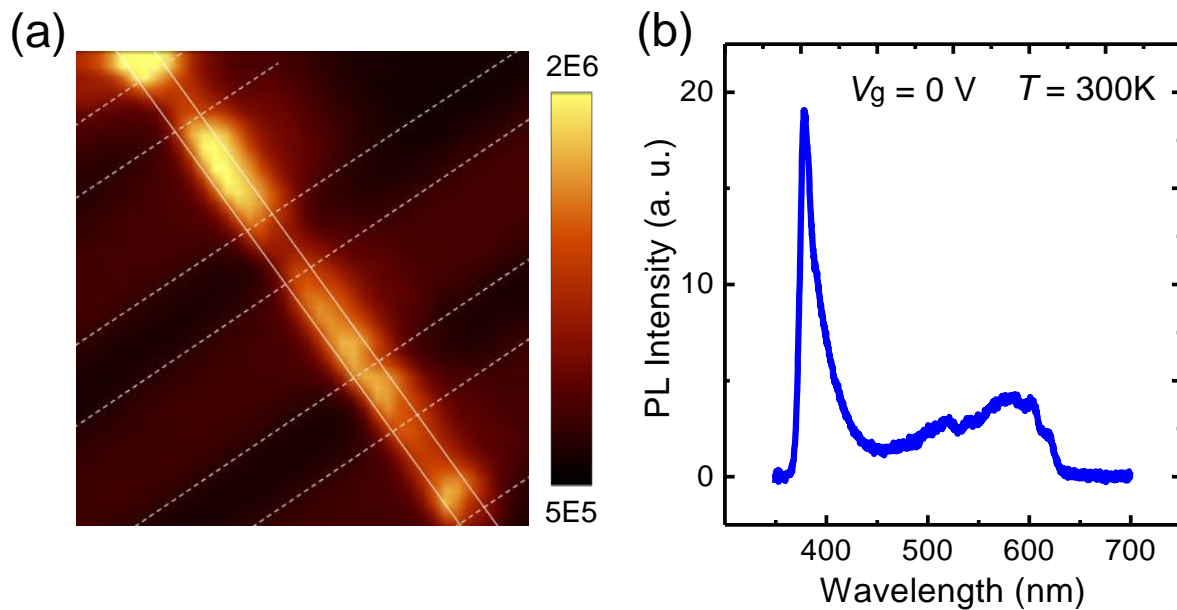


**Figure 7.2. Optical properties of the studied ZnO NW.** (a) The RT-PL intensity mapping of single ZnO NW device with zero gate bias. Contrast scale of the PL image represents the photon counts, i.e., PL intensity. (b) RT-PL spectra of a single ZnO NW device.



Figure 7.2(b) shows a PL spectrum measured from a ZnO NW device exhibiting the general feature of near-band-edge ultraviolet (UV) emission at 380 nm and a broad deep-level emission<sup>62</sup> in the visible region. The natively doped ZnO, as shown in the schematic band diagram of Figure 7.3, has shallow donor levels typically lying approximately 50–100 meV below the conduction band edge.<sup>56</sup> Accordingly, the main UV emission was accompanied by a satellite feature at about 395 nm (Figure 7.2(b)). The broad DLE in the visible region can be attributed to the transition involving optical centers from the deep levels. The origin of the DLE has been controversial since this emission can be attributed to several kinds of defects and vacancies. The commonly reported defects present in ZnO-based nanostructures are oxygen vacancies, zinc vacancies, interstitial zinc, and adsorbed molecules. However, it has been most widely accepted that the several DLEs are associated with oxygen vacancies with different charged states.<sup>46, 47, 50, 141-146</sup> Deconvolution of the DLE in natively doped ZnO NWs generally produces three main features.

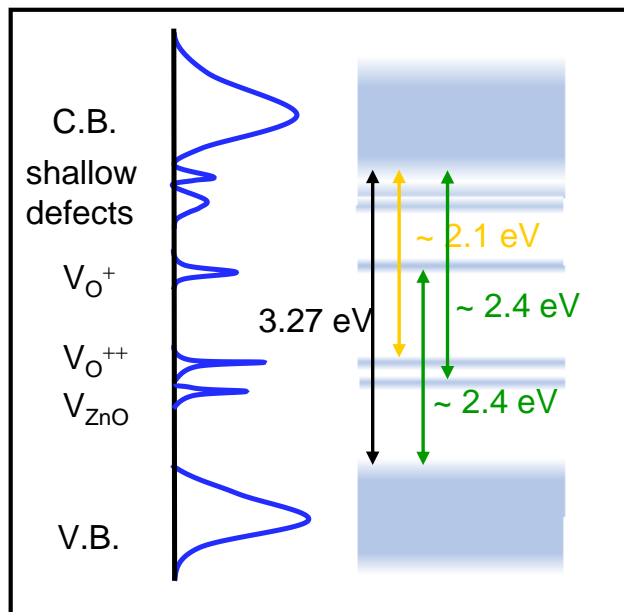


**Figure 7.3.** Schematic illustration of the energy band diagram of the ZnO NW including various defect-related energy levels.

As shown in Figure 7.3, the green emission ( $\sim 520$  nm) is associated with singly charged oxygen vacancies ( $V_{O^+}$ ), which have been attributed to localized moments.<sup>47, 144, 146</sup> A recent study suggested that the presence of  $V_{O} + V_{Zn}$  di-vacancies ( $V_{ZnO}$ ) can also contribute to the green emission, since it is located around  $\sim 0.9$  eV above the valence band edge.<sup>147, 148</sup> The spinless doubly charged oxygen vacancies ( $V_{O^{++}}$ ) yield a yellow emission ( $\sim 570$  nm).<sup>47, 144, 146</sup> And the orange-red emission ( $\sim 610 - 750$  nm) is ascribed to the excess oxygen on the ZnO surface<sup>47, 141</sup> and/or donor-acceptor recombination process between  $V_{O}$  and  $V_{Zn}$  defects.<sup>125</sup> The relative intensity and location of these peaks essentially depend on how the material was processed, such as growth conditions, annealing, *etc.* Figure 7.2(b) shows the strong suppression of the orange-red emission peak, indicating a lack of excess oxygen on the NW surface and/or  $V_{Zn}$ . This lack of excess oxygen might be due to the surface modification of the ZnO NW with the  $Al_2O_3$  capping layer. As discussed in the Introduction, the correlation between the DLE of singly charged oxygen vacancies  $V_{O^+}$  and ferromagnetism has been well established according to several previous reports.<sup>46-50, 149</sup> The observation of green emission in an individual ZnO NW device indicates that the ZnO NW in our FET carries oxygen vacancy induced ferromagnetism.

### 7.2.2. Gate tuned PL imaging of a Single ZnO NW device

We also performed a PL study on an individual NW device to investigate how the gate voltage affects emissions associated with both free carriers and localized moments. Figures 7.4(a and b) display PL images of a single ZnO NW FET with non-overlapping emission wavelength ranges and with zero gate bias. A wavelength range of 370–450 nm was chosen to display the main band edge emission (Figure 7.4(a)), while 480–640 nm was the range selected to display the oxygen vacancy-induced emission (Figure 7.4(b)). PL images for the same range of wavelength, but under a gate voltage  $V_g$  of +30 V, are shown in Figure 7.4(c and d). When applying a gate bias, the intensity of the main emission was strongly quenched, whereas defect-related peaks maintained their emission intensities. We inspected several NW devices and observed the same trend.

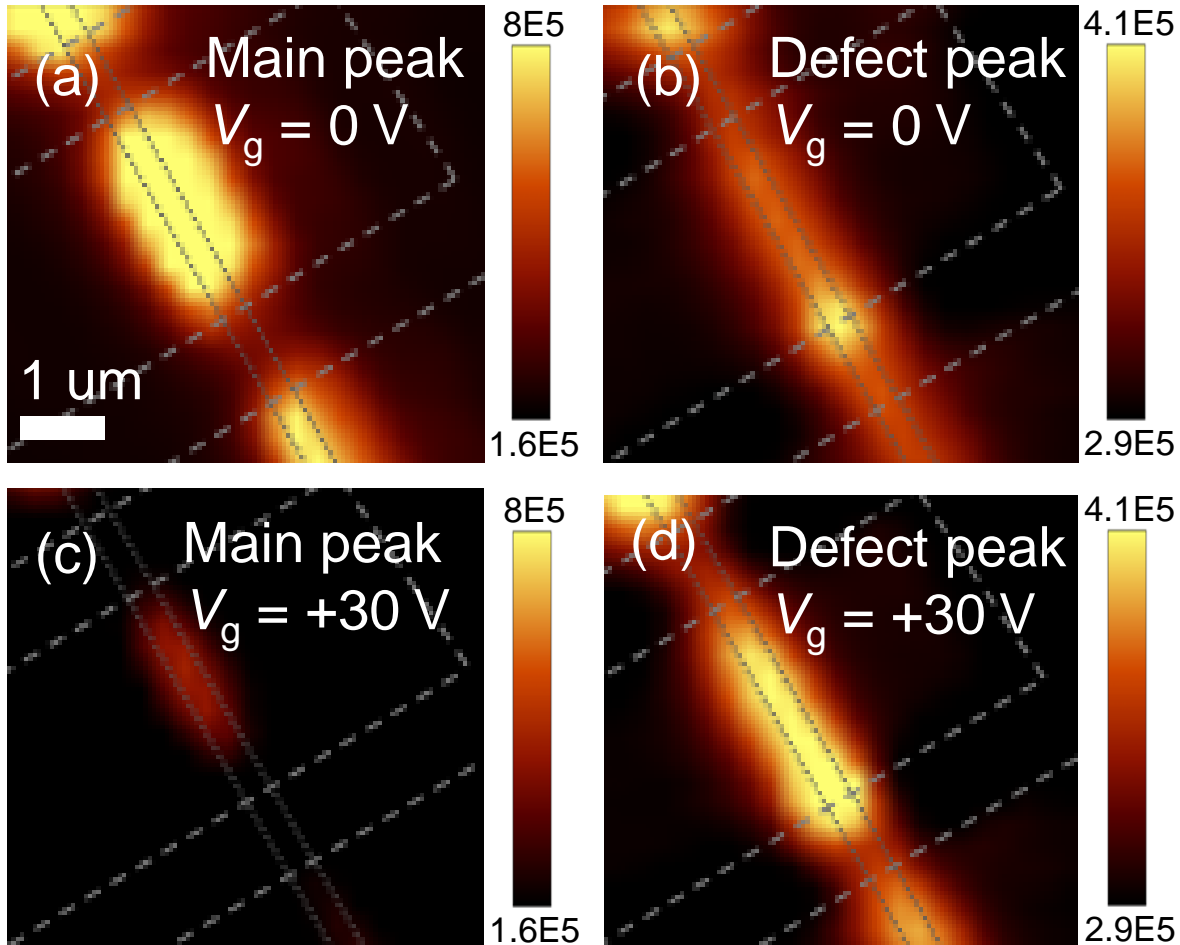


**Figure 7.4. Gate-tuned RT PL emission intensity mapping of a single ZnO NW device.** (a-d) The emission intensity mapping of the UV band edge emission peak (main peak) and defect-related peaks at gate voltages  $V_g = 0$  and  $+30$  V. A wavelength range of 370-450 nm was chosen to display the main band edge emission (a and c), while 480-640 nm was the selected range to display oxygen vacancy-induced emission (b and d). Dotted line in PL images represent the location of the NW and the electrodes.

The corresponding RT PL spectra are shown in Figure 7.5 for gate voltages of both  $V_g = 0$  V and +30 V. The strong suppression of the main emission reflects excitons associated with the band edge are loosely bounded and hence easily dissociated upon application of even a relatively weak field. However, the lack of suppression of the intensities of the defect-related peaks suggests the defect-related moments to be rather localized in the system. The response of the PL emission to the applied voltage is consistent with the carrier-mediated exchange interaction mechanism and with these interactions having been tuned by the gate field.

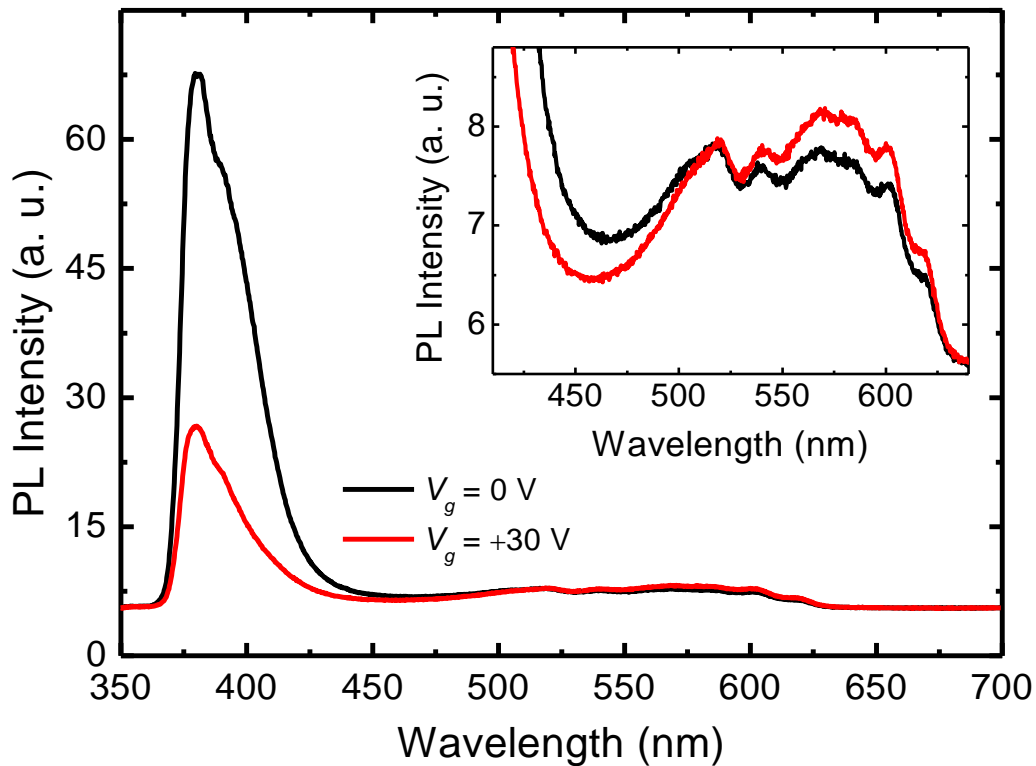


**Figure 7.5. Gate-tuned RT PL spectra of a single ZnO NW device.** The PL spectra of the single ZnO NW FET measured at  $V_g = 0$  V and +30 V. The PL spectra showed the intensity of the "main peak" at  $V_g = 0$  V was decreased considerably upon application of a gate voltage  $V_g = +30$  V. The inset shows that the intensity of "defect peak" at  $V_g = 0$  V changed slightly upon application of a gate voltage  $V_g = +30$  V.

### **7.3. Conclusion**

In summary, In order to clarify the presence of ferromagnetism and oxygen vacancies in the studied ZnO NW FET, we performed a UV confocal PL study for the individual device using a lab-made confocal microscope. The observation of green emission in an individual ZnO NW device indicates that the ZnO NW in our FET carries oxygen vacancy induced ferromagnetism. We also demonstrated the effects of gate voltage on photoluminescence (PL) spectra in an individual ferromagnetic ZnO NW FET devices. The PL spectra of an individual NW device conforms the localization of oxygen vacancy induced spins in the NW. The response of PL emission spectra to the applied gate voltage is consistent with carrier mediated exchange interaction mechanism and these interactions having been tuned by the gate field.

## REFERENCES

1. Wolf, S. A.; Awschalom, D. D.; Buhrman, R. A.; Daughton, J. M.; von Molnar, S.; Roukes, M. L.; Chtchelkanova, A. Y.; Treger, D. M. Spintronics: A spin-based electronics vision for the future. *Science* 2001, 294, 1488-1495.
2. Baibich, M. N.; Broto, J. M.; Fert, A.; Nguyen Van Dau, F.; Petroff, F.; Etienne, P.; Creuzet, G.; Friederich, A.; Chazelas, J. Giant magnetoresistance of (001)Fe/(001)Cr magnetic superlattices. *Phys Rev Lett* 1988, 61, 2472-2475.
3. Binasch, G.; Grunberg, P.; Saurenbach, F.; Zinn, W. Enhanced magnetoresistance in layered magnetic structures with antiferromagnetic interlayer exchange. *Phys Rev B Condens Matter* 1989, 39, 4828-4830.
4. Johnson, M.; Silsbee, R. H. Interfacial charge-spin coupling: Injection and detection of spin magnetization in metals. *Phys Rev Lett* 1985, 55, 1790-1793.
5. Johnson, M.; Silsbee, R. H. Coupling of Electronic Charge and Spin at a Ferromagnetic-Paramagnetic Metal Interface. *Phys Rev B* 1988, 37, 5312-5325.
6. Johnson, M.; Silsbee, R. H. Spin-Injection Experiment. *Phys Rev B* 1988, 37, 5326-5335.
7. Thomson, W. On the Electro-Dynamic Qualities of Metals:--Effects of Magnetization on the Electric Conductivity of Nickel and of Iron. *Proceedings of the Royal Society of London* 1856, 8, 546-550.
8. Smit, J. Magnetoresistance of ferromagnetic metals and alloys at low temperatures. *Physica* 1951, 17, 612-627.
9. Jedema, F. J.; Filip, A. T.; van Wees, B. J. Electrical spin injection and accumulation at room temperature in an all-metal mesoscopic spin valve. *Nature* 2001, 410, 345-348.
10. Jedema, F. J.; Heersche, H. B.; Filip, A. T.; Baselmans, J. J. A.; van Wees, B. J. Electrical detection of spin precession in a metallic mesoscopic spin valve. *Nature* 2002, 416, 713-716.
11. Jedema, F. J.; Nijboer, M. S.; Filip, A. T.; van Wees, B. J. Spin injection and spin accumulation in all-metal mesoscopic spin valves. *Phys Rev B* 2003, 67.
12. Tombros, N.; Jozsa, C.; Popinciuc, M.; Jonkman, H. T.; van Wees, B. J. Electronic spin transport and spin precession in single graphene layers at room temperature. *Nature* 2007, 448, 571-U4.
13. Tombros, N.; van der Molen, S. J.; van Wees, B. J. Separating spin and charge transport in single-wall carbon nanotubes. *Phys Rev B* 2006, 73.
14. Liu, E. S.; Nah, J.; Varahramyan, K. M.; Tutuc, E. Lateral Spin Injection in Germanium Nanowires. *Nano Lett* 2010, 10, 3297-3301.

15. Zhang, S. X.; Dayeh, S. A.; Li, Y.; Crooker, S. A.; Smith, D. L.; Picraux, S. T. Electrical Spin Injection and Detection in Silicon Nanowires through Oxide Tunnel Barriers. *Nano Lett* 2013, 13, 430-435.
16. van't Erve, O. M. J.; Friedman, A. L.; Li, C. H.; Robinson, J. T.; Connell, J.; Lauhon, L. J.; Jonker, B. T. Spin transport and Hanle effect in silicon nanowires using graphene tunnel barriers. *Nat Commun* 2015, 6.
17. Zwanenburg, F. A.; van der Mast, D. W.; Heersche, H. B.; Kouwenhoven, L. P.; Bakkers, E. P. A. M. Electric Field Control of Magnetoresistance in InP Nanowires with Ferromagnetic Contacts. *Nano Lett* 2009, 9, 2704-2709.
18. Heedt, S.; Morgan, C.; Weis, K.; Burgler, D. E.; Calarco, R.; Hardtdegen, H.; Grutzmacher, D.; Schapers, T. Electrical Spin Injection into InN Semiconductor Nanowires. *Nano Lett* 2012, 12, 4437-4443.
19. Datta, S.; Das, B. Electronic analog of the electro-optic modulator. *Applied Physics Letters* 1990, 56, 665-667.
20. Žutić, I.; Fabian, J.; Das Sarma, S. Spintronics: Fundamentals and applications. *Reviews of Modern Physics* 2004, 76, 323-410.
21. Awschalom, D. D.; Flatte, M. E. Challenges for semiconductor spintronics. *Nat Phys* 2007, 3, 153-159.
22. Valenzuela, S. O.; Tinkham, M. Direct electronic measurement of the spin Hall effect. *Nature* 2006, 442, 176-179.
23. Crooker, S. A.; Furis, M.; Lou, X.; Adelman, C.; Smith, D. L.; Palmstrom, C. J.; Crowell, P. A. Imaging spin transport in lateral ferromagnet/semiconductor structures. *Science* 2005, 309, 2191-2195.
24. Appelbaum, I.; Huang, B. Q.; Monsma, D. J. Electronic measurement and control of spin transport in silicon. *Nature* 2007, 447, 295-298.
25. Lou, X. H.; Adelman, C.; Crooker, S. A.; Garlid, E. S.; Zhang, J.; Reddy, K. S. M.; Flexner, S. D.; Palmstrom, C. J.; Crowell, P. A. Electrical detection of spin transport in lateral ferromagnet-semiconductor devices. *Nat Phys* 2007, 3, 197-202.
26. Koo, H. C.; Kwon, J. H.; Eom, J.; Chang, J.; Han, S. H.; Johnson, M. Control of Spin Precession in a Spin-Injected Field Effect Transistor. *Science* 2009, 325, 1515-1518.
27. Kum, H.; Heo, J.; Jahangir, S.; Banerjee, A.; Guo, W.; Bhattacharya, P. Room temperature single GaN nanowire spin valves with FeCo/MgO tunnel contacts. *Applied Physics Letters* 2012, 100.
28. Chappert, C.; Fert, A.; Van Dau, F. N. The emergence of spin electronics in data storage. *Nat Mater* 2007, 6, 813-823.
29. Furdyna, J. K. Diluted Magnetic Semiconductors. *J Appl Phys* 1988, 64, R29-R64.

30. Ferrand, D.; Cibert, J.; Wasiela, A.; Bourgognon, C.; Tatarenko, S.; Fishman, G.; Andreczyk, T.; Jaroszynski, J.; Kolesnik, S.; Dietl, T.; Barbara, B.; Dufeu, D. Carrier-induced ferromagnetism in p-Zn<sub>1-x</sub>Mn<sub>x</sub>Te. *Phys Rev B* 2001, 63.
31. Munekata, H.; Ohno, H.; Vonmolnar, S.; Segmuller, A.; Chang, L. L.; Esaki, L. Diluted Magnetic Iii-V Semiconductors. *Physical Review Letters* 1989, 63, 1849-1852.
32. Ohno, H.; Munekata, H.; Penney, T.; Vonmolnar, S.; Chang, L. L. Magnetotransport Properties of P-Type (In,Mn)As Diluted Magnetic Iii-V Semiconductors. *Physical Review Letters* 1992, 68, 2664-2667.
33. Ohno, H.; Shen, A.; Matsukura, F.; Oiwa, A.; Endo, A.; Katsumoto, S.; Iye, Y. (Ga,Mn)As: A new diluted magnetic semiconductor based on GaAs. *Applied Physics Letters* 1996, 69, 363-365.
34. Shen, A.; Ohno, H.; Matsukura, F.; Sugawara, Y.; Akiba, N.; Kuroiwa, T.; Oiwa, A.; Endo, A.; Katsumoto, S.; Iye, Y. Epitaxy of (Ga, Mn)As, a new diluted magnetic semiconductor based on GaAs. *J Cryst Growth* 1997, 175, 1069-1074.
35. Jungwirth, T.; Sinova, J.; Mašek, J.; Kučera, J.; MacDonald, A. H. Theory of ferromagnetic (III,Mn)V semiconductors. *Reviews of Modern Physics* 2006, 78, 809-864.
36. Edmonds, K. W.; Wang, K. Y.; Campion, R. P.; Neumann, A. C.; Farley, N. R. S.; Gallagher, B. L.; Foxon, C. T. High-Curie-temperature Ga<sub>1-x</sub>Mn<sub>x</sub>As obtained by resistance-monitored annealing. *Applied Physics Letters* 2002, 81, 4991-4993.
37. Chiba, D.; Takamura, K.; Matsukura, F.; Ohno, H. Effect of low-temperature annealing on (Ga,Mn)As trilayer structures. *Applied Physics Letters* 2003, 82, 3020-3022.
38. Fukumura, T.; Jin, Z.; Ohtomo, A.; Koinuma, H.; Kawasaki, M. An oxide-diluted magnetic semiconductor: Mn-doped ZnO. *Applied Physics Letters* 1999, 75, 3366-3368.
39. Matsumoto, Y.; Murakami, M.; Shono, T.; Hasegawa, T.; Fukumura, T.; Kawasaki, M.; Ahmet, P.; Chikyow, T.; Koshihara, S.; Koinuma, H. Room-temperature ferromagnetism in transparent transition metal-doped titanium dioxide. *Science* 2001, 291, 854-856.
40. Matsumoto, Y.; Takahashi, R.; Murakami, M.; Koida, T.; Fan, X. J.; Hasegawa, T.; Fukumura, T.; Kawasaki, M.; Koshihara, S. Y.; Koinuma, H. Ferromagnetism in co-doped TiO<sub>2</sub> rutile thin films grown by laser molecular beam epitaxy. *Jpn J Appl Phys* 2001, 40, L1204-L1206.
41. Ueda, K.; Tabata, H.; Kawai, T. Magnetic and electric properties of transition-metal-doped ZnO films. *Applied Physics Letters* 2001, 79, 988-990.
42. Ogale, S. B.; Choudhary, R. J.; Buban, J. P.; Lofland, S. E.; Shinde, S. R.; Kale, S. N.; Kulkarni, V. N.; Higgins, J.; Lanci, C.; Simpson, J. R.; Browning, N. D.; Das Sarma, S.; Drew, H. D.; Greene, R. L.; Venkatesan, T. High Temperature Ferromagnetism with a Giant Magnetic Moment in Transparent Co-doped  $\text{Mn}_{1-x}\text{Mg}_x\text{ZnO}$ . *Physical Review Letters* 2003, 91, 077205.



43. Kale, S. N.; Ogale, S. B.; Shinde, S. R.; Sahasrabudde, M.; Kulkarni, V. N.; Greene, R. L.; Venkatesan, T. Magnetism in cobalt-doped Cu<sub>2</sub>O thin films without and with Al, V, or Zn codopants. *Applied Physics Letters* 2003, 82, 2100-2102.
44. Philip, J.; Theodoropoulou, N.; Berera, G.; Moodera, J. S.; Satpati, B. High-temperature ferromagnetism in manganese-doped indium–tin oxide films. *Applied Physics Letters* 2004, 85, 777-779.
45. Coey, J. M. D.; Venkatesan, M.; Fitzgerald, C. B. Donor impurity band exchange in dilute ferromagnetic oxides. *Nat Mater* 2005, 4, 173-179.
46. Xing, G.; Wang, D.; Yi, J.; Yang, L.; Gao, M.; He, M.; Yang, J.; Ding, J.; Sum, T. C.; Wu, T. Correlated d<sub>0</sub> ferromagnetism and photoluminescence in undoped ZnO nanowires. *Applied Physics Letters* 2010, 96, 112511.
47. Panigrahy, B.; Aslam, M.; Misra, D. S.; Ghosh, M.; Bahadur, D. Defect-Related Emissions and Magnetization Properties of ZnO Nanorods. *Adv Funct Mater* 2010, 20, 1161-1165.
48. Mal, S.; Nori, S.; Jin, C.; Narayan, J.; Nellutla, S.; Smirnov, A. I.; Prater, J. T. Reversible room temperature ferromagnetism in undoped zinc oxide: Correlation between defects and physical properties. *J Appl Phys* 2010, 108, 073510.
49. Mal, S.; Narayan, J.; Nori, S.; Prater, J. T.; Kumar, D. Defect-mediated room temperature ferromagnetism in zinc oxide. *Solid State Commun* 2010, 150, 1660-1664.
50. Xu, X. Y.; Xu, C. X.; Lin, Y.; Li, J. T.; Hu, J. G. Comparison on Photoluminescence and Magnetism between Two Kinds of Undoped ZnO Nanorods. *J Phys Chem C* 2013, 117, 24549-24553.
51. Kushwaha, A.; Tyagi, H.; Aslam, M. Role of defect states in magnetic and electrical properties of ZnO nanowires. *Aip Adv* 2013, 3.
52. Kim, Y.-S.; Park, C. H. Rich Variety of Defects in ZnO via an Attractive Interaction between O Vacancies and Zn Interstitials: Origin of  $\delta$ -Type Doping. *Physical Review Letters* 2009, 102, 086403.
53. Vlasenko, L. S.; Watkins, G. D. Optical detection of electron paramagnetic resonance in room-temperature electron-irradiated ZnO. *Phys Rev B* 2005, 71.
54. Xing, G. Z.; Lu, Y. H.; Tian, Y. F.; Yi, J. B.; Lim, C. C.; Li, Y. F.; Li, G. P.; Wang, D.; Yao, B.; Ding, J.; Feng, Y. P.; Wu, T. Defect-induced magnetism in undoped wide band gap oxides: Zinc vacancies in ZnO as an example. *Aip Adv* 2011, 1.
55. Zhang, B. Y.; Yao, B.; Li, Y. F.; Liu, A. M.; Zhang, Z. Z.; Li, B. H.; Xing, G. Z.; Wu, T.; Qin, X. B.; Zhao, D. X.; Shan, C. X.; Shen, D. Z. Evidence of cation vacancy induced room temperature ferromagnetism in Li-N codoped ZnO thin films. *Applied Physics Letters* 2011, 99.
56. Chiu, S. P.; Lin, Y. H.; Lin, J. J. Electrical conduction mechanisms in natively doped ZnO nanowires. *Nanotechnology* 2009, 20.

57. Tsai, L. T.; Chiu, S. P.; Lu, J. G.; Lin, J. J. Electrical conduction mechanisms in natively doped ZnO nanowires (II). *Nanotechnology* 2010, 21.
58. Lu, Z. L.; Hsu, H. S.; Tzeng, Y. H.; Zhang, F. M.; Du, Y. W.; Huang, J. C. A. The origins of ferromagnetism in Co-doped ZnO single crystalline films: From bound magnetic polaron to free carrier-mediated exchange interaction. *Applied Physics Letters* 2009, 95, 102501.
59. Tian, Y.; Li, Y.; He, M.; Putra, I. A.; Peng, H.; Yao, B.; Cheong, S. A.; Wu, T. Bound magnetic polarons and p-d exchange interaction in ferromagnetic insulating Cu-doped ZnO. *Applied Physics Letters* 2011, 98, 162503.
60. He, M.; Tian, Y. F.; Springer, D.; Putra, I. A.; Xing, G. Z.; Chia, E. E. M.; Cheong, S. A.; Wu, T. Polaronic transport and magnetism in Ag-doped ZnO. *Applied Physics Letters* 2011, 99, 222511.
61. Walsh, A.; Da Silva, J. L. F.; Wei, S. H. Theoretical description of carrier mediated magnetism in cobalt doped ZnO. *Physical Review Letters* 2008, 100.
62. O'Handley, R. C. *Modern Magnetic Materials: Principles and Applications*. Wiley: 1999.
63. McGuire, T. R.; Potter, R. I. Anisotropic Magnetoresistance in Ferromagnetic 3d Alloys. *IEEE T Magn* 1975, 11, 1018-1038.
64. Lou, X.; Adelman, C.; Furis, M.; Crooker, S. A.; Palmstrom, C. J.; Crowell, P. A. Electrical detection of spin accumulation at a ferromagnet-semiconductor interface. *Physical Review Letters* 2006, 96.
65. van't Erve, O. M. J.; Hanbicki, A. T.; Holub, M.; Li, C. H.; Awo-Affouda, C.; Thompson, P. E.; Jonker, B. T. Electrical injection and detection of spin-polarized carriers in silicon in a lateral transport geometry. *Applied Physics Letters* 2007, 91.
66. Erve, O. M. J. v. t.; Awo-Affouda, C.; Hanbicki, A. T.; Li, C. H.; Thompson, P. E.; Jonker, B. T. Information Processing With Pure Spin Currents in Silicon: Spin Injection, Extraction, Manipulation, and Detection. *IEEE Transactions on Electron Devices* 2009, 56, 2343-2347.
67. Berend, T. J. Electrical Spin Injection and Transport in Semiconductors. In *Handbook of Spin Transport and Magnetism*, Chapman and Hall/CRC: 2011; pp 329-369.
68. Efros, A. L.; Pollak, M. *Electron-Electron Interactions in Disordered Systems*. Elsevier Science: 2012.
69. Altshuler, B. L.; Khmel'nitzkii, D.; Larkin, A. I.; Lee, P. A. Magnetoresistance and Hall effect in a disordered two-dimensional electron gas. *Phys Rev B* 1980, 22, 5142-5153.
70. Hikami, S.; Larkin, A. I.; Nagaoka, Y. Spin-Orbit Interaction and Magnetoresistance in the Two Dimensional Random System. *Progress of Theoretical Physics* 1980, 63, 707-710.
71. Inoue, J.-i. CHAPTER 2 - GMR, TMR and BMR A2 - Shinjo, Teruya. In *Nanomagnetism and Spintronics*, Elsevier: Amsterdam, 2009; pp 15-92.

72. Dresselhaus, G. Spin-Orbit Coupling Effects in Zinc Blende Structures. *Phys Rev* 1955, 100, 580-586.
73. Bychkov, Y. A.; Rashba, E. I. Oscillatory Effects and the Magnetic-Susceptibility of Carriers in Inversion-Layers. *J Phys C Solid State* 1984, 17, 6039-6045.
74. Hall, E. H. On a New Action of the Magnet on Electric Currents. *American Journal of Mathematics* 1879, 2, 287-292.
75. Dyakonov, M. I.; Perel, V. I. Possibility of Orienting Electron Spins with Current. *Jetp Lett-Ussr* 1971, 13, 467-&.
76. Hirsch, J. E. Spin Hall Effect. *Physical Review Letters* 1999, 83, 1834-1837.
77. Kimura, T.; Otani, Y.; Sato, T.; Takahashi, S.; Maekawa, S. Room-temperature reversible spin Hall effect. *Physical Review Letters* 2007, 98.
78. Kontani, H.; Tanaka, T.; Hirashima, D. S.; Yamada, K.; Inoue, J. Giant Intrinsic Spin and Orbital Hall Effects in  $\text{Sr}_2\text{M}\{\text{O}\}_4$  ( $M=\text{Ru}$ , Rh, Mo). *Physical Review Letters* 2008, 100, 096601.
79. Kontani, H.; Tanaka, T.; Hirashima, D. S.; Yamada, K.; Inoue, J. Giant Orbital Hall Effect in Transition Metals: Origin of Large Spin and Anomalous Hall Effects. *Physical Review Letters* 2009, 102, 016601.
80. Matsukura, F.; Tokura, Y.; Ohno, H. Control of magnetism by electric fields. *Nat Nanotechnol* 2015, 10, 209-220.
81. Ohno, H.; Chiba, D.; Matsukura, F.; Omiya, T.; Abe, E.; Dietl, T.; Ohno, Y.; Ohtani, K. Electric-field control of ferromagnetism. *Nature* 2000, 408, 944-946.
82. Boukari, H.; Kossacki, P.; Bertolini, M.; Ferrand, D.; Cibert, J.; Tatarenko, S.; Wasiela, A.; Gaj, J. A.; Dietl, T. Light and Electric Field Control of Ferromagnetism in Magnetic Quantum Structures. *Physical Review Letters* 2002, 88, 207204.
83. Lee, H.-J.; Helgren, E.; Hellman, F. Gate-controlled magnetic properties of the magnetic semiconductor (Zn,Co)O. *Applied Physics Letters* 2009, 94, 212106.
84. Li, L.; Guo, Y.; Cui, X. Y.; Zheng, R.; Ohtani, K.; Kong, C.; Ceguerra, A. V.; Moody, M. P.; Ye, J. D.; Tan, H. H.; Jagadish, C.; Liu, H.; Stampfl, C.; Ohno, H.; Ringer, S. P.; Matsukura, F. Magnetism of Co-doped ZnO epitaxially grown on a ZnO substrate. *Phys Rev B* 2012, 85, 174430.
85. Sawicki, M.; Chiba, D.; Korbecka, A.; Nishitani, Y.; Majewski, J. A.; Matsukura, F.; Dietl, T.; Ohno, H. Experimental probing of the interplay between ferromagnetism and localization in (Ga, Mn)As. *Nat Phys* 2010, 6, 22-25.
86. Wen Chang, H.; Akita, S.; Matsukura, F.; Ohno, H. Hole concentration dependence of the Curie temperature of (Ga,Mn)Sb in a field-effect structure. *Applied Physics Letters* 2013, 103, 142402.

87. Nepal, N.; Luen, M. O.; Zavada, J. M.; Bedair, S. M.; Frajtag, P.; El-Masry, N. A. Electric field control of room temperature ferromagnetism in III-N dilute magnetic semiconductor films. *Applied Physics Letters* 2009, 94, 132505.
88. Park, Y. D.; Hanbicki, A. T.; Erwin, S. C.; Hellberg, C. S.; Sullivan, J. M.; Mattson, J. E.; Ambrose, T. F.; Wilson, A.; Spanos, G.; Jonker, B. T. A Group-IV Ferromagnetic Semiconductor:  $\text{MnxGe}_{1-x}$ . *Science* 2002, 295, 651-654.
89. Yamada, Y.; Ueno, K.; Fukumura, T.; Yuan, H. T.; Shimotani, H.; Iwasa, Y.; Gu, L.; Tsukimoto, S.; Ikuhara, Y.; Kawasaki, M. Electrically Induced Ferromagnetism at Room Temperature in Cobalt-Doped Titanium Dioxide. *Science* 2011, 332, 1065-1067.
90. Checkelsky, J. G.; Ye, J. T.; Onose, Y.; Iwasa, Y.; Tokura, Y. Dirac-fermion-mediated ferromagnetism in a topological insulator. *Nat Phys* 2012, 8, 729-733.
91. Kou, X. F.; He, L.; Lang, M. R.; Fan, Y. B.; Wong, K.; Jiang, Y.; Nie, T. X.; Jiang, W. J.; Upadhyaya, P.; Xing, Z. K.; Wang, Y.; Xiu, F. X.; Schwartz, R. N.; Wang, K. L. Manipulating Surface-Related Ferromagnetism in Modulation-Doped Topological Insulators. *Nano Lett* 2013, 13, 4587-4593.
92. Meng, X. B.; Yang, X. Q.; Sun, X. L. Emerging Applications of Atomic Layer Deposition for Lithium-Ion Battery Studies. *Adv Mater* 2012, 24, 3589-3615.
93. Klingshirn, C. ZnO: Material, physics and applications. *Chemphyschem* 2007, 8, 782-803.
94. Grundmann, M.; Frenzel, H.; Lajn, A.; Lorenz, M.; Schein, F.; von Wenckstern, H. Transparent semiconducting oxides: materials and devices. *Phys Status Solidi A* 2010, 207, 1437-1449.
95. Modepalli, V.; Jin, M. J.; Park, J.; Jo, J.; Kim, J. H.; Baik, J. M.; Seo, C.; Kim, J.; Yoo, J. W. Gate-Tunable Spin Exchange Interactions and Inversion of Magnetoresistance in Single Ferromagnetic ZnO Nanowires. *Acs Nano* 2016, 10, 4618-4626.
96. Ozgur, U.; Alivov, Y. I.; Liu, C.; Teke, A.; Reshchikov, M. A.; Dogan, S.; Avrutin, V.; Cho, S. J.; Morkoc, H. A comprehensive review of ZnO materials and devices. *J Appl Phys* 2005, 98.
97. Law, M.; Greene, L. E.; Johnson, J. C.; Saykally, R.; Yang, P. D. Nanowire dye-sensitized solar cells. *Nat Mater* 2005, 4, 455-459.
98. Menzel, A.; Subannajui, K.; Guder, F.; Moser, D.; Paul, O.; Zacharias, M. Multifunctional ZnO-Nanowire-Based Sensor. *Adv Funct Mater* 2011, 21, 4342-4348.
99. Singh, D. P. Synthesis and Growth of ZnO Nanowires. *Sci Adv Mater* 2010, 2, 245-272.
100. Baik, J. M.; Lee, J. L. Fabrication of vertically well-aligned (Zn,Mn)O nanorods with room temperature ferromagnetism. *Adv Mater* 2005, 17, 2745-+.
101. Lupan, O.; Emelchenko, G. A.; Ursaki, V. V.; Chai, G.; Redkin, A. N.; Gruzintsev, A. N.; Tiginyanu, I. M.; Chow, L.; Ono, L. K.; Cuenya, B. R.; Heinrich, H.; Yakimov, E. E. Synthesis and characterization of ZnO nanowires for nanosensor applications. *Mater Res Bull* 2010, 45, 1026-1032.

102. Tak, Y.; Park, D.; Yong, K. J. Characterization of ZnO nanorod arrays fabricated on Si wafers using a low-temperature synthesis method. *J Vac Sci Technol B* 2006, 24, 2047-2052.
103. Wang, J. P.; Wang, Z. Y.; Huang, B. B.; Ma, Y. D.; Liu, Y. Y.; Qin, X. Y.; Zhang, X. Y.; Dai, Y. Oxygen Vacancy Induced Band-Gap Narrowing and Enhanced Visible Light Photocatalytic Activity of ZnO. *Acs Appl Mater Inter* 2012, 4, 4024-4030.
104. Dietl, T.; Ohno, H.; Matsukura, F.; Cibert, J.; Ferrand, D. Zener model description of ferromagnetism in zinc-blende magnetic semiconductors. *Science* 2000, 287, 1019-1022.
105. Chang, L. T.; Wang, C. Y.; Tang, J. S.; Nie, T. X.; Jiang, W. J.; Chu, C. P.; Arafin, S.; He, L.; Afsal, M.; Chen, L. J.; Wang, K. L. Electric-Field Control of Ferromagnetism in Mn-Doped ZnO Nanowires. *Nano Lett* 2014, 14, 1823-1829.
106. Bardeen, J.; Brattain, W. H. The Transistor, a Semi-Conductor Triode. *Phys Rev* 1948, 74, 230-231.
107. Shockley, W. The Theory of p-n Junctions in Semiconductors and p-n Junction Transistors. *Bell System Technical Journal* 1949, 28, 435-489.
108. Edgar, L. J. Method and apparatus for controlling electric currents. Google Patents: 1930.
109. Lee, J. M.; Kim, K. K.; Park, S. J.; Choi, W. K. Low-resistance and nonalloyed ohmic contacts to plasma treated ZnO. *Applied Physics Letters* 2001, 78, 3842-3844.
110. Kim, H.-K.; Han, S.-H.; Seong, T.-Y.; Choi, W.-K. Low-resistance Ti/Au ohmic contacts to Al-doped ZnO layers. *Applied Physics Letters* 2000, 77, 1647-1649.
111. Myers, E. B.; Ralph, D. C.; Katine, J. A.; Louie, R. N.; Buhrman, R. A. Current-induced switching of domains in magnetic multilayer devices. *Science* 1999, 285, 867-870.
112. Slonczewski, J. C. Current-driven excitation of magnetic multilayers. *J Magn Magn Mater* 1996, 159, L1-L7.
113. Catalan, G.; Seidel, J.; Ramesh, R.; Scott, J. F. Domain wall nanoelectronics. *Reviews of Modern Physics* 2012, 84, 119-156.
114. Yamaguchi, A.; Ono, T.; Nasu, S.; Miyake, K.; Mibu, K.; Shinjo, T. Real-Space Observation of Current-Driven Domain Wall Motion in Submicron Magnetic Wires. *Physical Review Letters* 2004, 92, 077205.
115. Chernyshov, A.; Overby, M.; Liu, X. Y.; Furdyna, J. K.; Lyanda-Geller, Y.; Rokhinson, L. P. Evidence for reversible control of magnetization in a ferromagnetic material by means of spin-orbit magnetic field. *Nat Phys* 2009, 5, 656-659.
116. Liu, L. Q.; Pai, C. F.; Li, Y.; Tseng, H. W.; Ralph, D. C.; Buhrman, R. A. Spin-Torque Switching with the Giant Spin Hall Effect of Tantalum. *Science* 2012, 336, 555-558.

117. Dietl, T. A ten-year perspective on dilute magnetic semiconductors and oxides. *Nat Mater* 2010, 9, 965-974.
118. Ohno, H. A window on the future of spintronics. *Nat Mater* 2010, 9, 952-954.
119. Datta, S.; Das, B. Electronic Analog of the Electrooptic Modulator. *Applied Physics Letters* 1990, 56, 665-667.
120. Tang, J. S.; Wang, C. Y.; Hung, M. H.; Jiang, X. W.; Chang, L. T.; He, L.; Liu, P. H.; Yang, H. J.; Tuan, H. Y.; Chen, L. J.; Wang, K. L. Ferromagnetic Germanide in Ge Nanowire Transistors for Spintronics Application. *Acs Nano* 2012, 6, 5710-5717.
121. Tsai, C. I.; Wang, C. Y.; Tang, J. S.; Hung, M. H.; Wang, K. L.; Chen, L. J. Electrical Properties and Magnetic Response of Cobalt Germanosilicide Nanowires. *Acs Nano* 2011, 5, 9552-9558.
122. Khosla, R. P.; Fischer, J. R. Magnetoresistance in Degenerate CdS: Localized Magnetic Moments. *Phys Rev B* 1970, 2, 4084-4097.
123. Peters, J. A.; Parashar, N. D.; Rangaraju, N.; Wessels, B. W. Magnetotransport properties of InMnSb magnetic semiconductor thin films. *Phys Rev B* 2010, 82, 205207.
124. An, Y.; Ren, Y.; Yang, D.; Wu, Z.; Liu, J. Oxygen Vacancy-Induced Room Temperature Ferromagnetism and Magnetoresistance in Fe-Doped In<sub>2</sub>O<sub>3</sub> Films. *The Journal of Physical Chemistry C* 2015, 119, 4414-4421.
125. Xing, G. Z.; Lu, Y. H.; Tian, Y. F.; Yi, J. B.; Lim, C. C.; Li, Y. F.; Li, G. P.; Wang, D. D.; Yao, B.; Ding, J.; Feng, Y. P.; Wu, T. Defect-induced magnetism in undoped wide band gap oxides: Zinc vacancies in ZnO as an example. *Aip Adv* 2011, 1, 022152.
126. Tian, Y. F.; Li, Y. F.; Wu, T. Tuning magnetoresistance and exchange coupling in ZnO by doping transition metals. *Applied Physics Letters* 2011, 99.
127. Gacic, M.; Jakob, G.; Herbort, C.; Adrian, H.; Tietze, T.; Brück, S.; Goering, E. Magnetism of Co-doped ZnO thin films. *Phys Rev B* 2007, 75, 205206.
128. Reuss, F.; Frank, S.; Kirchner, C.; Kling, R.; Gruber, T.; Waag, A. Magnetoresistance in epitaxially grown degenerate ZnO thin films. *Applied Physics Letters* 2005, 87, 112104.
129. Zeng, Y. J.; Pereira, L. M. C.; Menghini, M.; Temst, K.; Vantomme, A.; Locquet, J. P.; Van Haesendonck, C. Tuning Quantum Corrections and Magnetoresistance in ZnO Nanowires by Ion Implantation. *Nano Lett* 2012, 12, 666-672.
130. Appelbau, J. Exchange Model of Zero-Bias Tunneling Anomalies. *Phys Rev* 1967, 154, 633-&.
131. Appelbaum, J. "s-d" Exchange Model of Zero-Bias Tunneling Anomalies. *Physical Review Letters* 1966, 17, 91-95.

132. Watts, S. M.; Wirth, S.; von Molnár, S.; Barry, A.; Coey, J. M. D. Evidence for two-band magnetotransport in half-metallic chromium dioxide. *Phys Rev B* 2000, 61, 9621-9628.
133. Marsocci, V. A. Anisotropic Magnetoresistance in Ferromagnetic 3d Alloys - Comment. *IEEE T Magn* 1976, 12, 46-46.
134. Schierholz, C.; Matsuyama, T.; Merkt, U.; Meier, G. Weak localization and spin splitting in inversion layers on  $\delta$ -type InAs. *Phys Rev B* 2004, 70, 233311.
135. Turk, M. E.; Choi, J. H.; Oh, S. J.; Fafarman, A. T.; Diroll, B. T.; Murray, C. B.; Kagan, C. R.; Kikkawa, J. M. Gate-induced carrier delocalization in quantum dot field effect transistors. *Nano Lett* 2014, 14, 5948-52.
136. Ngueyn, V. L.; Spivak, B. Z.; Shklovskii, B. I. Tunnel Hopping in a Disordered System. *Zh Eksp Teor Fiz* 1985, 89, 1770-1784.
137. Sivan, U.; Entinwohman, O.; Imry, Y. Orbital Magnetoconductance in the Variable-Range-Hopping Regime. *Physical Review Letters* 1988, 60, 1566-1569.
138. Shklovskii, B. I.; Éfros, A. L. *Electronic properties of doped semiconductors*. Springer-Verlag: Berlin ; New York, 1984; p xii, 388 p.
139. di Vittorio, S. L.; Dresselhaus, M. S.; Endo, M.; Nakajima, T. Magnetotransport at the metal-insulator transition in fluorine-intercalated graphite fibers. *Phys Rev B* 1991, 43, 12304-12315.
140. Zhou, R.; Sun, B. Q.; Ruan, X. Z.; Luo, H. H.; Ji, Y.; Wang, W. Z.; Zhang, F.; Zhao, J. H. Temperature dependence of effective g factor in diluted magnetic semiconductor (Ga,Mn)As. *J Appl Phys* 2008, 103, 053901.
141. Chen, T.; Xing, G. Z.; Zhang, Z.; Chen, H. Y.; Wu, T. Tailoring the photoluminescence of ZnO nanowires using Au nanoparticles. *Nanotechnology* 2008, 19.
142. Djurišić, A. B.; Leung, Y. H.; Tam, K. H.; Ding, L.; Ge, W. K.; Chen, H. Y.; Gwo, S. Green, yellow, and orange defect emission from ZnO nanostructures: Influence of excitation wavelength. *Applied Physics Letters* 2006, 88, 103107.
143. Djuricic, A. B.; Leung, Y. H.; Tam, K. H.; Hsu, Y. F.; Ding, L.; Ge, W. K.; Zhong, Y. C.; Wong, K. S.; Chan, W. K.; Tam, H. L.; Cheah, K. W.; Kwok, W. M.; Phillips, D. L. Defect emissions in ZnO nanostructures. *Nanotechnology* 2007, 18.
144. Ghosh, M.; Raychaudhuri, A. K. Ionic environment control of visible photoluminescence from ZnO nanoparticles. *Applied Physics Letters* 2008, 93, 123113.
145. Hsu, N. E.; Hung, W. K.; Chen, Y. F. Origin of defect emission identified by polarized luminescence from aligned ZnO nanorods. *J Appl Phys* 2004, 96, 4671-4673.



146. Ye, J. D.; Gu, S. L.; Qin, F.; Zhu, S. M.; Liu, S. M.; Zhou, X.; Liu, W.; Hu, L. Q.; Zhang, R.; Shi, Y.; Zheng, Y. D. Correlation between green luminescence and morphology evolution of ZnO films. *Appl Phys a-Mater* 2005, 81, 759-762.
147. Chen, R.; Tay, Y.; Ye, J.; Zhao, Y.; Xing, G. Z.; Wu, T.; Sun, H. D. Investigation of Structured Green-Band Emission and Electron-Phonon Interactions in Vertically Aligned ZnO Nanowires. *J Phys Chem C* 2010, 114, 17889-17893.
148. Li, M. J.; Xing, G. C.; Xing, G. Z.; Wu, B.; Wu, T.; Zhang, X. H.; Sum, T. C. Origin of green emission and charge trapping dynamics in ZnO nanowires. *Phys Rev B* 2013, 87.
149. Kushwaha, A.; Tyagi, H.; Aslam, M. Role of defect states in magnetic and electrical properties of ZnO nanowires. *Aip Adv* 2013, 3, 042110.



## ACKNOWLEDGEMENTS

It would have been impossible to finish this work without the help and support of many kind people. Unfortunately, it is only possible to give particular mention to a few ones here. I apologize in case I fail to write down some names, but be sure they are forever written on my mind.

Foremost, I would like to express my admiration and sincere gratitude to my doctoral advisor Prof. Dr. Jung-Woo Yoo for giving me the honor to work in his group at the Functional Hybrid Materials and Devices Lab (FHMDL), UNIST. I am very grateful for his guidance, support, and patience during all these years. I am also grateful to the UNIST and South Korea for giving me the opportunity to stay and study Ph.D. course.

I would also thank to my Doctoral committee members, Prof. Kibog Park, Prof. Jeong Min Baik, Prof. Ki-Suk Lee and Prof. Jeongyong Kim for their valuable suggestions and discussions during my thesis defense. I would like to thank Prof. Jeong Min Baik and Ms. Ji-Hyun Kim for providing good ZnO nanowire samples. I also would like to thank Prof. Jeongyong Kim and Dr. Changwon Seo from Sungkyunkwan University for the help of PL characterization. I would also like to thank all the faculty members of Department of Materials Science and Mechanical Engineering, who directly or indirectly helped me and supported me for the Ph.D. admission as well as Ph.D. graduation. I would also like to thank all my teachers of High school, College, Undergraduate, Master course, for their kind motivation to reach this level. I am particularly highly grateful to Prof. D. Narayana Rao and Prof C.K. Jayasankar for their support and encouragement to study Ph.D. course at UNIST.

I would also like to thank active and alumini of my lab members, Ms. Mi-jin Jin, Mr. Jungmin Park, Mr. Junhyeon Jo, Ms. In-Seon Oh, Mr. Dae-Seong Choi, and Mr. Dong Hoon Kim for their kindness and support. I specially thank Mi-Jin Jin for her friendship and for her valuable discussions during the experiment. I would like to thank all Materials Science Engineering and other department fellow colleagues whom I met and share some of their time during my stay at UNIST. In particular I would also like to thank my off lab Korean friend, Dr. Jae-Kyung Choi for his friendship during my stay at UNIST.

I would also like to thank the staff of UNIST central research facility and Nanofabrication clean room for their kind support for my experiment and characterization. In particular, I specially thank the e-beam lithography operator Ms. Lu-da Lee for her assistance and patience during e-beam lithography device processing. I would like to thank the nonteaching staff members of Materials Science and Engineering

department and UNIST administration, for their assistance during my Ph.D course. I specially thank Ms. Jiyeon Kim, Mr. Nanyong Park and Ms. Yoon Jin A, for their discussion when I meet them.

I would also thank my off lab foreigner friends, Dr. Ajay, Ms. Ghana and family, Mr. Jyothi Partho, Dr. Ravikumar Cheedarala, Dr. Vijaya and family, Dr. Rahul, Dr Deepthi and family, Dr. Vinu, Dr. Jayalakshmi, Dr. Armugam, Dr. Durgaprasad, Dr. Biplab and family, Dr Noor, Mr. Munaz, Dr. Raju, and all for making me feel the wrath of a family and shared love with me.

Specially, I owe my parents, Nagarathamma Modepalli and Venkataiah Modepalli for their understanding and support on my pursuits. Their persistence, kindness, and honesty are always greatest worth and have always rooted in my life. I would also thank my grandfather Subbarayudu Bollineni and Chinnaiah Modepalli, grandmother, Subbamma Bollineni and Subbamma Modepalli, my Brother Ramana Modepalli and all my family members, friends and well-wishers for their kind support and encouragement.

Finally, I am indebted to my dear wife, Jhanshi Modepalli for her years support and love. Without her tireless dedication to our family, this thesis would not have been delivered. It is my luck to experience the beautiful life with her. I am also thankful to the Almighty for always keeping me warm through all leaps and falls of my Ph.D. and giving me a confidence for life whenever I fail.